

# Effective Medium Approximation for Infrared Surface-Enhancing Substrates

A Thesis Submitted to the  
College of Graduate and Postdoctoral Studies  
In Partial Fulfillment of the Requirements  
For the Degree of Master of Science  
In the Department of Chemistry  
University of Saskatchewan  
Saskatoon

By

Ian Richard Andvaag

Copyright Ian Andvaag, April 2022. This work is licensed under a Creative Commons Attribution 4.0 International License.

Unless otherwise noted, copyright of the material in this thesis belongs to the author and is licensed under the Creative Commons Attribution 4.0 International License.

## I Permission to Use

In presenting this thesis/dissertation in partial fulfillment of the requirements for a Postgraduate degree from the University of Saskatchewan, I agree that the Libraries of this University may make it freely available for inspection. I further agree that permission for copying of this thesis/dissertation in any manner, in whole or in part, for scholarly purposes may be granted by the professor or professors who supervised my thesis/dissertation work or, in their absence, by the Head of the Department or the Dean of the College in which my thesis work was done. It is understood that any copying or publication or use of this thesis/dissertation or parts thereof for financial gain shall not be allowed without my written permission. It is also understood that due recognition shall be given to me and to the University of Saskatchewan in any scholarly use which may be made of any material in my thesis/dissertation.



This work is licensed under a [Creative Commons Attribution-NonCommercial-ShareAlike 4.0 International License](https://creativecommons.org/licenses/by-nc-sa/4.0/).

## **II Disclaimer**

Reference in this thesis/dissertation to any specific commercial products, process, or service by trade name, trademark, manufacturer, or otherwise, does not constitute or imply its endorsement, recommendation, or favoring by the University of Saskatchewan. The views and opinions of the author expressed herein do not state or reflect those of the University of Saskatchewan, and shall not be used for advertising or product endorsement purposes.

Requests for permission to copy or to make other uses of materials in this thesis/dissertation in whole or part should be addressed to:

Department of Chemistry

University of Saskatchewan

165 Thorvaldson Building, 110 Science Place

Saskatoon, Saskatchewan S7N 5C9 Canada

OR

Dean

College of Graduate and Postdoctoral Studies

University of Saskatchewan

116 Thorvaldson Building, 110 Science Place

Saskatoon, Saskatchewan S7N 5C9 Canada

### **III Abstract**

Surface-enhanced infrared absorption spectroscopy (SEIRAS) is an increasingly popular analytical technique for studying molecular adsorption, finding applications in catalysis, biosensing and battery research. Crucial to its operation is a textured metal film, which can be produced by physical vapour deposition, galvanic electroless deposition and more recently, electrochemical reduction onto a conductive metal oxide layer. All methods suffer from poorly defined substrates which are difficult to reproduce with a consistent response. A model which predicts the optical response of a SEIRAS film could guide the development of better deposition procedures. This work aims to implement a model utilizing the Bruggeman effective medium approximation (EMA) and the Fresnel equations to calculate SEIRAS spectra for a range of morphologies and validate the calculations with experimental spectra.

The developed model reproduces the asymmetric line shapes seen in experimental measurements, which arise from the Fresnel equations and a small change in the refractive index upon molecular adsorption onto a moderately reflective substrate. The Bruggeman model demonstrates that composite metal-dielectric films can acquire a permittivity function yielding moderate reflection under the conditions of a SEIRAS experiment. The angle-dependent behaviour is explained well by electric field strength calculations. The Bruggeman EMA also successfully explains the general trends observed in SEIRAS films and appears to be a useful tool to optimize the surface morphology for maximal enhancement without yielding bimodal spectra. Further work incorporating percolation theory as well as nucleation and growth models may be able to link the crucial fill-factor parameter to an experimentally accessible variable.

## **IV Acknowledgements**

First and foremost, I would like to thank my supervisor, Ian Burgess. You have been a fantastic guide and teacher. I'm grateful for the time you've invested into me through many hours of discussion. I particularly appreciate you offering your modern spectroscopy course which has really shaped my thinking and provided a crucial foundation for the work presented here.

It was truly a joy to work alongside the other members of the Burgess group. Each of you have fostered a productive and positive working environment. In particular, I would like to thank Erick Lins for supplying some polarization and angle-dependent data used to validate the modelling results. Thanks also to Osai Clarke for acquiring SEM images, and Tyler Morhart for a substantial amount of photolithography work that ultimately did not end up providing publishable results due to lack of time on my part. Thanks to the entire lab group for adopting ITO/metal substrates and providing the motivation for this research.

I am grateful to Dr. Robert Johanson for graciously providing training and access to the sputtering equipment in his lab in the Engineering department.

Thanks to my parents for their support and care. Thanks also to my brother, who was willing to listen to me ramble on about effective medium theories and who was available to consult on Python-related issues.

Finally, I would like to recognize the financial support provided by NSERC by awarding me the CGS-M scholarship. Thanks also to the University of Saskatchewan and my TA managers, Pearson Ahiahonu and Adrian Clark.

## V Contents

I	Permission to Use	
II	Disclaimer	i
III	Abstract	ii
IV	Acknowledgements	iii
V	Contents	iv
V.i	List of Tables	vii
V.ii	List of Figures	viii
V.iii	List of Abbreviations	xi
1	INTRODUCTION	1
2	BACKGROUND	3
2.1	Surface-enhanced vibrational spectroscopy	3
2.1.1	Motivation for Using ATR-SEIRAS	8
2.1.2	Modern Approaches in ATR-SEIRAS	9
2.1.3	Spectral Line Shapes	12
2.1.4	SEIRAS Enhancement Mechanisms	13
2.1.5	Approach to Address Open Questions in ATR-SEIRAS	14
2.2	Basic Electromagnetics Background	16
2.2.1	Classical Electromagnetic Approach	16
2.2.2	Permittivity and Permeability	17
2.2.3	Parameters of Electromagnetic Waves	18
2.2.4	Surface Selection Rule	19

2.3	Drude-Lorentz model	21
2.3.1	Lorentz Model	21
2.3.2	Drude Model for Conductors	22
2.3.3	Generalized Drude-Lorentz Model for Multiple Resonances	23
2.4	Transfer Matrix Method	24
2.4.1	Snell's Law and Fresnel Equations	24
2.4.2	Propagation Matrices	25
2.5	Percolation Theory	25
2.6	Effective Medium Approximations	27
2.6.1	Maxwell-Garnett	30
2.6.2	Bruggeman	31
2.7	Plasmonic Enhancement Mechanism	31
2.7.1	Bulk Plasmons and Epsilon Near Zero Modes	32
2.7.2	Polaritons	34
2.7.3	Surface Plasmon-Polaritons	34
3	EXPERIMENTAL METHODOLOGY	40
3.1	Deposition of CMO Thin Films	40
3.2	Bimodality Parameter and Peak Height	41
3.3	Electrodeposition Spectroscopic Data	42
3.4	Cyanate Angle-Dependent Data	43
4	IMPLEMENTATION OF AN EMA MODEL	44
4.1	Selecting an Effective Medium Model	44
4.2	Formulation of Bruggeman model	47
4.3	Derivation of an Algorithm for an Arbitrary Number of Ellipsoidal particles	51
4.3.1	Algorithm for the Product of a Variable Number of Binomial Terms	53

4.3.2	Calculate the Coefficients for Each Additive Polynomial	54
4.3.3	Calculate the Roots of the Polynomial	55
4.3.4	Determine the Physically Correct Root	55
4.3.5	Calculate $\epsilon_{BR}, x, \epsilon_{BR}, y, \epsilon_{BR}, z$	57
5	RESULTS AND DISCUSSION	59
5.1	CMO Modelling	59
5.2	Plasmons	60
5.2.1	Propagating Surface Plasmon Polariton (PSPP) Modes	61
5.2.2	Epsilon Near Zero (ENZ) Modes	64
5.2.3	Localized Surface Plasmon Polariton (LSPP) Modes	66
5.3	Evaluating SEIRAS response	68
5.3.1	Model to Extract Fill Factor From SEM of SEIRAS film	72
5.3.2	Nucleation and Growth	73
5.3.3	CMO-Au Films Compared to Conventional Pure Au Films	75
5.4	Spectral Line Shapes	79
6	CONCLUSIONS AND FUTURE WORK	85
7	REFERENCES	88
8	APPENDIX: DETAILED SPUTTERING INSTRUCTIONS	97
8.1	Introductory notes	97
8.2	Changing the target	97
8.3	Calibrating the thickness measurement of the quartz crystal monitor	98
8.4	Instructions for use	98
8.5	Shutdown procedure	100

## V.i List of Tables

Table 2-1: Comparison of common EMA expressions.	29
Table 4-1: Polarizabilities for several common particle morphologies. $L_\tau$ is the depolarization factor along the $\tau^{\text{th}}$ ellipsoidal semi-axis ( $\tau = a, b, c$ ) and $F$ is fractional volume of coated ellipsoid occupied by the core material. Subscripts: sh = shell; mat = matrix.	48
Table 4-2: Ellipsoid depolarization factors, where $\gamma$ is the aspect ratio of major semi-axis to minor semi-axis ( $\gamma \geq 1$ ). $\tau$ refers to the index of the Cartesian axis; and $a, b, c$ refer to the radii of the semi-axes from largest to smallest. The integration variable, $q$ , in the expression for the general form is an ellipsoidal coordinate; details are outside the scope of this work but can be found in Bohren and Huffman. <sup>88</sup>	49
Table 4-3: Bounds on physical validity of $\epsilon_{\text{BR}}$ .	56
Table 5-1: Summary of investigation of momentum matching analysis for CMO/Au composite interface.	64

## V.ii List of Figures

Figure 2-1: Configurations for IR measurements of analyte-containing solutions.	4
Figure 2-2: Situating ATR-SEIRAS in the scheme of vibrational spectroscopic techniques.	7
Figure 2-3: Framework locating the background topics to be presented in the following subsections.	16
Figure 2-4: Relationships between parameters characterizing waves.	19
Figure 2-5: Real charges and induced image charges explain the surface selection rule. The arrows indicate the direction of the dipole moment vector.	20
Figure 2-6: Comparison of Bruggeman and Maxwell-Garnett models for a simple Au/H <sub>2</sub> O system at 1000 cm <sup>-1</sup> . The Maxwell-Garnett model fails to predict a nontrivial percolation threshold, where the percolation threshold at $f = 0.33$ is apparent in the Bruggeman model.	31
Figure 2-7: Dispersion relations for: x-component of a polariton in Si prism at 45 degrees AOI (blue); photon in vacuum (orange); Surface plasmon-polariton (SPP) mode at Au-air interface (green); bulk plasmon of Au (red). The real component of wavevector is shown on the left, and the imaginary component on the right. The bulk plasma frequency is marked with a dashed line and the SPP frequency with a dotted line. <b>Propagating</b> SPPs may be excited at lower frequencies than $\omega_{\text{SPP}}$ while whereas <b>localized</b> SPPs may be excited between $\omega_{\text{SPP}}$ and $\omega_{\text{p}}$ .	36
Figure 2-8: The PSPP momentum-matching condition for the Si/Au interface. The blue trace plots the frequency of the intersection points of $k_{\text{SPP,Au/air}}$ and $k_{x,\text{Si/Air}}$ as a function of angle (e.g., the intersection of the green and blue traces in Figure 2-7). This is the frequency of the PSPP resonance as a function of angle. In the NIR, PSPPs are only able to be excited very near to the critical angle.	37
Figure 2-9: Possible operative plasmonic modes in ATR-SEIRAS experiment involving a layered system of Au composite/ITO/Si.	38
Figure 3-1: Modelled spectral line shapes for bimodality parameters of 1, 0.5 and 0; all plots are normalized to peak heights of unity.	42
Figure 4-1: Two-step Bruggeman approach for coated particles. The resulting permittivity of the first instance of the Bruggeman model is used as an input to the second instance.	45
Figure 4-2: Program output visualizing an ellipsoid oriented off-axis with respect to the applied field; rotated 20° counterclockwise about the [111] axis. The rotation matrix is the matrix which will transform the local basis vectors of the ellipsoid	

(saturated RGB vectors) into the desired coordinate system of the applied field (dull RGB vectors).	58
Figure 5-1: A) Real ( $n$ ) and imaginary ( $\kappa$ ) refractive index of a CMO calculated by Drude model (parameters extracted from external reflection spectra); B) p-polarized external reflectivity spectrum calculated for air/25 nm of CMO/Si.	60
Figure 5-2: In-plane wavevector components of PSPP at the interface between the Si prism and CMO interface for: A) metal-like CMO and B) dielectric-like CMO. The intersection between the PSPP wavevector (red) and the wavevector of the excitation polariton in the Si prism (indigo to teal at AOIs from 17.1° to 90.0°) indicates the conditions (frequency, angle and wavevector) where a PSPP may be excited.	63
Figure 5-3: Wavevector matching condition for the Bruggeman-modelled Au-composite/H <sub>2</sub> O interface. The frequency and AOI of each intersection between $k_x$ (PSPP Bruggeman/H <sub>2</sub> O) and $k_x$ (Si) is plotted to identify possible PSPPs.	64
Figure 5-4: Experimental external reflectivity spectra of an as-deposited (unannealed) 50 nm ITO film demonstrating the excitation of an ENZ mode at $\sim 4200 \text{ cm}^{-1}$ .	65
Figure 5-5: Ratio of p- to s-polarized modelled reflectivity spectra for the Si/ITO/H <sub>2</sub> O system. The 30 nm film (A) demonstrates an ENZ mode, while the 160 nm film (B) demonstrates a PSPP whose frequency is angle dependent. The feature beyond $14000 \text{ cm}^{-1}$ is a nonresonant phenomenon resulting from the ITO acting as an interference antireflection coating. <sup>49</sup>	66
Figure 5-6: Absorbance peak height as a function of the extent of Au deposition for different CMO underlayers.	69
Figure 5-7: Calculated bimodality parameter (as defined in section 3.2) as a function of extent of Au deposition for different CMO underlayers. A) shows experimentally derived data, and B shows the analogous Bruggeman-modelled data.	70
Figure 5-8: Overall substrate reflectivity as a function of deposition for different underlayers. A) plots the detector counts of the sample single beam spectrum as a stand-in for the reflectivity while B) is the directly computed sample reflectivity averaged over the entire spectral range.	71
Figure 5-9: SEM of SEIRAS film to extract parameters for EMA modelling.	73
Figure 5-10: Representative SEMs of electrodeposited Au on annealed ITO for the stated charges.	74
Figure 5-11: Angle-dependent SEIRAS of $\nu_{CN}$ mode of cyanate for p- and s-polarized light.	75

Figure 5-12: Comparison of enhancement and spectral line shapes for traditional all-metal SEIRAS films and ITO/Au composite films. The markers represent experimental data points calculated from the spectra shown in Figure 5-11. The experimental absorbance data was normalized such that the point at 40 degrees lies on the calculated curve. 76

Figure 5-13: Electric field strength calculations for: yellow trace: Si, 25 nm Au, 25 nm composite, H<sub>2</sub>O; purple trace: Si, 25 nm ITO, 25 nm composite, H<sub>2</sub>O. 78

Figure 5-14: From left to right: calculated RI, absorbance, and reflectance for the 3-phase Bruggeman formula for spheres containing metal, organic, and water. Reflectivity and absorbance are calculated at 60 degrees using p-polarized light. These plots were calculated at  $f = 13$ , however the product of the normalized  $n$  and  $\kappa$  values (dashed green trace) matches the line shape of the absorbance fairly well at all values of  $f$ . 81

Figure 5-15: The refractive indices of a 2-phase Bruggeman composite are in lavender while the permittivities are in blue. The fill-factor increases from left to right; the first column  $f = 0$  corresponds to pure organic ( $\eta_{\text{org}}$ ), while the last column  $f = 1$  corresponds to pure metal ( $\eta_{\text{met}} = 1 + 30i$ ). The organic is modelled as a Lorentz oscillator with parameters:  $\nu_0 = 1500 \text{ cm}^{-1}$ ;  $\gamma = 20 \text{ cm}^{-1}$ ;  $\epsilon_\infty = 1.5$ . The top row plots  $\eta$  or  $\epsilon$  on the complex plane, while the bottom two rows plot the components as a function of frequency. When  $f = 1/3$ ,  $\epsilon_{\text{BR}}$  is dominated by the product of  $\eta_{\text{met}}$  and  $\eta_{\text{org}}$ , which manifests as a rotation and scaling of the  $\eta_{\text{org}}$  in the complex plane (top row,  $\eta_{\text{org}}$  in the first column is rotated and scaled to give  $\epsilon_{\text{BR}}$  in the middle column). This appears in the individual components as a swap of their line shapes and an inversion in the Lorentzian (bottom rows, middle column). 83

### V.iii List of Abbreviations

AOI	Angle of incidence
ATR	Attenuated total reflectance
CAD	Computer-aided design
CMO	Conductive metal oxide
CPP	Capacitive plasmon-polariton
DC	Direct current
EBL	Electron beam lithography
EMA	Effective medium approximation; equivalent to EMT
EMT	Effective medium theory; equivalent to EMA
ENZ	Epsilon near zero mode
FDTD	Finite difference time domain
FWHM	Full width at half-maximum
GEMT	Generalized effective medium theory
IR	Infrared
ITO	Indium tin oxide ( $\text{In}_2\text{O}_3/\text{SnO}_2$ )
IZO	Indium zinc oxide ( $\text{In}_2\text{O}_3/\text{ZnO}$ )
LSPP	Localized surface plasmon-polariton
MEF	Metal enhanced fluorescence
MG	Maxwell-Garnett
MOP	4-methoxypyridine
PM-IRRAS	Polarization-modulated infrared reflection-adsorption spectroscopy
PSPP	Propagating surface plasmon-polariton
PVD	Physical vapour deposition
QCM	Quartz crystal monito
RF	Radiofrequency
RI	Refractive index

RMS	Root mean square
s-SNOM	Scattering type scanning near field optical microscopy
SBP	Screened bulk plasmon
sccm	Standard cubic centimetres per minute
SE	Surface enhanced
SEIRAS	Surface enhanced infrared absorption spectroscopy
SEIRS	Surface enhanced IR scattering
SERS	Surface enhanced Raman spectroscopy
SHINERS	Shell-isolated nanoparticle-enhanced Raman spectroscopy
SNR	Signal to noise ratio
SPP	Surface plasmon-polariton
SPR	Surface plasmon resonance
TCO	Transparent conducting oxide
TERS	Tip-enhanced Raman spectroscopy

# 1 INTRODUCTION

Vibrational spectroscopy is an incredibly useful technique for obtaining molecular structural information. Surface-enhanced (SE) spectroscopy further extends this utility as an analytical method by introducing a metal surface in the vicinity of the molecules, which greatly increases the sensitivity of the measurement and enables the possibility of electrochemical control. SE spectroscopy promises a wide range of applications, from studying the selective adsorption of molecules on single crystallographic facets, to the design of more active catalysts with lower precious metal usage. Enzyme-based sensors have been made by tethering biomimetic membranes onto metal surfaces, and SE techniques are powerful tools for characterizing such sensors.<sup>1</sup> An exciting proposed use of surface-enhanced spectroscopy involves microfluidic devices supported on top of an internal reflection element (IRE) to direct an IR beam at certain points along the channel.<sup>2</sup> Thin film electrodes can be deposited on top of the IRE which are used to drive redox reactions. IR measurements allow the reaction's progress to be monitored in situ and are used as the basis for control signals for pump systems. This could find application in low volume, high throughput automated research by running many devices in parallel or potentially even in commercial manufacture of drugs on a small scale. By and large, however, the major application of SE spectroscopy is as a research technique for studying electrochemical reactions involving catalytic surfaces.

As SE techniques mature and find more applications, new substrates will need to be designed. A particular metal may be required to catalyze some reaction in lieu of the commonly used coinage metals, or perhaps a functional group needs to be anchored to the surface to bind a target analyte. The SE technique of interest in this thesis is attenuated total reflection (ATR) surface-enhanced IR absorption spectroscopy (SEIRAS), and details of this technique will be explained below. Traditionally, substrates for ATR-SEIRAS have been produced by depositing gold or silver films directly on the surfaces of suitable IRE materials such as Si, ZnSe or Ge. Although these modified substrates can provide strong apparent surface enhancements, the films are notoriously irreproducible, fragile, and prone to failure during measurements. In 2019 the

Burgess group reported the advantages of depositing a buffer layer of conductive metal oxide (CMO) on the IRE upon which a gold film could be grown by electrodeposition.<sup>3</sup> This approach provided high enhancement factors and unprecedented film stability. This approach has also, very recently, been shown to be amenable for generating SEIRAS active layers of electrocatalytically important metals such as palladium.<sup>4</sup> However, the core reasons for the improved optical performance of the CMO-modified SEIRAS approach were poorly understood prior to this thesis work. This is a fundamental knowledge gap which must be confronted to understand how to maximize (or balance) the enhancement, conductivity, and transparency of the substrate, depending on the application. A basic understanding of the underlying physics and a model to predict the optoelectronic properties of a composite film is imperative. The primary goal of this thesis is to develop a model of the permittivity of a composite film using effective medium approximation (EMA) and evaluate its predicted SEIRAS performance and compare model-based results to experimental spectra.

## 2 BACKGROUND

Implementing an EMA model requires a knowledge base which is not part of the training of an average chemist. Thus, the substantial background section presented here aims to provide context for a general chemistry audience. In brief, the choice of utilizing ATR-SEIRAS is discussed and compared to other surface-enhanced techniques (section 2.1). A basic discussion of electromagnetics (2.2) provides context for the EMA approach and the Drude-Lorentz model is introduced (2.3), which will later be used to compare the properties of conductive metal oxide (CMO)-supported composite films to traditional all-metal films. This is followed by a brief overview of the transfer matrix method (2.4) which is used to calculate experimentally measurable properties, like reflectivity and absorption spectra. A few comments are provided on percolation theory (2.5) before an in-depth discussion of the effective medium approximation approach (2.6). Finally, a review of plasmonic enhancement mechanisms (2.7) is presented as a question that continually arose during this work: are plasmonic mechanisms operative in SEIRAS generally and in CMO-metal substrates specifically?

### 2.1 Surface-enhanced vibrational spectroscopy

Surface enhanced infrared spectroscopy can be done in transmission,<sup>5,6</sup> external reflection,<sup>7</sup> or internal reflection<sup>8</sup> mode. Diagrams of common experimental setups for each geometry are shown in Figure 2-1. A brief discussion of each will provide the rationale for working in internal reflection geometry and provide some context for the aims of this work.

Transmission mode offers a simple beam path and uncomplicated apparatus. Thin metal layers are sufficiently transparent that the IR light may be passed through the film with enough intensity to enable measurements. Transmission mode presents a significant problem for IR spectroscopy of solutions, since the concentration of the solvent is very high (*e.g.*, ~55 M for aqueous solutions) and many common solvents, such as H<sub>2</sub>O, have a significant IR absorption cross-section. This causes a very significant attenuation of light, and the signal to noise ratio (SNR) of the analyte's absorbance is often too poor to be useful.

This leaves reflection-based techniques. Surface enhanced spectroscopies make use of metal films, which initially appear to provide a convenient reflective surface for a specular reflection-based measurement. For analytes which adsorb strongly to the metal film (or to a functionalized metal film), this can be a successful approach. The metal film can be placed in contact with the analyte-containing solution and be "incubated" so that the analyte will adsorb to the surface, and then the reflection spectrum can be measured *ex situ* (*i.e.*, the dry interface with adsorbed analyte). While this approach (called reflection-adsorption IR spectroscopy, RAIRS) is successful, *in situ* methods are often desirable or required. For example, to study adsorption kinetics, the solution must be held in contact with the metal surface during the measurement using an IR-transparent window. The IR beam enters through the window, passes through the solvent, is reflected off the metal and passes back through the solvent and window to be collected by the detector.

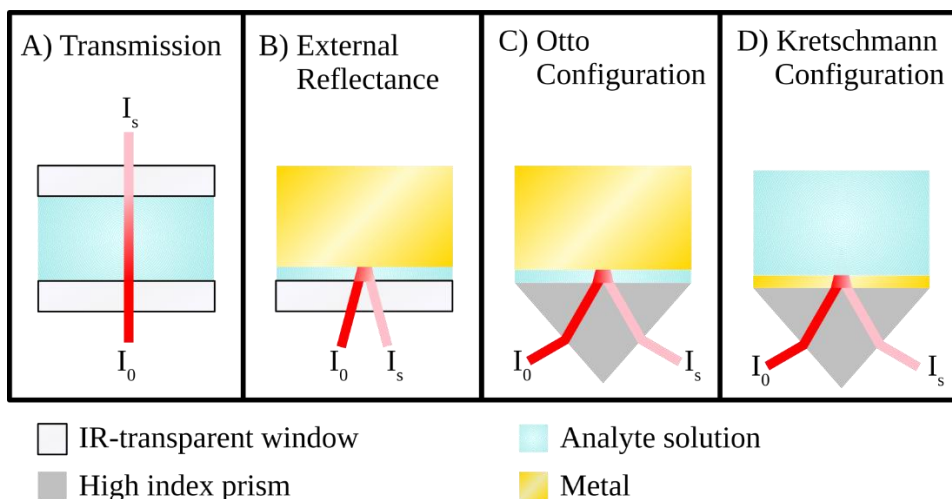


Figure 2-1: Configurations for IR measurements of analyte-containing solutions.

An alternative approach is the so-called "internal reflection" method, where the window is substituted for a high refractive index, IR-transparent prism to bring light to the solution. By Snell's law (eqn. 2-1, where  $n$  is the refractive index and  $\theta$  is the angle of incidence), when light travelling in a high index medium encounters a medium of a lower index, there is an angle of incidence (AOI)<sup>a</sup> where the light will be totally internally reflected back into the high index medium,

---

<sup>a</sup> In this thesis, the AOI will always be measured from the surface normal.

assuming there are no absorptive losses. This angle is called the critical angle. Light travelling at any angle of incidence more grazing than the critical angle will be totally internally reflected.

$$n_1 \sin \theta_1 = n_2 \sin \theta_2 \quad 2-1$$

Total internal reflection may appear to be a useless phenomenon: if the light is totally reflected from the interface, then how could it provide information about the analyte on the far side of the interface? Although the power is totally reflected in the case of an interface between two non-absorbing dielectrics, electric fields still exist on the far side of the interface. These fields form an evanescent wave, so named because the field strength decays exponentially with the distance from the surface and propagates along the direction of the interface. If there is a lossy material, such as a molecule with an infrared-active mode parallel to the interface that is in the vicinity of the evanescent wave, the fields can excite that mode thereby attenuating the reflected power. The energy carried by the wave can excite rotational and vibrational motions of the molecule which can be further converted to translational motions through molecular collisions. Taking a macroscopic view, this is to say that the energy carried by the incident electromagnetic wave is eventually converted into heat. Since these modes will only dissipate energy of a particular frequency, the power collected by the detector will be reduced only at the frequencies corresponding to the characteristic modes of the absorbing molecule, thereby providing a "fingerprint" which can be used to identify the analyte.

The internal reflection method described above is conventional attenuated total reflection (ATR) IR spectroscopy, without any surface enhancement. The decay of the evanescent wave depends upon the crystal material, analyte, angle of incidence, and wavelength. Using typical values for a mid-IR experiment, the penetration depth (defined as the distance at which the field intensity has fallen to  $\frac{1}{e}$  of its incident intensity) is on the order of 0.5  $\mu\text{m}$ . If a typical bond length is taken to be about 1.5  $\text{\AA}$ , it is clear that the evanescent wave will probe well beyond the first layer of adsorbed molecules and extend into the bulk of solution. For a truly surface sensitive technique, an additional mechanism is required to confine the region probed to within a few nanometers of the interface. Furthermore, to perform electrochemical measurements, the surface of interest must be made electrically conductive.

The first method to confine the evanescent wave to a shallower region than the penetration depth of two dielectrics was described by Otto and the experimental setup (Figure 2-1) now bears his name.<sup>9</sup> A metal is positioned very near (less than the depth of penetration of an evanescent wave) the internal reflecting plane of the prism and the analyte is contained in the narrow gap between the prism and the metal. The benefit of the Otto configuration is that a propagating surface plasmon-polariton (PSPP) can be excited, which will be further discussed in section 2.7. The major challenge of working in the Otto configuration is precisely controlling the width of the gap between the metal and prism which requires the position of the surfaces to be adjustable while remaining highly parallel. If the gap is too large, the evanescent field at the metal interface will be too weak to excite a measurable PSPP. Both RAIRS and the Otto configuration enable the use of monocrystalline metal electrodes, oriented and polished so the adsorption of analytes on different crystallographic planes can be studied. The smooth surfaces used in these techniques are less enhancing than is attainable with roughened polycrystalline films, and the experimental challenges of the Otto configuration has limited its popularity.

Shortly after Otto's publication, Kretschmann and Raether demonstrated that the positions of the metal and the dielectric layer can be swapped (Figure 2-1), and a PSPP is still able to be excited at the metal-solution interface.<sup>10</sup> The metal film must be kept sufficiently thin such that absorption by the metal is minimized, but the Kretschmann configuration has proved to be a very successful approach since depositing a thin metal film is experimentally much simpler than maintaining a very precise gap. In electrochemical ATR-SEIRAS, a thin metal film is deposited directly upon the principal reflection surface of the prism which fulfills both purposes of confining the evanescent field and acting as an electrode. The metal films used are textured rather than continuous, uniform slabs, as will be discussed at length in the following chapters. They are also very thin - much thinner than the wavelength of light used to interrogate the surface - and therefore *the optical properties of these films are different than the bulk metal*. The metal film can thus be placed directly at the IRE-solution interface. The film needs to balance the requirements of being sufficiently metal-like that it is reasonably conductive, but also sufficiently transparent that it does not attenuate too much light. The surface texture of the film is sometimes described as "metal islands" where the metal appears as separated regions with some amount of interconnectedness, similar to an archipelago.

One helpful division that can be used to categorize surface-enhanced techniques is whether the method is “resonant” or “non-resonant”. Figure 2-2 groups some of the most common surface enhanced vibrational techniques into these categories. Resonant techniques use substrates with finely tuned plasmon resonances to maximize the degree of enhancement over a narrow frequency range for a particular application. Producing precise metallic structures (often described as nanoantennae) to obtain the highest sensitivity presents a huge experimental difficulty and requires the use of sophisticated, low throughput techniques such as electron beam lithography. Since the aim is typically to obtain the highest enhancement, Raman has dominated the field of enhanced vibrational spectroscopy. By Fermi’s golden rule, the probability of an *absorption* event is proportional to the square of the electric field. Since Raman is an inelastic *scattering* process, it involves two photons: the incident photon and the scattered photon, where the probability of each event is proportional to the square modulus of the electric field,  $|E|^2$ , and therefore the entire transition probability scales with an  $|E|^4$  dependency.

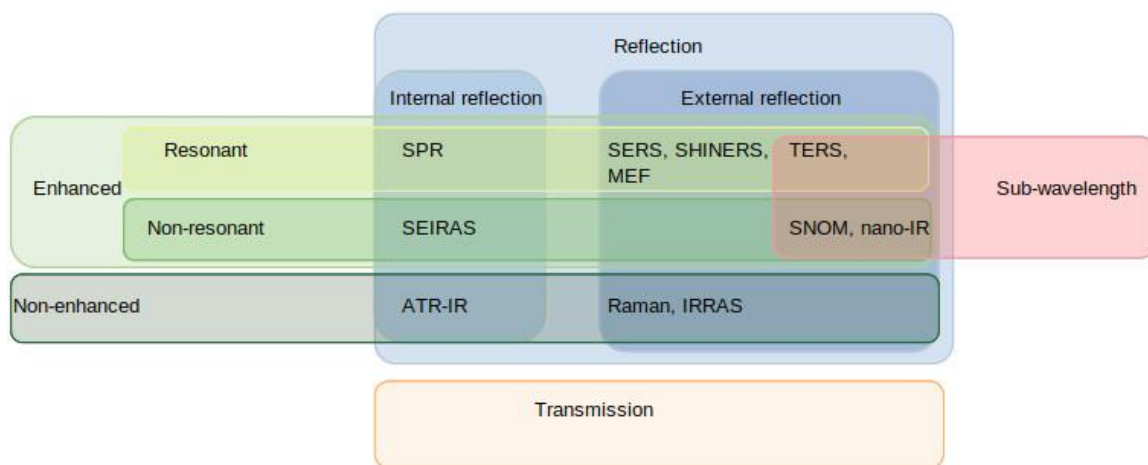


Figure 2-2: Situating ATR-SEIRAS in the scheme of vibrational spectroscopic techniques.

Alternatively, non-resonant SEIRAS utilizes relatively simple methods to produce textured metal films which offer a broadband response but with reduced enhancement factors typically in the range of 10-1000. In contrast to the well-defined structures required for resonant techniques, the films used in ATR-SEIRAS are usually poorly characterized and contain a broad range of particle shapes and sizes. The most typical film preparation techniques are physical vapour deposition and electroless deposition, which do not provide much control in creating films with a specific morphology to obtain optimal performance. By changing the deposition rate, it is possible

to adjust the RMS surface roughness somewhat, but the variance of the roughness is large and the range of features sizes that can be produced is limited.<sup>11</sup> Electrochemical annealing may improve the performance of the film by restructuring the metal surface, but again does not afford a high level of control. Non-resonant films do have some advantages: they are much simpler and cheaper to manufacture, and they offer a broad band spectral response which, as a general diagnostic tool, is preferable to a sensor optimized for maximum sensitivity over a narrow spectral range.

### 2.1.1 Motivation for Using ATR-SEIRAS

Following the above review of surface-enhanced vibrational techniques, it is important to address why ATR-SEIRAS is worth studying. For a commercial sensor designed for a particular analyte, surface plasmon resonance (SPR) offers much improved sensitivity and selectivity. In terms of absolute detection limits, SEIRAS cannot compete with the single-molecule detection limits offered by surface enhanced Raman spectroscopy (SERS).

The largest advantage offered by ATR-SEIRAS is its combination with electrochemistry for the spectroscopic observation of the electrode-solution interface. Spectra can be collected while potentials are applied to the electrode and the signal collected is largely confined to molecules adsorbed on the electrode surface. The characteristic vibrational peaks offer excellent selectivity and provide a high degree of confidence for molecular identification. Quantification of adsorbed molecules is certainly challenging due to the variable nature of the substrates, however it is possible.<sup>12</sup> Unlike SPR which essentially just provides a binary response (has the SPR angle shifted or not), SEIRAS can provide information regarding the structure of the interface, such as the orientation of adsorbed molecules.<sup>13</sup>

The advanced nanoantennae structures used in resonant spectroscopic techniques are well-described by finite difference time domain (FDTD) and similar computational methods, but are not easily applicable to extensive, difficult to mesh structures utilized as ATR-SEIRAS substrates. The motivation for the work presented here is to assess the explanatory power of EMA as applied to the less well-defined substrates which are widely used in electrochemical ATR-SEIRAS, in particular, metals electrodeposited onto CMOs. This EMA-based model aims to guide the development and optimization of films using electrodeposition and nanoparticle film deposition techniques, which offer a greater degree of control of the film properties relevant to ATR-SEIRAS

compared to the historically used techniques of physical vapour deposition (PVD) and electroless deposition.

### 2.1.2 Modern Approaches in ATR-SEIRAS

Traditionally, metal enhancing films have been produced by PVD techniques such as was used by Hartstein *et al.*<sup>14</sup> in the first report of SEIRAS. Since Miyake *et al.*<sup>15</sup> published an electroless deposition procedure for Au films onto a hydrogen-terminated Si surface, this has also become a popular technique. Producing a robustly adhered film that exhibits enhancement is a significant challenge. These traditional methods suffer from significant inherent variability in the resulting films, even with rigorous adherence to a standardized procedure. Unfortunately, there is currently no way of assessing if a particular film will exhibit enhancement prior to using it and empirically testing its optical response. If the film is SEIRAS-inactive, electrochemically annealing the film (cycling the applied potential in the presence of molecules which weakly bind to the metal) can re-texture the surface,<sup>16</sup> but success in SEIRAS activation is not guaranteed. Furthermore, traditional SEIRAS films are notoriously fragile, with delamination being the most common failure mode. Metals have poor wettability on common IRE materials, such as Ge<sup>17</sup> and Si<sup>18</sup>, which allows for the formation of metal islands, but yields delicate films. Delamination is exacerbated by applying highly reducing potentials. The evolution of hydrogen bubbles stresses the film and creates buoyant forces which lift the film off the IRE. Long term stability is poor, especially with extended aqueous contact, such as the electrolyte used during a typical electrochemical experiment. Scrupulous cleanliness is required to successfully deposit films. Using adhesion layers is not possible for electroless deposition which uses HF to etch the Si surface. For vacuum-deposited films, the use of adhesion promoters such as Ti, Cr, and W<sup>19</sup> often causes the metal overlayers to be too smooth, which completely suppresses all enhancement.<sup>17</sup>

Another approach to deposit a SE film involves synthesizing a suspension of nanoparticles and depositing them as a thin film on top of the principal reflecting plane. This approach has been utilized for external reflection techniques for several decades, for example glassy carbon electrodes can be decorated with metal nanoparticles,<sup>20</sup> but this approach has not been utilized extensively for ATR-SEIRAS until recently.<sup>21,22</sup> Synthesizing nanoparticles *ex-situ* and then depositing them as a film expands the range of particle morphologies considerably as there is a great variety of solution syntheses for obtaining specific shapes and sizes of metallic nanoparticles. Surfactants

and capping agents are often used during the synthesis to keep the particles suspended and removing these protective molecules so that the target analyte can adsorb to the particles presents a challenge. If electrochemical control is desired, the particles can be drop-cast onto a transparent conducting oxide film, such as a CMO which will act as the electrode. This is a considerable advantage since a much larger range of particle loadings can be utilized. With sputtered or electrolessly deposited films, the density of gold must be sufficient such that the film is continuous and is conductive enough to behave as an electrode. This requires that the composite film has a fill factor beyond the metal-insulator transition such that the metal islands are largely connected. At these fill factors, the performance of the film declines from its optimal enhancement, and absorption losses from the metal become more pronounced. To reiterate, the film must perform two functions: 1) act as a conductive electrode and 2) confine the EM fields and provide the electromagnetic field enhancement. By introducing an underlayer, the roles can be separated, and the overall performance improved. The underlayer can be designed to provide suitable conductivity while maintaining sufficient IR transparency. Furthermore, the textured metal film can be optimized to maximize enhancement while yielding acceptable spectral line shapes, without any concern about its conductivity. The adhesion of some CMOs to Si IREs is extremely good,<sup>3</sup> which improves the reliability of this approach compared to all-metal films and relaxes the cleanliness requirements.

A great variety of nanoparticle shapes have been used for SEIRAS including rods,<sup>23</sup> stars,<sup>24</sup> and cubes.<sup>25</sup> Particles can be encapsulated with a dielectric shell as is done in SHINERS<sup>26</sup> so the fill factor can be increased without the particles agglomerating into a single conductive unit. There are a number of options to deposit suspended nanoparticles into ordered thin films.<sup>27</sup> If homogeneous particles are used, some deposition techniques create large domains of well-defined arrays which are easier to characterize and model and provide less substrate-to-substrate variation,<sup>28</sup> facilitating quantification over traditional vacuum or electrolessly deposited substrates which are notoriously variable in their sensitivity.<sup>17</sup> Simple drop-casting is an option,<sup>24</sup> and while some domains can exhibit excellent ordering, the “coffee ring effect” often prevents long-range ordering on the scale of several square millimetres. Langmuir-type techniques make use of the interfacial surface energy and smoothness of a liquid’s surface to enable self-assembly of protected metal nanoparticles.<sup>29</sup> The films can be transferred from the liquid interface onto a solid support

by drawing the substrate through the film or by draining the liquid below the level of a submerged substrate.

In recent years, preparing surface-enhancing films by metal deposition on top of CMOs has emerged as a viable substitute to more traditional films deposited directly on IREs. As will be discussed at length in subsequent sections, ATR-SEIRAS has not historically relied upon sharp plasmonic resonances to obtain its moderate (generally in the range of  $10$ - $10^3$ ) enhancement factors. Instead a broadband enhancement is obtained largely as a result of confining the electric field of the evanescent wave to very short region of space around the metal film,<sup>30</sup> along with the chemical enhancement effect (section 2.1.4.1). This means that the identity of the metal is not nearly as important as in SERS, where substrates are limited to “plasmonic metals”, largely Ag and Au, which exhibit localized surface plasmon-polaritons (LSPPs) at optical wavelengths where Raman excitation lasers operate. Many metals have been used as enhancing layers for SEIRAS including Fe,<sup>31</sup> Ni,<sup>32</sup> Pb,<sup>33</sup> Pt,<sup>34</sup> and Sn<sup>35</sup> among others.

Electroreduction of metal salt precursors to metallic films using a CMO electrode offers a convenient method to deposit a wide variety of metals. This has a number of advantages. First, the wettability of metals on common IRE materials is very poor. Although this has been exploited as a texturing method by "dewetting" (heating to increase the mobility of the metals and allowing surface tension to cause the film to bead up), it is generally a disadvantage due to the poor mechanical stability of the films. By contrast, CMOs generally have excellent adhesion to IREs (*e.g.*,  $\text{In}_2\text{O}_3$  on  $\text{Si}/\text{SiO}_2$ ) and moderate adhesion to metals and thus act as a bonding agent to adhere the metal to the IRE. As per their name, CMO films are conductive and will therefore electrically connect the metal particles when utilized as an underlayer. This enables a much wider range of metal densities to be used, while still operating as a continuous electrode. Even sparsely loaded films which are well below their percolation threshold, can be charged as a single electrode. The CMO layer also enables the possibility of electrodeposition of metallic films by reduction of metal salt precursors. Films produced by electrodeposition allow for much more control over the morphology and are generally less smooth (and therefore more enhancing) than films prepared by sputtering. Shape-directing ligands can be used to selectively adsorb onto specific crystallographic facets, hindering growth along those axes, enabling the exclusive growth of a particular shape.<sup>36</sup>

Also noteworthy are graphene-based substrates whose SPP modes may be tuned by chemical doping.<sup>37</sup>

### 2.1.3 Spectral Line Shapes

Absorbance spectral line shapes deviating from the ideal Lorentzian are widely reported in the literature for surface enhanced vibrational spectroscopies,<sup>7,38,39</sup> and a useful model should be capable of predicting this phenomenon. Non-Lorentzian lineshapes have been called “anomalous line-shapes” and range from slightly asymmetric to bimodal to fully inverted. Numerous explanations have been provided in the literature,<sup>20,38,40</sup> but it is important to recognize that no new phenomena need to be invoked to account for this behaviour: it is simply a consequence of the presence of an absorbing film on a moderately reflecting substrate. Perhaps the most complete account explaining the cause of the unexpected line shapes was provided in the early 2000’s by Pecharroman *et al.*<sup>40,41</sup> In order to gain some intuition, they constructed the simplest system which could still replicate the observed behaviour. As their interest was in explaining results from external reflection geometry experiments, they used a three-layer system of: 1) air, 2) metal nanoparticle film, and 3) a conductive backing layer. To calculate a differential reflectivity spectrum, two reflectivity spectra are calculated with all the same parameters except the permittivity of the composite, which changes upon adsorption of the analyte. Two different scenarios are discussed: when the backing layer is a highly IR-reflecting, metallic electrode and when it is a moderately reflecting electrode, such as glassy carbon or graphite. In the case of moderately reflecting electrodes, Pecharroman *et al.* demonstrated, using the Fresnel equations, that the adsorption of a molecule onto the nanoparticle film may cause an increase in the reflectivity of the interface due to the change in the permittivity of the composite layer upon adsorption. Furthermore, under conditions relevant to a surface-enhancing experiment, even pure metal electrodes can be made to be poorly reflective. Smooth bulk metal surfaces, such as polished electrodes, are known to not exhibit any significant enhancement.<sup>15</sup> To obtain an enhancing surface, the electrode surface may be roughened, for example by the well-known process of “platinizing” a platinum electrode.<sup>7</sup> By electrodepositing Pt on the electrode, a textured film of nanoparticles develops on the surface. This provides the conditions for surface enhancement (high local electric fields at the metal surface), but it also causes the surface to become significantly less reflective, enabling the appearance of asymmetric spectral lineshapes.

The discussion in Pecharroman *et al.* was limited to the external reflection geometry, and was not extended to ATR-SEIRAS, where the principle of total internal reflection is used as opposed to external reflection from a bulk metal electrode. The Au-nanoparticle films supported on conductive metal oxides studied in the course of this work should be considered as moderately reflecting, and as such they visually appear significantly duller than bulk gold. Therefore, the conditions of maximal enhancement (highly textured surface with small interparticle separation) are precisely the same conditions under which bimodal and inverted line shapes are expected to occur.

#### 2.1.4 SEIRAS Enhancement Mechanisms

The mechanism of enhancement in SEIRAS has been debated at length in the literature,<sup>38,40,42,43</sup> and a complete explanation has not been fully developed. Broadly, accounts for the enhancement are separated into two main categories: chemical and electromagnetic. Both are active in any enhancing surface, although the dominant mechanism depends on the morphology of the surface.

##### 2.1.4.1 Chemical

The enhancement provided by the poorly defined roughened metal surfaces commonly used by electrochemical ATR-SEIRAS practitioners is likely best attributed to chemical enhancement. The chemical mechanism emphasizes the change in polarizability of a metal particle upon the adsorption of some analyte. This change in polarizability causes a change in the permittivity of the composite metal film and the change is most pronounced at resonant vibrational frequencies of the analyte. IR absorption by a material implies anomalous dispersion in its permittivity function in the spectral region of the absorption ( $\frac{\delta\epsilon}{\delta\omega} < 0$ ). This perturbs the polarizability of the metal particles most strongly at the absorption frequencies of the analyte, so the SEIRAS spectrum has absorption features corresponding to the spectrum of the analyte. Effective medium theory has proven to be a highly informative approach in modelling the changes in polarizability upon adsorption.<sup>44</sup>

##### 2.1.4.2 Electromagnetic Mechanism and Plasmons

The electromagnetic explanation invokes surface plasmon-polaritons (SPPs) and the corresponding high local field strengths around metal particles as the reason for enhanced IR signals (see detailed discussion in Section 2.7). By Fermi's Golden Rule, the probability of a photon-induced transition between vibrational eigenstates is proportional to the square of the electric field amplitude, and increased absorption seen in surface-enhanced spectra is accounted for by the increased electric field strength. Pointy, high aspect ratio structures create especially large field strengths by the "lightning-rod" effect, which concentrates the electric field in a small region.<sup>45</sup> Gaps between adjacent particles are hotspots which account for large portions of the observed signal.<sup>46</sup> Researchers working with "resonant" surface enhanced IR scattering (sometimes denoted SEIRS in comparison to SEIRAS) use well-defined structures produced by metal deposition through two-dimensional arrays of polystyrene beads (colloidal lithography) or electron beam lithography which have sharply defined resonance positions. Near-field effects are dominant in these resonant nanoantennae, where the scattered fields cause enhancement which falls off with a distance to the fourth power dependency.<sup>47</sup> Finite difference, time-domain (FDTD) numerical approximations to Maxwell's equations can be applied to such geometrically well-defined systems and allows field strength maps to be calculated around particles. High field strengths are apparent in the immediate vicinity of the particle surfaces where adsorbed molecules would be found. The enhancement factors for these carefully engineered structures are typically higher (up to  $5 \times 10^5$  for SEIRS compared to  $1 \times 10^3$  for the poorly-defined roughened films used in SEIRAS),<sup>47</sup> however, their spectral range of enhancement is narrower. Scattering scanning near-field microscopy (s-SNOM) has been a useful tool to experimentally measure the highly localized (sub-diffraction-limited) enhancement of nanoantennae in order to investigate the electromagnetic enhancement mechanism.<sup>48</sup> In addition to localized and propagating SPPs, there has recently been growing interest in investigating a plasmonic mode related to the bulk plasmon which may be excited for very thin conductive films.<sup>49</sup> The potential role of these three different types of SPPs in the CMO-based ATR-SEIRAS substrates is also explored in this thesis.

### 2.1.5 Approach to Address Open Questions in ATR-SEIRAS

In light of the above introduction to surface-enhanced spectroscopy, it is clear that while the field is very broad, there is still much to be investigated and interpreted. The surface-enhanced vibrational spectroscopy community has placed much emphasis on the level of enhancement

provided by different surfaces and focused much of its attention on the empirical-based development of ever more enhancing substrates. Somewhat less attention has been directed into understanding the anomalous spectral line shapes and obtaining a firmer theoretical basis to guide the development of better substrates.

Irrespective of the enhancement mechanisms operative in ATR-SEIRAS substrates, having a model that can predict ATR-SEIRAS behaviour is highly desirable. Such a model should account for the observed spectral line shapes. As will be shown in the following sections, the transfer matrix method (TMM) combined with an EMA model for the permittivity of the composite film is very successful at reproducing experimental results, despite not offering much in the way of assigning a clear enhancement mechanism as described in the preceding section. Since many SE spectroscopists do not have extensive training in physics, there has not been an easily accessible account of how to select, implement and draw conclusions from EMA-based modelling. Finite-element-based models for determining the response of well-defined substrates are often performed using commercial software, and a firm grasp of the underlying math is not required for most practitioners. Conversely, numerous researchers have utilized EMA for modelling broadband enhancing surfaces, and this thesis aims to describe and review this approach as it pertains to ATR-SEIRAS.

This concludes the background information regarding surface-enhanced vibrational spectroscopy in context for the work presented in this thesis. The remaining subsections in the background chapter (2.2 to 2.7) will present several topics which may appear somewhat peripheral to the motivation presented above, but details of these topics are important to understand the modelling approach and analysis. The chart presented in Figure 2-3 demonstrates how each background section discussed relates to the broader schema of this thesis.

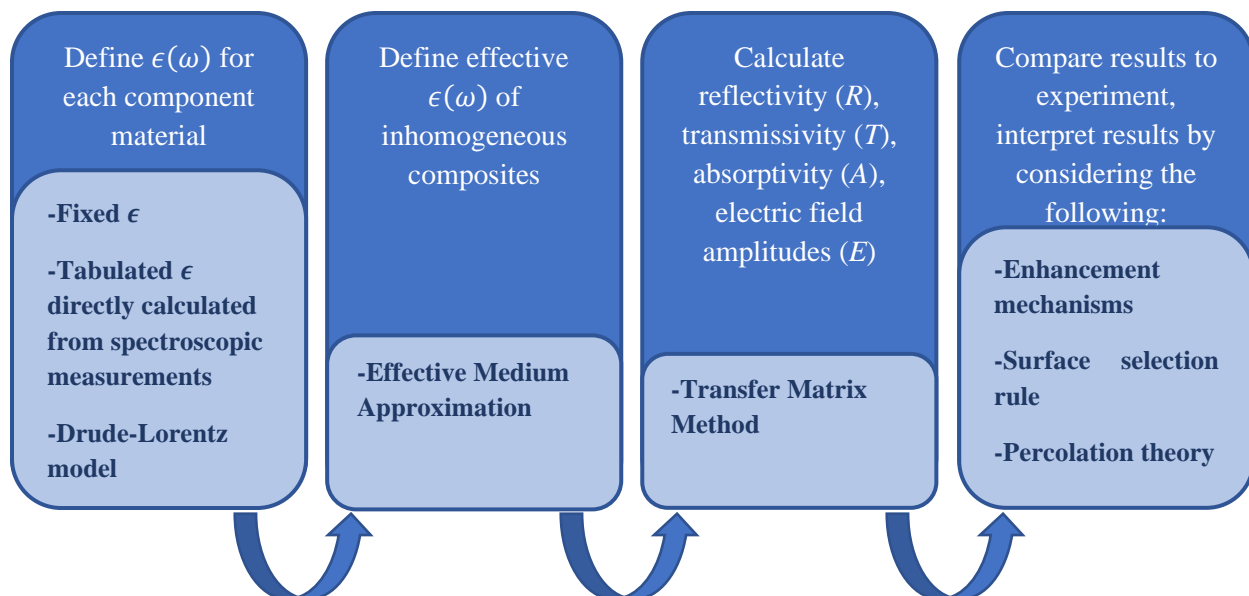


Figure 2-3: Framework locating the background topics to be presented in the following subsections.

## 2.2 Basic Electromagnetics Background

As previously mentioned, this thesis requires a familiarity with basic electromagnetic theory beyond what is encountered in the training of the average chemist. This section introduces the core aspects of electromagnetic theory needed to appreciate the underpinning physics associated with the EMA approach and modelling of ATR-SEIRAS systems.

### 2.2.1 Classical Electromagnetic Approach

To consider the physical interactions occurring on a microscopic scale in an ATR-SEIRAS experiment is to be faced with an extremely complex multi-body scattering problem from each of the constituent molecules. The scale of the problem is insurmountable -- each scatterer has many degrees of freedom, and each adds another equation. Rather than attempting to solve the resulting system of equations, one can adopt an approach that is analogous to how classical thermodynamics foregoes the need to understand the minutia of the individual interactions to describe observable macroscopic effects. Electrodynamics is akin to thermodynamics in this approach: experimentally accessible parameters are generally macroscopic, but the underlying interactions which cause a particular behaviour are microscopic. A collection of gas molecules is most completely described by the kinetic energy of each individual molecule, but usually the best that can be measured is the

temperature. It is meaningless to ask, "What is the temperature of an individual molecule?", since temperature is an emergent, macroscopic property of a collection of molecules. In a similar way, the refractive index of a material is an analogous property in electrodynamics. Although the most complete description involves interactions on the scale of individual scatterers, the refractive index is a useful macroscopic property which describes the system on a scale which allows for the development of optical devices which are useful on the "human scale".<sup>50</sup>

One might imagine that being able to link the microscopic description with the macroscopic one would open the possibility of designing materials on the nano scale which have useful properties on the macro scale. Indeed, this is the goal of EMA: to compute the average results or "effective" properties on the macroscopic scale, using microscopic parameters to define the system, but without having to rigorously calculate the response function for each constituent particle. EMAs therefore link the microscopic structure of a system to the observable response of that system in a way that can be readily calculated.

### 2.2.2 Permittivity and Permeability

The electrical permittivity and magnetic permeability are a measure of how well a material polarizes and magnetizes in response to electric and magnetic fields, and hence govern the propagation of electromagnetic waves through that material. The constitutive relations (equations 2-2 and 2-3) describe the induced fields (displacement field,  $\mathbf{D}$  and the magnetic flux density,  $\mathbf{B}$ ) in terms of the applied fields (electric field,  $\mathbf{E}$  and magnetic field  $\mathbf{H}$ ). Although the relations appear simple, the permittivity and permeability are in general complex quantities. Additionally, the permittivity is not a simple scalar, in general. Real materials are dispersive, which is to say that the permittivity depends on the frequency of the applied field. This provides a framework for the different spectroscopic techniques. Transitions between various energy states occur at different energy levels, and therefore different portions of the EM spectrum are useful in determining particular kinds of information. X-rays are at the same energy as of core electron transitions, UV-Vis deals with valence electron transitions, IR with vibrational transitions and RF with nuclear spin transitions. Each of these transitions manifests itself as a change in the permittivity at the particular frequency of the difference in energy states of that transition. There are various models to describe the permittivity of a material as a function of energy, the most relevant to this work being the Drude-Lorentz model (section 2.2.3).

Furthermore, for anisotropic materials, the permittivity depends upon the direction of the applied field, and therefore it is often given as a 2<sup>nd</sup> rank tensor ( $3 \times 3$  matrix) which acts on the 3-dimensional  $\mathbf{E}$  vector. Birefringence and dichroism refer to anisotropy of the refractive index and the absorption coefficient, respectively. The physical origin of anisotropy arises from non-cubic crystal structures or from aligned particles. In certain uncommon materials, the permittivity may even be time-variant. For these nonlinear materials, the simple constitutive relations do not apply since the permittivity itself is a function of the applied field.

In this work, the materials under consideration are nonmagnetic, and so it is assumed that the relative permeability is unity and is therefore often omitted from various equations for clarity. For simplicity, the relative permittivity (equation 2-4) is usually reported, which is a unitless value obtained by dividing the true material permittivity by the permittivity *in vacuo*,  $\epsilon_0$ . The vacuum permittivity and permeability are linked by the fundamental property of the free space impedance (equation 2-7). While a material's permittivity is the fundamental physical property, it is convenient to define the complex refractive index,  $\eta$ , which is frequently a more intuitive parameter. For example, the real part of the refractive index describes the ratio of the phase velocity of EM waves in a material to the velocity *in vacuo*.

$$\mathbf{D} = \epsilon \mathbf{E} \quad 2-2 \qquad \mathbf{B} = \mu \mathbf{H} \quad 2-3$$

$$\epsilon_r = \frac{\epsilon}{\epsilon_0} \quad 2-4 \qquad \mu_r = \frac{\mu}{\mu_0} \quad 2-5$$

$$\eta^2 = \mu \epsilon \quad 2-6 \qquad Z_0 = \sqrt{\frac{\mu_0}{\epsilon_0}} \quad 2-7$$

### 2.2.3 Parameters of Electromagnetic Waves

There are several parameters used to characterize electromagnetic waves and the relationship between some common wave parameters are depicted in Figure 2-4. The parameters in blue, namely frequency and period, are fundamental properties of a wave which are the same regardless of medium of propagation (assuming a linear material). To move between the material-dependent parameters in grey and the absolute parameters of the wave in blue, it is necessary to have some information about the material's electromagnetic response. This could be the

permittivity, refractive index, or phase velocity among others. When a wave travels from one medium into another, the frequency (and likewise the period) remains unchanged, although the velocity of the wave and the wavelength (and likewise the wavenumber) will change according to the relation  $f = \frac{v_p}{\lambda}$ , where  $v_p$  is the phase velocity of the wave. The extent to which the velocity and wavelength will change depends upon material's electromagnetic response, which is given by the constitutive relations (eqns. 2-3 & 2-4).

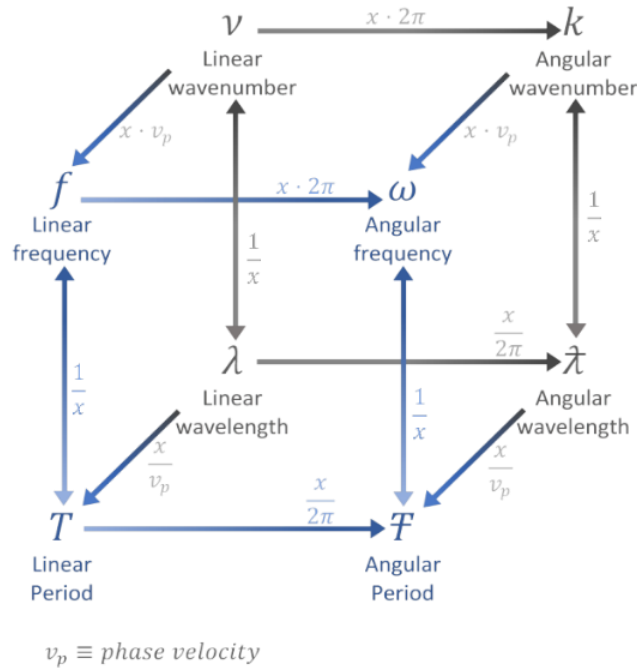


Figure 2-4: Relationships between parameters characterizing waves.

Another common way of describing the frequency of EM waves which is not depicted in Figure 2-4 is by the energy of a photon of that frequency. From quantum mechanics, the amplitude of an electromagnetic wave can only adopt integer multiples of some minimum amplitude, called a quantum. The value of this minimum amplitude depends upon the frequency of the wave, which does not change upon refraction. The energy of a photon is proportional to the square of its amplitude and is given by:  $E = hf$ , where  $h$  is Planck's constant.

### 2.2.4 Surface Selection Rule

When measuring molecules adsorbed to conductive surfaces, as is the case in SEIRAS, a phenomenon called the surface selection rule applies. An electric charge placed next to a metal

will induce an opposite charge in the metal. Although the electric fields are largely confined to the surface of the metal, it is helpful to consider this accumulation or deficiency of charge density as a point source within the metal with equal and opposite charge to the real charge, at the same distance from the interface. This mathematical construct is referred to as an “image charge”, so called because it appears as a reflection of the real charge about the metal interface. This applies equally to induced and permanent dipoles.

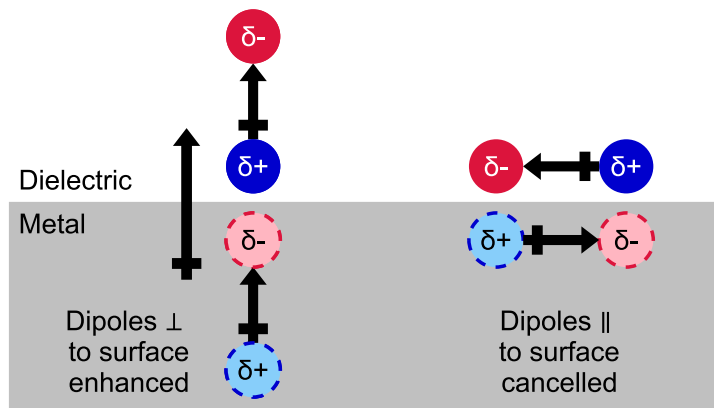


Figure 2-5: Real charges and induced image charges explain the surface selection rule. The arrows indicate the direction of the dipole moment vector.

As can be seen in Figure 2-5, this effect prevents the observation of vibrational modes having their transition dipole moment parallel to the interface since the net electric field is cancelled by the induced polarization of the metal. Conversely, dipole moments perpendicular to the surface are enhanced by the image charges, and so modes involving these moments remain observable. The surface selection rule also has implications for the polarization of the incident light. s-Polarized light has its electric field vector pointed parallel to the interface, and therefore it will excite only the modes which will not be observed, according to the surface selection rule. In contrast, p-polarized light has a component of its electric field vector oscillating normal to the surface, so it will be able to excite modes that are observable. The fraction of the p-polarized component which is normal to the surface is a function of the angle of incidence. At grazing angles, the largest fraction of p-polarized light will be effective in exciting surface-allowed modes, while at normal incidence, the electric field is entirely oscillating in the plane of the interface, where modes are silent. The surface selection rule can be useful in determining molecular orientations by observing the relative intensity of various modes of molecules adsorbed on smooth crystal surfaces compared to spectra of the bulk material.<sup>51</sup>

By this explanation, one should expect to observe the surface selection rule not only at surfaces of metals, but any interface with a conductive material. For materials with a non-negligible impedance, the image charge may not fully offset the real charge, and so vibrational modes that are parallel to the surface may be only partially attenuated. This can be due to insufficient charge carrier density which cannot create an image charge of sufficient magnitude to match that of the real charge. Alternatively, the charge carrier mobility may not be responsive enough to keep pace with the resonant frequency of the oscillation such that the dipole is incompletely annulled.

## 2.3 Drude-Lorentz model

To model the optical response of a material, it is clear from the constitutive relation that the permittivity of the material must be defined. In this work, the Drude and Lorentz models are used to calculate the permittivity of metals and dielectrics, respectively. These permittivities are inputs into the effective medium and transfer matrix models to determine the ATR-SEIRAS response. The Drude-Lorentz model is also invoked to account for many of the differences observed when comparing CMO-supported SEIRAS films to conventional all-metal films.

### 2.3.1 Lorentz Model

The permittivity of a dielectric can be modelled by recognizing that the constituent atoms can be polarized by an external field. The field dislocates the electron cloud from its nucleus, thereby establishing a dipole which exerts a restoring force on the electron cloud. Therefore, the induced dipole behaves as a simple harmonic oscillator. The full derivation is outside the scope of this thesis (see Hecht),<sup>52</sup> but a brief explanation can provide some intuition. By analyzing the forces on the electrons (the massive nuclei are considered to be static), the applied force of the electric field is equal to the sum of the acceleration force, the restoring force and the frictional force. Taking the Fourier transform provides the frequency response from the time-dependent equation. The statistical average of the polarization over all of the induced dipoles allows the material's relative permittivity to be calculated by the Lorentz model (eqn. 2-8), where  $N$  is the number density of electrons,  $e$  is the fundamental charge,  $\omega_0$  is the resonant frequency,  $\Gamma$  is the damping factor and  $m_e$  is the effective electron mass. Different materials have different affinities for the displaced electrons and one method of incorporating this behaviour into the model is to define an

"effective electron mass",  $m_e$ , to account for the material properties which exert forces on the electron and thereby cause it to behave differently than an isolated electron in free space.

$$\epsilon = 1 + \left( \frac{Ne^2}{\epsilon_0 m_e} \right) \frac{1}{\omega_0^2 - \omega^2 - i\omega\Gamma} \quad 2-8$$

The collection of constants in parentheses is defined as the square of the plasma frequency (eqn. 2-9) which has special significance when considering the properties of metals as discussed in the following section.

$$\omega_p = \sqrt{\frac{Ne^2}{m_e \epsilon_0}} \quad 2-9$$

### 2.3.2 Drude Model for Conductors

Although the Lorentz model was presented as describing the permittivity of dielectrics, only a slight modification makes it suitable for modelling electrical conductors. The defining feature of a conductor is that its valence and conduction bands overlap, resulting in a partially filled band of electrons. These conduction electrons are unbound electrons, which have no restoring force, and therefore do not behave as a simple harmonic oscillator. Thus, they have no natural resonant frequency. Instead, the electrons are able to be driven at a range of frequencies, depending upon the frequency of the externally applied field. To obtain the Drude model (eqn. 2-10) from the Lorentz model, the  $\omega_0$  term is set to zero.

If the spectral region of interest is at low frequency, rather than model all of the higher frequency resonances, it is common practice to introduce the term  $\epsilon_\infty$ , the permittivity at infinite frequency. Each resonance at frequencies above the region of interest will add a DC offset to the permittivity, and all of these offsets are combined into the constant  $\epsilon_\infty$ . If every resonance is modelled explicitly, then  $\epsilon_\infty = 1$ .

$$\epsilon = \epsilon_\infty - \frac{\omega_p^2}{\omega^2 + i\omega\Gamma} \quad 2-10$$

In real conductors, as the electrons move through the material, some will collide with other particles, dissipating their energy which is the loss mechanism accounted for by the damping factor,  $\Gamma$ . Often when referring to metals, it may be more intuitive to express the damping of the

oscillation in terms of the relaxation time,  $\tau$ , which is the average time an electron travels in a material before a collision and which is given by  $\tau = \frac{1}{\Gamma}$ .

The plasma frequency is a defining parameter for the optical behaviour of metals. While the unbound electrons in a conductor can oscillate at a range of applied frequencies, there is a limit to the frequency range that can drive a plasma oscillation. Although small, electrons still have some finite mass and correspondingly, inertia, which will resist change to their motion. For low frequencies, the electrons can respond instantaneously to the field, but as the frequency is increased, the response of the electron cloud lags, and the amplitude of the oscillation is damped. The plasma frequency is a measure of the frequency where the optical behaviour of the conductor changes. At frequencies well below  $\omega_p$ , the electron cloud completely counteracts the applied field, screening the metal's interior from the field. Additionally, the imaginary part of the permittivity becomes extremely large at low  $\omega$ , further preventing the field from penetrating into the metal resulting in the very high reflectivity of metals. Microwaves, for example, are perfectly reflected off the walls of a microwave oven, confining them inside. For frequencies in the vicinity of  $\omega_p$ , the conductor becomes quite lossy. At frequencies much greater than  $\omega_p$ , the electrons are not affected by the field. The inertia of the electron is too large to respond at these frequencies and the conductor becomes effectively transparent to these high frequency waves.

### 2.3.3 Generalized Drude-Lorentz Model for Multiple Resonances

Real materials have multiple resonances arising from electronic transitions between energy states. These transitions are also well-modelled as Lorentz oscillators, although the parameters may differ slightly. Each transition contributes another term which can all be summed together to give the overall dielectric function (eqn. 2-11). The term  $G_j$  accounts for the relative strength of different resonances.

$$\epsilon = \epsilon_{\infty} + \omega_p^2 \sum_{j=1}^N \frac{G_j}{(\omega_{0,j}^2 - \omega^2) - i\omega\Gamma_j} \quad 2-11$$

This generalized Drude-Lorentz form is valid for calculating the permittivity of metals, including their interband transitions. The unbound contribution is modelled by setting the first

resonant frequency to zero. Rather than attempting to determine physically accurate values according to the definition of the plasma frequency, reported values are frequently empirically determined in the region of interest. The full width at half maximum (FWHM), peak height and resonant frequency can be calculated from measured spectra, for each resonance, and there are various ways of expressing these parameters in terms of variables into a Lorentz oscillator model. For example, the plasma frequency is often omitted in the context of the dielectrics, and its effect is rolled into  $G_j$ , so care should be taken that the parameters match the specific implementation of the model when using literature values.

## 2.4 Transfer Matrix Method

Once the permittivity of a material is defined (for example, by using the Drude-Lorentz model), some mathematical construct must be employed to calculate the optical response of the material, using the permittivity as a parameter. Determining the permittivity function of a material, whether homogenous or composite, is of little use unless experimentally accessible optical properties such as reflection, transmission and absorption can be subsequently calculated. For systems that are well-described by a stack of thin layers, the transfer matrix method (TMM) is an efficient algorithm to calculate these observable spectra when compared to other methods (FDTD, *etc.*). The TMM is a rigorous method, *i.e.*, it is an exact solution to Maxwell's equations for flat, homogeneous films of infinite extent.

### 2.4.1 Snell's Law and Fresnel Equations

Fresnel<sup>53</sup> developed a series of equations governing the behaviour of waves at interfaces. The reflection and transmission coefficients bearing his name are complex numbers characterizing the reflected and refracted fields (eqns. 2-12 through 2-15). The behaviour of light at an interface depends upon the direction of the electric field of the radiation with respect to the interface, which is called the polarization state of the light. A common way to express polarization is linearly, with respect to the plane of incidence. If the electric field is completely contained within the plane of incidence, this is termed parallel or "p-polarized" (equivalently, transverse magnetic or "TM"). Conversely, if the electric field is perpendicular to the plane of incidence, this is termed "s-polarized" (equivalently, transverse electric, "TE"). All other polarization states can be constructed from linear combinations of p- and s-polarized states.

The directly observable properties, reflectivity,  $R$ , and transmissivity,  $T$  are purely real-valued. One point of caution: the symbol *eta* ( $\eta$ ) is used in the literature both as the electromagnetic impedance as well as the complex refractive index. In this thesis,  $\eta$  always refers to the complex refractive index.

$$r_p = \frac{\eta_i \cos \theta_t - \eta_t \cos \theta_i}{\eta_i \cos \theta_t + \eta_t \cos \theta_i} \quad 2-12$$

$$t_p = \frac{2\eta_i \cos \theta_i}{\eta_i \cos \theta_t + \eta_t \cos \theta_i} \quad 2-13$$

$$r_s = \frac{\eta_i \cos \theta_i - \eta_t \cos \theta_t}{\eta_i \cos \theta_i + \eta_t \cos \theta_t} \quad 2-14$$

$$t_s = \frac{2\eta_i \cos \theta_i}{\eta_i \cos \theta_i + \eta_t \cos \theta_t} \quad 2-15$$

$$R = |r|^2 \quad 2-16$$

$$T_p = \operatorname{Re} \left( \frac{\eta_f^* \cos \theta_f}{\eta_0^* \cos \theta_0} \right) |t_p|^2 \quad 2-17$$

$$T_s = \operatorname{Re} \left( \frac{\eta_f \cos \theta_f}{\eta_0 \cos \theta_0} \right) |t_s|^2 \quad 2-18$$

## 2.4.2 Propagation Matrices

The above Fresnel equations are useful for calculating the behaviour of the interface between *two* materials, but in the case of ATR-SEIRAS, the coated IRE consists of multiple layers. Abeles<sup>54</sup> first developed a transfer matrix formalism to allow for the simple and rapid calculation of stratified layers with *multiple* interfaces. As is discussed in section 2.2.2, anisotropic materials have different permittivity values along its axes. This requires a more sophisticated transfer matrix formalism, such as provided by Passler and Paarmann,<sup>55</sup> however anisotropy was not required to model the ATR-SEIRAS substrates in this work.

## 2.5 Percolation Theory

Percolation theory is a method of describing phase transitions of a geometric network. This is relevant to this work since ATR-SEIRAS films are composites of metallic and insulating particles whose overall character may be either metallic or insulating depending upon the relative proportions of the particles. Percolation theory provides a framework for understanding the metal-to-insulator transition of a composited material purely through geometric considerations. The topic of percolation theory is extensive, but a few concepts relevant to this work bear discussion. One can consider a SEIRAS metal island film as a 2D lattice, where each lattice site is either void or is

occupied by the metal. A primitive model to populate the lattice sites could be to randomly occupy each site with a probability,  $p$ , and then examine the properties of the resulting film. The conductivity of the film could be measured by placing the probes of an ohmmeter on opposite sides of the lattice. At low fill factors, the film will behave as a dielectric, as there is no current path between the probes. As  $p$  is increased, the film will continue to be insulating until a continuously occupied path from one side to the other develops. At this point the conductivity will jump significantly, and this value of  $p$  is called the percolation threshold,  $p_c$ , because the film is said to percolate above this probability. For materials with highly contrasting electronic properties, there is only a narrow range of  $p$  where the property of the effective medium is intermediate to the individual properties. Typically, the effective property is dominated by one of the materials, and the process is analogous to a phase transition. One of the characteristic parameters of such a system is the probability that any occupied site is a part of a “spanning cluster” *i.e.*, one that spans the entire length of the lattice. This probability is called  $P_\infty$  and it can be calculated by  $P_\infty = (p - p_c)^\beta$ . Perhaps the most significant insight of percolation theory was identifying that the critical exponent,  $\beta$ , is a constant and it does not depend on the type of lattice chosen. Other critical properties exist whose behaviour scales with some critical constant.

One useful application of percolation theory to EMAs was provided by Brouers *et al.*<sup>56</sup> using the critical exponents for conductivity and superconductivity obtained from the literature. These exponents are constants, independent of material properties or a system’s geometry, and depend only upon the dimensionality of the system, so they can be obtained from even highly dissimilar systems. The optical threshold, defined as the fill factor,  $f$ , where the real component of the dielectric constant equals zero, can be recalculated using these critical exponents which allows for deviation from the expected threshold of  $f = \frac{1}{3}$  to better match the data.

In 1987, Berthier *et al.*<sup>57</sup> proposed a “space renormalization” procedure in order to better match the simple morphologies modelled by classical EMAs to the actual complex shapes of metal-insulator composites. By thresholding a TEM image, a binary map of the sites occupied by dielectric and metallic particles is obtained. To account for the features occurring at both low and high spatial frequency (micro- and macro-geometry) an iterative approach is used. A grid having cells containing four pixels (2 x 2) is overlaid on top of the binary map. An effective medium is used to calculate the average permittivity of the cell, and thus a down sampled image is

constructed. Another grid is overlaid atop the down sampled image and the process is repeated until the image is reduced to a single pixel representing the entire field of view. The value obtained for this single pixel is the effective permittivity of the medium. This approach is reported to model accurate percolation thresholds, independent of the inherent percolation threshold normally associated with the basic EMAs, and had been successfully applied to textured metal films similar to those used in surface-enhanced spectroscopy.<sup>58</sup>

## 2.6 Effective Medium Approximations

As alluded to in prior sections, EMAs model the permittivity of a layer composed of two or more materials each having a unique permittivity. The permittivity of the component particles may be defined by the Drude-Lorentz model, or by tabulated empirically derived values as a function of frequency. The roughened surfaces used in SEIRAS can be treated as composites of metal, electrolyte, and analyte. EMA only considers a single particle in isolation and accounts for the contribution of the other particles as an effectively homogenous medium. The earliest EMAs assumed only spherical particles and isotropic permittivities, but later modifications extended the theory to ellipsoidal inclusions and allowed for anisotropic permittivities arising either from component particles of inherently anisotropic materials or through geometric means by way of preferential orientation of ellipsoidal particles. The fundamental assumption of EMAs is that the spatial particle distribution is random rather than clustered such that the local field that each particle experiences is equal to that experienced by any other particle.<sup>59</sup> A second assumption is that the particles are sufficiently small as to be ideally polarized dipoles without higher order modes.<sup>50</sup>

The EMA approach is sometimes called mean field theory because it approximates the effect of long-range particle coupling (the far field) by averaging. This is not the full picture of what is physically happening in a SEIRAS film, but it is a reasonable approximation for roughened metal-island films. A major limitation of EMA is that it does not account for the near field particle coupling, so the enhancement provided by any scattering particles that behave as plasmonic antennae will not be modelled explicitly. For large interparticle distances, this is likely not too significant, but as the fill factor is increased, the error has been reported to invalidate even qualitative results.<sup>60</sup>

A note on terminology: in the 1970s literature, EMA or effective medium theory (EMT) often refers exclusively to Bruggeman's model or derivatives thereof. In this work, EMA is a general term referring to a family of models for the effective properties of a composite medium which account for the far field interactions of particles, and which have no particular relation to Bruggeman's formalism. *Table 2-1* summarizes the various abbreviations which have been applied to some common EMAs and provides the relevant equations for comparison.

When searching the literature, it is helpful to recognize that EMAs are used in several domains, and although the terminology may differ, the underlying mathematics is applicable across disciplines. EMA has been applied to calculate a variety of effective properties: conductivity, permittivity, permeability, and elastic modulus. Generally, the expressions for one property are valid for calculating the others. Therefore, it is possible to take an expression for effective conductivity and replace all of the  $\sigma$  for  $\epsilon$  to arrive at a valid EMA expression in terms of permittivity.

Table 2-1: Comparison of common EMA expressions.

Name (Alternative names)	Clausius-Mossotti <sup>50,61</sup> (Lorentz-Lorenz) <sup>61</sup>	Maxwell-Garnett <sup>63,66,67</sup> (Rayleigh Average T-matrix Approximation) <sup>68</sup>	Bruggeman <sup>62-64</sup> (Polder-van Santen) <sup>61</sup> (Bottcher) <sup>61</sup> (Traditional Anisotropic Bruggeman) <sup>65</sup>	Generalized EMT <sup>61,62</sup> (Unified Mixing Formula) <sup>61</sup>
Formulation for randomly oriented ellipsoids	$\frac{\epsilon_{CM,\tau} - 1}{1 + L_\tau(\epsilon_{CM,\tau} - 1)} = \sum_{j=1}^N f_j \frac{\epsilon_j - 1}{1 + L_\tau(\epsilon_j - 1)}$	$\frac{\epsilon_{MG,\tau} - \epsilon_h}{\epsilon_h + L_\tau(\epsilon_{MG,\tau} - \epsilon_h)} = f \frac{\epsilon_{met} - \epsilon_h}{\epsilon_h + L_\tau(\epsilon_{met} - \epsilon_h)}$	$\sum_{j=1}^N f_j \frac{\epsilon_{BR,\tau} - \epsilon_j}{(1 - L_{j,\tau})\epsilon_{BR,\tau} + L_{j,\tau}\epsilon_j} = 0$	$\frac{\epsilon_{eff,\tau} - \epsilon_*}{\epsilon_* + L_\tau(\epsilon_{eff,\tau} - \epsilon_*)} = f \frac{\epsilon_{met} - \epsilon_*}{\epsilon_* + L_\tau(\epsilon_{met} - \epsilon_*)}$ For Maxwell-Garnett: $\epsilon_* = \epsilon_h$ For Bruggeman: $\epsilon_* = \epsilon_{eff}$ For Lorentz-Lorenz: $\epsilon_* = 1$
Expression for spheres only	$\frac{\epsilon_{CM} - 1}{\epsilon_{CM} + 2} = f \frac{\epsilon_{met} - 1}{\epsilon_{met} + 2}$	$\epsilon_{MG} = \epsilon_{met} \left( 1 + \frac{3f \left( \frac{\epsilon - \epsilon_m}{\epsilon + 2\epsilon_m} \right)}{1 - f \left( \frac{\epsilon - \epsilon_{met}}{\epsilon + 2\epsilon_{met}} \right)} \right)$	$\sum_{j=1}^N f_j \frac{\epsilon_j - \epsilon_{BR}}{\epsilon_j + (d-1)\epsilon_{BR}} = 0$ For isotropic geometries (circles, spheres, etc.) of arbitrary number of phases, $j$ , and dimensionality, $d$ .	$\frac{\epsilon_{eff} - \epsilon_h}{\epsilon_{eff} + 2\epsilon_h + v(\epsilon_{eff} - \epsilon_h)} = f \frac{\epsilon_{met} - \epsilon_h}{\epsilon_{met} + 2\epsilon_h + v(\epsilon_{eff} - \epsilon_h)}$ For Maxwell-Garnett, $v = 0$ For Polder-van Santen, $v = 2$ For Coherent Potential Approximation, $v = 3$
Two-phase expression for spherical host	$\epsilon_{CM} = 1 + \frac{f\alpha_{met}}{\epsilon_0 - 3f\alpha_{met}}$	$\epsilon_{MG} = \epsilon_{met} \frac{1 + \frac{2}{3}f\alpha}{1 - \frac{1}{3}f\alpha}$	$\epsilon_{BR} = \epsilon_{met} \frac{1 - f + \frac{1}{3}f\alpha}{1 - f - \frac{2}{3}f\alpha}$	N/A
$f$ : Fractional volume occupied by the particles. $L_\tau$ : Depolarization factor along the $\tau^{\text{th}}$ ellipsoidal semi-axis ( $\tau = a, b, c$ ). $d$ : The dimensionality of the system (usually 3). $N$ : The total number of phases. $v$ : Generalized EMT parameter (unitless).	$h$ : Pertaining to the host. $j$ : For the symmetrical Bruggeman theory, there is no distinction between host and inclusion, and there can be more than 2 constituents. $j$ means pertaining to the $j^{\text{th}}$ phase $\tau$ : Pertaining to the $\tau^{\text{th}}$ principal semi-axis of the ellipsoid. $met$ : Pertaining to the metal. $eff$ : Pertaining to the effective medium.			

A brief overview of the Maxwell-Garnett and Bruggeman models is provided here since they are the most common in the SE spectroscopy literature, but many others have been developed. Although not utilized in this work, it is important to first address the most substantial development in the domain of EMAs in the past 50 years. In 1978, Bergman published a paper<sup>69</sup> linking all possible EMAs in a unified format. Going beyond simple geometric models, Bergman developed a much more generalized approach by using spectral density functions. However, the spectral density function cannot be parameterized in terms of basic morphological parameters, except in “simple” cases where the Bergman representation converges with the classical effective medium models using known mixing rules,<sup>70</sup> so the Bergman representation has not been utilized in this work.

### 2.6.1 Maxwell-Garnett

The major advantages of the Maxwell-Garnett (MG) model are its simple formulation and rapid execution speed. MG is linear with respect to the effective permittivity and does not present any physical root selection problems. MG defines one of the particles as the medium and the rest of the particles as inclusions in this medium. The resulting properties of the effective medium depend upon which medium is considered the host; for this reason, it is labelled as a non-symmetric EMA. This is to say that the effective properties of a medium containing inclusion particles with a certain volume fill fraction,  $f$ , will not give the same result when the particles are designated as the medium and the medium material is designated as the particles having a volume fill fraction  $1 - f$ . One major limitation of the MG model is its complete inability to predict a percolation threshold (except in the trivial cases of  $f = 0$  and  $f = 1$ ). Nonetheless, it has been successfully applied to model plasmonic metal films<sup>71</sup> and under some applications provides better experimental agreement than more complex or physically accurate models,<sup>72</sup> although it will not provide any insight into metal-insulator transitions.

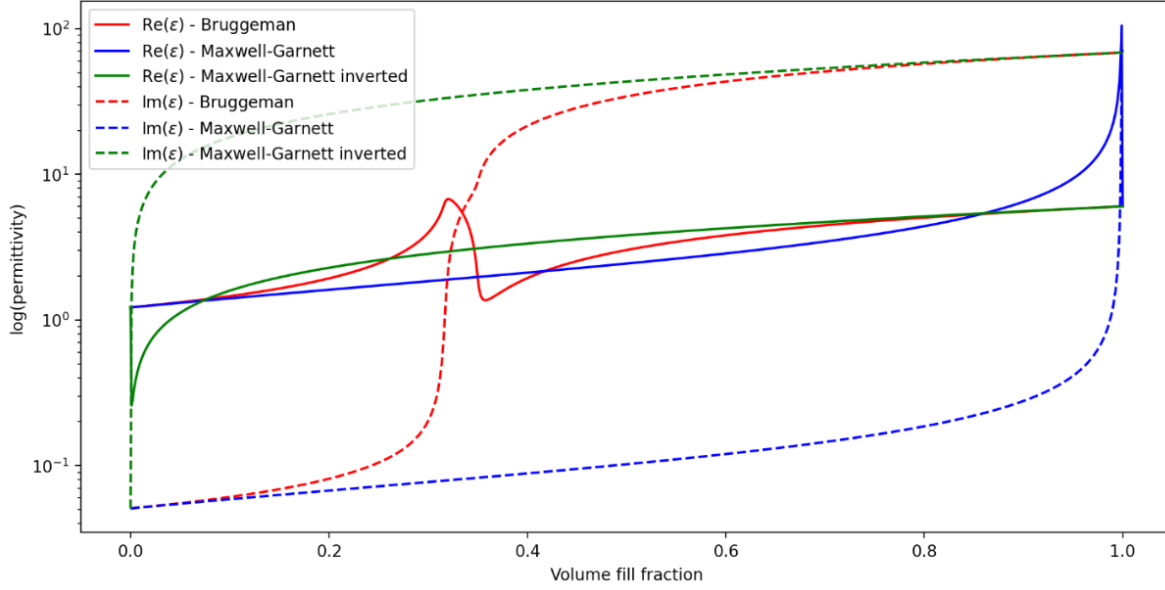


Figure 2-6: Comparison of Bruggeman and Maxwell-Garnett models for a simple Au/H<sub>2</sub>O system at 1000 cm<sup>-1</sup>. The Maxwell-Garnett model fails to predict a nontrivial percolation threshold, where the percolation threshold at  $f = 0.33$  is apparent in the Bruggeman model.

## 2.6.2 Bruggeman

As presented in this work, the Bruggeman formalism is a symmetric EMA and there is no arbitrary distinction of host particles and medium particles. As is shown in Figure 2-6, the Bruggeman model exhibits a metal-insulator transition at approximately  $f = 0.3$ . In the basic two-phase Bruggeman model, the percolation threshold appears at the depolarization factor of the particle. For isotropically-shaped particles, this is simply the reciprocal of the dimensionality: for circles (2D) percolation occurs at  $f = \frac{1}{2}$  while for spheres (3D) the transition occurs at  $f = \frac{1}{3}$ . This is reasonably close to the results obtained by percolation theory for 2D, but incorrect for 3D. Further extensions of the model such as multiple particles with different shapes, or core-shell structures may shift the position of the transition, but it is a limitation of the model that the percolation threshold does not perfectly agree with known experimental data and other percolation models.

## 2.7 Plasmonic Enhancement Mechanism

Resonant SE spectroscopy utilizes structures with sharply defined resonances well-described as plasmonic resonances. Plasmons have also been invoked to explain SEIRAS, but the

language used is often loose and does not follow strict definitions. Although it is part of the electromagnetic enhancement mechanism discussed in section 2.1.4, an overview of plasmons and a discussion on how they are potentially applicable to the CMO-Au SEIRAS substrates used in this thesis merits the following section.

### 2.7.1 Bulk Plasmons and Epsilon Near Zero Modes

Plasmons are quasiparticles arising from the collective oscillation of charge carriers (generally, conduction band electrons). It is important to appreciate the difference between the plasma oscillations described by the Drude model (equation 2-9) and an actual plasmon, as the word "plasmon" is frequently misapplied according to its strict definition. When an EM wave encounters a conductive medium, the charge carriers in the medium will experience a force and will move such that an opposing field is created which counteracts the incident field. This interaction is responsible for the reflectivity of metals; however, this does not constitute the excitation of a plasmon. The plasma oscillation that occurs by irradiating metals with frequencies lower than the plasma frequency,  $\omega_p$ , (eqn. 2-9) has no resonant frequency and it is driven at the frequency of the radiation. Unbound electrons in the vicinity of the photon will screen the rest of the metal from experiencing the field, and so the plasma oscillation will be confined to the surface of the illuminated region. Conversely, bulk plasmons are charge oscillations which *only* occur at a characteristic resonant frequency. Although any individual conduction band electron has no restoring force, when considering an entire block of material, there is an emergent property of the system which appears as a restoring force for the collection of conductive electrons, when treated as a single entity. When an external field is applied, the unbound electrons will experience a force and be displaced from the mean position of the lattice. The negatively charged electron cloud that is dislocated with respect to the positively charged lattice of nuclei behaves as an induced dipole, and for a perfect conductor, the polarization of this dipole will exactly cancel out the external field. If the external field could be turned off instantaneously, the displacement field would still exist due to the polarization of the metal, and the electrons would experience a force from this field driving them to their "equilibrium" position and then cause them to overshoot. This collection of electrons will oscillate at the metal's characteristic plasma frequency,  $\omega_p$ .

Bulk plasmons are longitudinal charge oscillations (the oscillation direction is colinear with the direction of propagation). Conversely, electromagnetic waves are transverse waves (the

oscillations are perpendicular to the wavevector.) For this reason, it is not possible to excite a bulk plasmon optically since the photon cannot transfer its momentum to the plasmon (at least not at normal incidence).<sup>73</sup> Certain obscure anisotropic metamaterials with negative real permittivity in one direction and positive real permittivity in the other direction enable the optical excitation of bulk plasmons,<sup>74</sup> but these conditions are not relevant to the isotropic substrates in this work.

The plasma frequency in the Drude model is the frequency at which a bulk plasmon may occur, and it also is the approximate transition point in the behaviour of the metal: below  $\omega_p$  typical metallic reflection occurs, and well-above  $\omega_p$  it approaches the behaviour of a vacuum ( $\epsilon = 1 + 0i$ ). Thus it is possible to determine the plasma frequency from reflectivity spectra (section 5.1), even though no plasmon is excited during such a measurement.<sup>73</sup>

Although it is not possible to excite a bulk plasmon optically, when a conductor is made into a film much thinner than the skin depth, there is a plasmon resonance related to the bulk plasmon which may be observed spectroscopically. As discussed above, the bulk plasmon is an oscillation that arises independently of any external field. By the constitutive relation,  $\mathbf{D} = \epsilon\mathbf{E}$ , it can be seen that the displacement field is independent of the external field when  $\epsilon = 0$ . Indeed, this is the result of the Drude model (eqn. 2-10) when the frequency of the external field is equal to the screened bulk plasma (SBP) frequency,  $\omega_{SBP} = \frac{\omega_p}{\sqrt{\epsilon_\infty}}$ . When a Drude conductor is made into a very thin film, opposite charges develop on the surfaces of the film and oscillate at the screened bulk plasma frequency. The charge distribution resembles a parallel plate capacitor and accordingly, this resonance has been occasionally called a capacitive plasmon resonance. If the permittivity of the material in the gap between the plates of the capacitor is close to zero in the frequency range where the plasmon can be excited, this capacitive mode is called an epsilon-near zero (ENZ) plasmon resonance. The surfaces need not be smooth planes; these modes are observed even on highly rough surfaces where it is theorized that particulates behave as separate capacitors.<sup>75</sup> ENZ modes are typically not relevant for smooth layers of Ag and Au since any possible ENZ mode is dwarfed by interband transitions.<sup>76</sup> However, CMOs do not have such transitions, and are “better metals” (as described by the Drude model) for observing ENZ plasmon resonance. ENZ modes can be observed as a dip in the p-polarized reflection spectrum, however, since it is often not experimentally feasible to obtain a reference spectrum in the absence of the conductive film, it is common to report the ratio of p- to s-polarized spectra since the s-polarized

spectrum is relatively featureless. The intensity of the excitation depends upon the angle of incidence to the p-polarized light since the component of the electric field transverse to the film capable of exciting the ENZ mode is highest at grazing incidence and zero at normal incidence. However, in contrast to propagating surface plasmon-polaritons (PSPPs) which will be discussed below, the excitation frequency of an ENZ mode does not depend on the angle of incidence, which can be used as an identifying characteristic. This fact can be appreciated by considering that, because the real permittivity is near zero (changing from positive to negative), the wavevector is also near zero and changing from real to complex since the wavevector is proportional to the square root of the permittivity. ENZ modes and PSPPs cannot both be fully expressed under the same conditions. With extremely thin films, ENZs dominate while PSPPs can be excited for somewhat thicker films where ENZ modes are quenched.

### 2.7.2 Polaritons

Plasmons can only be a relevant explanation of the enhancement in SEIRAS if they are capable of being excited by infrared light. A photon passing into condensed media ( $\epsilon \neq \epsilon_0$ ) can interact with the electrons in the material, and this interaction causes the EM wave to behave differently than it does when it is travelling in free space. For example, an EM wave inside a medium does not travel at the speed of light. One framework to account for the different behaviour is to strictly define a photon as travelling exclusively in free space. A theoretical quasiparticle called a polariton can be constructed for a quantum of electromagnetic field inside a medium which accounts for the superposition of the source fields and the medium response. When the photon enters a medium, it ceases to be a photon, and it becomes a polariton. The properties of a polariton are different from that of a photon travelling in a vacuum, for example the polariton has mass, causing it not to travel at  $c$ , the speed of massless particles.<sup>77</sup> If a polariton can couple with a plasmon, the resulting plasmon-polariton may provide an enhancement mechanism relevant to SEIRAS.

### 2.7.3 Surface Plasmon-Polaritons

Plasmons can couple with polaritons only when the wavevectors of the two quasi-particles match, a condition called momentum matching. The wavevector is a vector quantity where the magnitude is the angular wavenumber,  $|\vec{k}| = 2\pi\tilde{\nu}$  ( $\tilde{\nu}$  is the linear wavenumber inside the medium),

and the direction of the wavevector is the direction of propagation of the wavefronts, which is the same direction as the flow of power for isotropic media. Frequently, a relationship, called the dispersion relation, is constructed to express the wavevector of a wave as a function of frequency. Typically this analysis is limited to only the real part of the wavevector, which is the in-phase component.<sup>78</sup> The wavevector of a wave is a function of its energy (frequency) and the permittivity of the media involved. The dispersion relation of a mode allows the wave vector to be calculated for that mode as a function of frequency. Expressions for the component of the wavevector parallel to both the plane of incidence and the interface (defined as the  $x$ -component here) are provided in equations 2-19 to 2-21.  $\epsilon_{di}$  and  $\epsilon_{met}$  are the permittivities of the dielectric and the metal and  $\theta$  is the angle of incidence. Inspection of equation 2-21 shows that at a characteristic frequency, where the permittivity of the metal equals the negative of the permittivity of the dielectric, the  $x$ -component of the SPP obtains very large values. This characteristic frequency is known as the SPP frequency and for a Drude-modelled metal is given by:  $\omega_{SPP} = \sqrt{\frac{\omega_p^2}{\epsilon_\infty + \epsilon_{di}}}$ . Figure 2-7 plots the wavevectors for various modes as a function of frequency, normalized by the plasma frequency.

$$\text{Photon in infinite 3D media (polariton)} \quad \mathbf{k}_x = \frac{\omega}{c} \sin(\theta) \sqrt{\epsilon} \quad 2-19$$

$$\text{Bulk plasmon} \quad \mathbf{k}_x = \frac{\omega}{c} \sqrt{\epsilon_\infty - \frac{\omega_p^2}{\omega^2}} \quad 2-20$$

$$\text{Surface plasmon-polariton} \quad \mathbf{k}_x = \frac{\omega}{c} \sqrt{\frac{\epsilon_{met} \epsilon_{di}}{\epsilon_{met} + \epsilon_{di}}} \quad 2-21$$

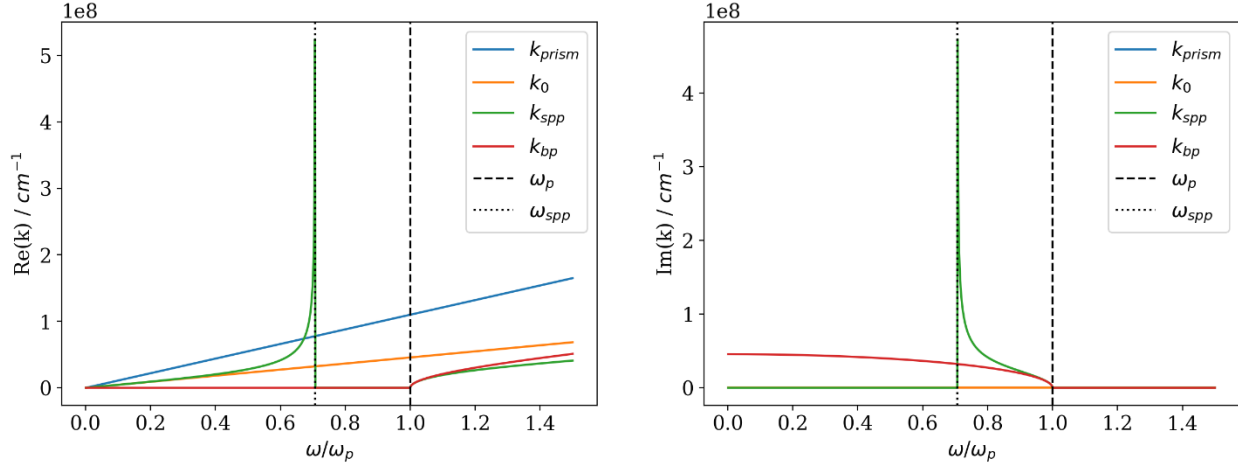


Figure 2-7: Dispersion relations for:  $x$ -component of a polariton in Si prism at 45 degrees AOI (blue); photon in vacuum (orange); Surface plasmon-polariton (SPP) mode at Au-air interface (green); bulk plasmon of Au (red). The real component of wavevector is shown on the left, and the imaginary component on the right. The bulk plasma frequency is marked with a dashed line and the SPP frequency with a dotted line. **Propagating** SPPs may be excited at lower frequencies than  $\omega_{SPP}$  while whereas **localized** SPPs may be excited between  $\omega_{SPP}$  and  $\omega_p$ .

In order to excite a **propagating** surface plasmon polariton, the momentum-matching criterion must be strictly satisfied, that is, the  $x$ -components of the polariton and the surface plasmon polariton must be equal. Propagating surface plasmons occur by the oscillation of charge density across the interface, which implies one further limitation: they can only be excited by  $p$ -polarized light since  $s$ -polarized light does not have an electric field vector component perpendicular to the surface which could drive the oscillation. This is the underlying principle of a technique called Surface Plasmon Resonance (SPR): the angle of incidence is swept until the wave vector component parallel to the interface matches that of the PSPP mode. When the wavevectors match, the polariton couples with the surface plasmon and a large drop in the reflectance is observed as the energy is used to drive the SPP and ultimately dissipated as heat. Since the permittivity of a metal is frequency dependent, there are in fact a range of angles which will satisfy the momentum-matching condition and where SPPs may be excited. Because these conditions arise from the dispersion of the metal, as the angle changes, “plasmons” can be found in different spectral regions. Figure 2-8 plots the frequencies where the momentum-matching condition is satisfied as a function of AOI for the Si/Au interface.

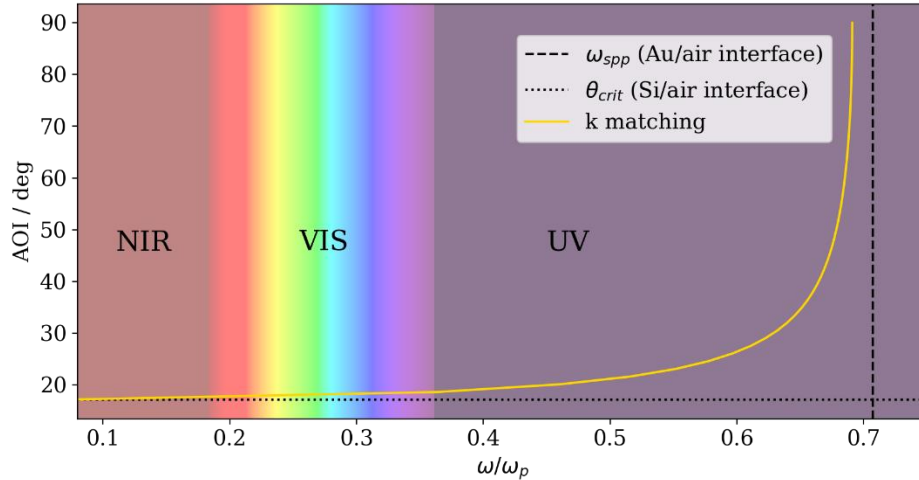


Figure 2-8: The PSPP momentum-matching condition for the Si/Au interface. The blue trace plots the frequency of the intersection points of  $k_{SPP,Au/air}$  and  $k_{x,Si/Air}$  as a function of angle (e.g., the intersection of the green and blue traces in Figure 2-7). This is the frequency of the PSPP resonance as a function of angle. In the NIR, PSPPs are only able to be excited very near to the critical angle.

Localized SPPs are another type of “plasmonic” mode. LSPPs confine the electric field to an interface and could therefore contribute to the surface enhancement effect observed on hybrid CMO-metal ATR-SEIRAS substrates. LSPPs are standing waves of charge oscillation on opposing surfaces of a nanoparticle, and unlike PSPPs, they do not propagate. For this reason, there is no strict momentum matching condition. LSPPs are most commonly discussed in the context of isolated particles and are responsible for the vibrant colours of metal nanoparticle suspensions. Essentially, LSPPs can be considered as a more general case of an ENZ mode. Since ENZ modes are reserved for describing semi-infinite films, they are akin to LSPP modes, which are limited to 1-dimension. Both ENZ and LSPP excitations occur at the transition point where the wavevector goes from real to complex, which is where the real part of conductor’s permittivity function is near zero. Both are independent of AOI, and both involve charge communication across some body of conductive material, which becomes impossible when the dimensions become too large. The main difference is that ENZ modes can only be excited by p-polarized light, while LSPPs can be excited with any polarization because the oscillation can occur in any direction.

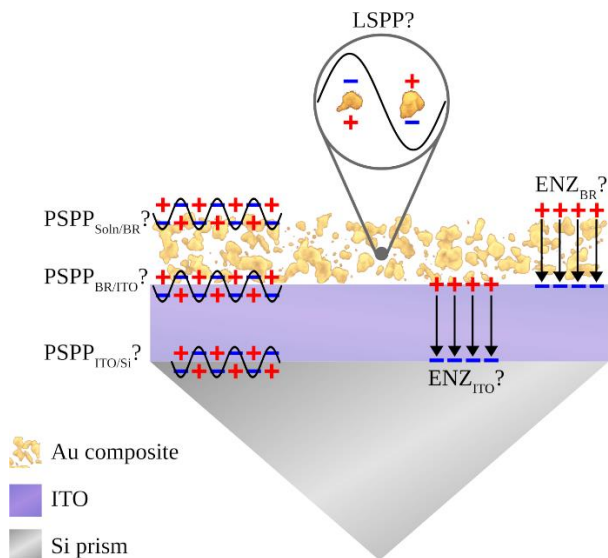


Figure 2-9: Possible operative plasmonic modes in ATR-SEIRAS experiment involving a layered system of Au composite/ITO/Si.

The various plasmon-polariton modes which could plausibly be responsible for the enhancement of a CMO-Au substrate are identified in Figure 2-1. PSPP modes may be supported at the interface between a dielectric and a conductor. The interface between the Si prism and the ITO layer presents one possible location for a PSPP mode. At high fill factors, the Au composite layer is quite metallic, and a PSPP may be supported at its interface with the solution. Additionally, an ENZ mode may be relevant when the film is conductive and thinner than its skin depth. Alternatively, at low fill factors, the Au composite behaves more like a dielectric and perhaps a PSPP could occur between the ITO and the composite layer. Under this scenario, the Au particles should be well-isolated and LSPPs might also be operative. Finally, the conductive ITO layer itself will have an ENZ mode, which may be a relevant enhancement mechanism depending on its plasma frequency. A key aspect of this thesis work is addressing the plausibility of these modes in the ATR-SEIRAS enhancement mechanism. To do so requires the ability to extract the permittivity functions of the CMO and the composite layer. As will be shown, the successful implementation of an effective medium model allows for this analysis.

This concludes the background section. In summary, a material's response to an oscillating electric field depends on a property called the permittivity. Real materials are dispersive, which is to say that the permittivity is a function of applied frequency. One method of calculating the permittivity is the Drude-Lorentz model, which can be applied to both metals and dielectrics,

depending upon the parameters. The transfer matrix method allows observable spectroscopic properties to be calculated from the permittivity of the materials in the system, assuming the system is well-described by a stack of homogeneous thin films. ATR-SEIRAS substrates contain a roughened metal layer, which is a composite of metallic and dielectric particles, and so cannot be directly modelled with the TMM. However, effective medium approximation provides the ability to model the composite layer as an effectively homogenized medium, which is a valid approach since the constituent particles are much smaller than the wavelengths of interest. Thus, a combined EMA/TMM approach will allow for the modelling of ATR-SEIRAS films. This is the approach that will be employed in the following chapters.

### 3 EXPERIMENTAL METHODOLOGY

While the most substantial component of the work undertaken for this thesis was the implementation of the EMA models (section 4), some experimental work was performed to assess the effectiveness of the EMA/TMM approach in describing the behaviour of ATR-SEIRAS substrates.

#### 3.1 Deposition of CMO Thin Films

Conductive metal oxide films were deposited from 2" diameter ceramic targets of two materials: 1) IZO containing 90%  $\text{In}_2\text{O}_3$  and 10% ZnO (Kurt J. Lesker); 2) ITO containing 90%  $\text{In}_2\text{O}_3$  90% and 10%  $\text{SnO}_2$  (Himet Materials). Both target materials are sufficiently conductive to be sputtered using DC power as well as RF. The films were sputtered in a pure Ar plasma by applying a constant 30 W of impedance-matched RF power at 13.56 MHz. Using RF power has been demonstrated to yield more crystalline films, while DC-sputtered films are more amorphous,<sup>79</sup> and high crystallinity is advantageous in terms of conductivity and chemical resistance.

Although sputtering can occur under a static pressure of gas, it is common to pump the chamber at a high rate and continually introduce inert gas while sputtering in order to flush out contaminants and undesirable byproducts which may be produced. These rates are highly dependent on the rate of the pump and the size and arrangement of the chamber and vacuum fittings. For example, when operating under high vacuum (molecular flow regime), doubling the diameter of a vacuum line increases the pump rate by factor of 8.<sup>80</sup> The reader is therefore cautioned that simply matching the parameters reported here may not result in films of the same properties when applied to sputtering equipment having a different vacuum system layout.

The sputtering unit (MagSput-4G2-RF/DC-HOT-UpG, Torr International, Inc.) was custom designed using a variety of commercially available parts. Detailed instructions for

operating this equipment are attached as an appendix. A dual-stage rotary-vane pump (Trivac D8AC) was used to rough out the chamber. A foreline metal wool trap (Kurt J. Lesker TAR4CS100QF) was installed directly on the pump inlet to reduce oil back-streaming. The rotary-vane pump also served as the backing pump and was connected to the exhaust port of the turbomolecular pump (Leybold TurboVac 151) via a ~2 m long KF-25 hose. The turbomolecular pump was installed on the rear wall of the vacuum chamber in a horizontal configuration. The magnetron sputtering guns (Angstrom Sciences, Inc. ONYX-2IC STD) are suspended from the ceiling of the chamber. The chamber (stainless steel cube with 18" edge length) was evacuated to a base pressure of  $2 \times 10^{-5}$  Torr or lower and introduced Ar gas at a flow rate of 2.4 sccm using a mass flow controller (UNIT UFC-1200A). This resulted in an operating chamber pressure of approximately  $2 \times 10^{-3}$  Torr. Sputtering was done at ambient temperature ( $\sim 22$  °C) and the time of deposition was controlled by a quartz crystal monitor (Sigma Instruments FTM-2000 and SQM-160). With a target-substrate distance of 8 cm, the deposition rate was approximately 5 nm/min. The sample stage was rotated at 10 rpm to improve film uniformity. Following deposition, the films were removed from the sputtering chamber and thermally annealed under vacuum in a tube furnace (Lindeberg) at 200 °C for one hour which significantly improved the chemical resilience of the films and increased their conductivity by approximately a factor of four. The thickness of the deposited layers was confirmed by profilometry (KLA-Tencor Alpha step D-120). The sheet resistance was measured with a 4-point probe (Lucas Labs S-302-4) and source measure unit (Keithley 2400 SourceMeter).

### **3.2 Bimodality Parameter and Peak Height**

In order to quantitatively compare the asymmetry of the line shapes, defining a “bimodality parameter” and “peak height” is helpful. There is no clear convention in the literature for this task, so details are provided here on the arbitrarily selected approach utilized in this work. This method will provide a result regardless of significant sloping baselines and is unambiguous for calculated (noise-free) data. First, the local maxima and minima are determined (if any) and the midpoint of the baseline is calculated as the average of two points equally spaced on either side of the resonant frequency. The absolute maximum is the largest of the local maxima and the midpoint, and likewise for the absolute minimum. The upward (downward) going lobe is calculated as the absolute difference between the maximum (minimum) and the midpoint. The peak height is

defined as the sum of the upward and downward-going lobes while the bimodality parameter is calculated as the upward-going lobe divided by the peak height. This results in the bimodality parameter ranging from 0 (fully inverted peak) to 1 (fully upright) with 0.5 representing equally large upward- and downward-going lobes (Figure 3-1).

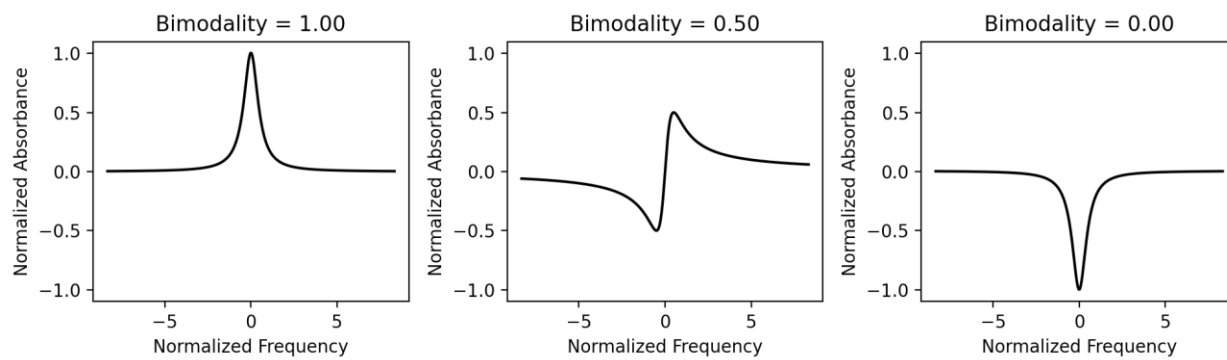


Figure 3-1: Modelled spectral line shapes for bimodality parameters of 1, 0.5 and 0; all plots are normalized to peak heights of unity.

### 3.3 Electrodeposition Spectroscopic Data

To ascertain the range of films that could be produced using electrodeposited Au on CMO, a standardized electrodeposition procedure was developed.  $\text{KAuCl}_4$  (0.12 mM) was pre-mixed with NaF (0.1 M) in a large flask which was used for all of the depositions to ensure the Au concentration remained constant. 4-Methoxypyridine (MOP) was mixed with 25 mL of this electrolyte and purged of dissolved  $\text{O}_2$  by bubbling Ar for 5 minutes. The concentration of MOP was kept at a low concentration (0.1 mM) to provide a spectroscopic handle<sup>81</sup> of the film's enhancement throughout the course of the deposition. Immediately after the 5 minutes had elapsed, the solution was introduced into a spectroelectrochemical cell (Jackfish SEC J1) with a Si micromachined wafer (IRUBIS GmbH) as the internal reflection element (IRE) to deposit the nanoparticle film. The cell was mounted atop a variable-angle optics box (VeeMAX III, PIKE Technologies) in the sample compartment of the spectrometer (Vertex 70V, Bruker). A single deposition cycle consisted of cycling the potential between -1.0 V (this and all subsequent potentials are reported with respect to saturated Ag/AgCl) and +0.05 V for three cycles, beginning and ending at 0 V using a potentiostat (Autolab 302N, Metrohm AG). A reference spectrum was collected while applying -0.90 V for 30 s. The ITO electrode was then biased to +0.30 V and held for 20 s since the adsorption process is slow. The sample spectrum was then collected, and the

electrode was returned to OCP after a total of 50 s. This constitutes one “deposition cycle”. The exception was the very first deposition cycle where the upper potential limit of the cyclic voltammetry was increased to +1.0 V to observe the gold oxidation peak and subsequent catalytic crossover indicating Au is being deposited on Au already in the second cycle.

### **3.4 Cyanate Angle-Dependent Data**

The polarization and angle-dependent data using cyanate were collected by my colleague, Erick Lins. The films were prepared in the above manner using a Si hemisphere as an IRE. The experimental details are provided in a paper that we co-authored.<sup>82</sup>

## 4 IMPLEMENTATION OF AN EMA MODEL

A wide variety of models were researched and implemented, including Yamaguchi,<sup>83</sup> Fedotov,<sup>84</sup> Maxwell-Garnett,<sup>66</sup> core-shell Bruggeman,<sup>85</sup> among others but a detailed discussion of each is outside of the scope of this thesis. Since the primary objective of my project focused primarily on understanding and explaining the observed behaviour of CMO-metal substrates compared to all-metal films, the simpler models were found to be the most useful. I will first discuss some of the considerations involved in selecting an effective medium before describing in detail how the traditional anisotropic Bruggeman model was implemented for an arbitrary number of components. This model is used to explain the behaviour of CMO-metal ATR-SEIRAS films described in the Results and Discussion chapter. The complete algorithm presented here can be readily implemented and the explicit details have not been published in the literature to the author's knowledge.

### 4.1 Selecting an Effective Medium Model

Given the large number of variations of EMAs reported in the literature, it is natural to ask which model should be selected for a particular application. Selecting an EMA model is not as simple as using the most sophisticated EMA. All EMAs are approximations, and they are only rigorously valid in the dilute limit (*i.e.*, as the fill fraction of the inclusions approaches zero). Nevertheless, EMAs have been successfully applied to mixtures significantly outside this limit, and they can sometimes model phenomena beyond their strict range of validity. For instance, Gittleman and Abeles<sup>86</sup> have shown that for isolated metal particles in vacuum, the asymmetric MG model more closely matches the experimental absorption profile of Ag-SiO<sub>2</sub> films than the more advanced Bruggeman model, in particular at higher fill fractions, where the Bruggeman model is generally expected to outperform the simple MG model. It is important to compare the modelled results to experimental spectra of an analogous system to ensure that a suitable model was selected.

Constructing a physically reasonable model of a SEIRAS film using a “classical” EMA is not entirely obvious. In an experiment, the concentration of the analyte has some bulk value in solution in the cell, but it adsorbs to the metal surface concentrating the analyte in the probed region. This is especially true when the metal is biased with a potential that increases the affinity of the analyte to the metal, as is commonly done in an electrochemical SEIRAS experiment. In the basic Bruggeman model (first row in *Table 2-1*), it is possible to either utilize a permittivity function of a dilute analyte in water, or instead consider discrete droplets of water and analyte. In *Figure 5-12* and *Figure 5-13*, the cyanate (analyte molecule) and water are modelled as discrete droplets, although both approaches yield substantially similar results.

An alternate approach is to use the Bruggeman model for a coated ellipsoid to first calculate the permittivity of an isolated, homogenized “effective ellipsoid”. It is then possible to construct an effective medium consisting of two phases (the effective ellipsoid and water), and then model this medium with a second instance of the Bruggeman model to determine the ultimate effective properties (*Figure 4-1*).<sup>85</sup> At first glance, this approach seems to more accurately describe the physical system of an electrochemical SEIRAS experiment since it accounts for the adsorption of the organic molecules in a thin film onto the Au-decorated electrode. However, by design, EMAs are abstractions from the full rigorous consideration of the localized electric fields on a nanoscale, so even if the geometry is more accurately accounted for, this might not be reflected in the resulting effective properties.

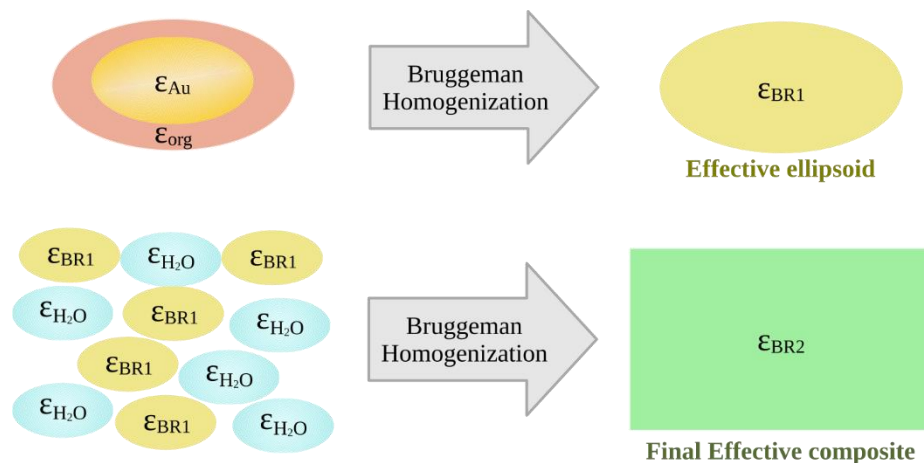


*Figure 4-1: Two-step Bruggeman approach for coated particles. The resulting permittivity of the first instance of the Bruggeman model is used as an input to the second instance.*

The two-step coated ellipsoid approach has one apparent shortcoming: for the conditions examined in this work (25 nm diameter Au core, 1 nm thick Lorentz oscillator shell, immersed in H<sub>2</sub>O) it fails to predict a percolation threshold, since the coated effective ellipsoid is very non-metallic. This limitation has not been discussed in the literature but is an empirical observation of the author and can be justified as follows. A percolation threshold (*i.e.*, a drastic change in the effective permittivity from dielectric-like to metal-like over a small change in fill factor) only occurs for a mixture containing both a metal and a dielectric. Each instance of the Bruggeman calculation is subject to the Wiener limits (section 4.3.4), and the result of the first effective ellipsoid calculation is constrained to a range of values that can ultimately be produced by the second iteration of the model. Coated particles with even extremely thin coatings have permittivities significantly different than their core material. This is to say, the permittivity of the coated particle is essentially non-metallic, and therefore when this permittivity is used in a second iteration of the Bruggeman model to account for the fill fraction of the coated particles in the matrix, no percolation threshold appears since the modelled system is not composed of both metallic and insulating particles. This model, however, has at least one successful prediction that cannot be replicated by the standard isolated particles model. It predicts a change in the line shape as a function of fill fraction of organic particles while keeping the volume of gold fixed. This behaviour has been observed in desorption experiments.<sup>87</sup>

The Bruggeman EMA was selected as the primary model for the analysis of SEIRAS films for the reasons outlined above, namely its relative ease of implementation and understanding, and its ability to qualitatively describe the trends in spectral features observed experimentally. Many different expressions of EMAs are reported in the literature, and it is not immediately obvious how they are related to one another. There are many models which are ascribed the name “Bruggeman”, but which differ significantly from each other. Conversely, there are a wide variety of other names which are in fact identical expressions. The goal of this section is to provide some of the most common expressions and variations and show how they are related, as well as to emphasize any differences and discuss the implications for their validity in describing the systems most relevant to this work.

The Bruggeman model is generally appealing because: 1) it can readily be extended to multiple phases (most other mixing models only allow for two components) 2) it is a reasonably

simple expression which allows for intuitive parameterization of simple geometric models, and 3) it yields fairly accurate results for fill factors at and above the percolation threshold where one would expect the model to fail due omission of near-field particle-particle coupling interactions.

## 4.2 Formulation of Bruggeman model

A few examples are presented in this section to illustrate how a specific expression found in the literature converges to the limiting case in the Bruggeman model. The basic model, as well as the majority of extensions of the model, can be expressed as the following:

$$\sum_j f_j \alpha_j = 0 \quad 4-1$$

where  $f_j$  is the volume fraction of the  $j^{\text{th}}$  phase, with the restriction that  $\sum_j f_j = 1$  and  $\alpha_j$  is the polarizability of a constituent particle of the  $j^{\text{th}}$  phase. This simple formulation rarely appears in the literature, but is provided as equation 14 in a publication by Noh *et al.*<sup>64</sup> where a lucid derivation of the model is presented.

The polarizability of a particle is a function of the permittivity of the constituent material(s) as well as the shape of the particle. Expressions for polarizability are known for a range of different particle geometries. Some of the most useful of these are summarized in *Table 4-1*. The expressions provided are not self-consistent, where self-consistency means that the field “seen” by each particle is modulated by the permittivity of the effective medium rather than the permittivity of the matrix. As identified by Granqvist and Hunderi,<sup>67</sup> the simplest way of achieving self-consistency is to replace the permittivity of the host medium with the permittivity of the effective medium. Therefore, the expressions of the polarizability have  $\epsilon_{matrix}$  replaced by  $\epsilon_{eff}$ . Note that the development of the Bruggeman equation from the generalized effective medium theory (GEMT) equation (see first row, last column in *Table 2-1*) implies the self-consistency condition. In this work, the Bruggeman model always utilizes the self-consistent polarizabilities.

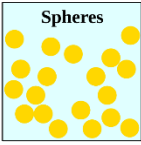
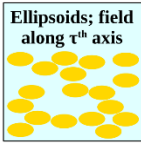
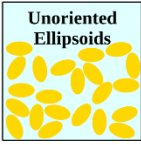
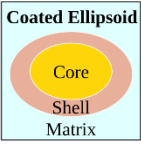
 <p>Spheres</p>	$\alpha = \frac{\epsilon_{particle} - \epsilon_{matrix}}{\epsilon_{matrix} + \frac{1}{3}(\epsilon_{particle} - \epsilon_{matrix})}$
 <p>Ellipsoids; field along <math>\tau^{\text{th}}</math> axis</p>	$\alpha_{\tau} = \frac{\epsilon_{particle} - \epsilon_{matrix}}{\epsilon_{matrix} + L_{\tau}(\epsilon_{particle} - \epsilon_{matrix})}$
 <p>Unoriented Ellipsoids</p>	$\alpha = \frac{1}{3} \sum_{\tau=1}^3 \frac{\epsilon_{particle} - \epsilon_{matrix}}{\epsilon_{matrix} + L_{\tau}(\epsilon_{particle} - \epsilon_{matrix})}$
 <p>Coated Ellipsoid</p> <p>Core Shell Matrix</p>	$\alpha_{\tau} = \frac{(\epsilon_{sh} - \epsilon_{mat})[\epsilon_{sh} + (\epsilon_{core} - \epsilon_{sh})(L_{\tau,core} - FL_{\tau,sh})] + F\epsilon_{sh}(\epsilon_{core} - \epsilon_{sh})}{[\epsilon_{sh} + (\epsilon_{core} - \epsilon_{sh})(L_{\tau,core} - FL_{\tau,sh})][\epsilon_{mat} + L_{\tau,sh}(\epsilon_{sh} - \epsilon_{mat})] + FL_{\tau,sh}\epsilon_{sh}(\epsilon_{core} - \epsilon_{sh})}$

Table 4-1: Polarizabilities for several common particle morphologies.  $L_{\tau}$  is the depolarization factor along the  $\tau^{\text{th}}$  ellipsoidal semi-axis ( $\tau = a, b, c$ ) and  $F$  is fractional volume of coated ellipsoid occupied by the core material. Subscripts:  $sh = \text{shell}$ ;  $mat = \text{matrix}$ .

The term  $L$  appearing in Table 4-1 for the equations for ellipsoids is a geometric factor related to the curvature of the particles along a particular direction.  $L$  is referred to as the depolarization factor. When a polarizable particle is subjected to an external field, the polarization of the material will cause opposite surface charges to develop on opposing sides of the particle. These charges establish an internal electric field called the depolarizing field,  $\mathbf{E}^{(d)}$ , counteracting the applied external field, which is given by the relation  $\mathbf{E}^{(d)} = \frac{L\mathbf{P}}{\epsilon_0}$ , where  $\mathbf{P}$  is the polarization of the particle.

In general,  $L$  is a tensor and can be measured or calculated by finite element methods for any arbitrary shape. For an ellipsoid measured along its basis axes,  $L$  is a diagonalized tensor with three elements,  $L_a, L_b, L_c$ , corresponding to each semi-axis. Small radii of curvature give small  $L_{\tau}$  and the sum of the factors for the three axes of a particle must equal unity. In the limiting case of a needle or a wire, the factor of the pointed end approaches 0, while for a thin sheet or plate the factor of the planar face approaches 1. Formulae to calculate these factors for common ellipsoids are provided in Table 4-2.<sup>88,89</sup>

General form	$a > b > c$	$L_\tau = \frac{abc}{2} \int_0^\infty \left( \frac{1}{(i^2 + q)\sqrt{(q + a^2)(q + b^2)(q + c^2)}} \right) dq$
Prolate spheroids	$a > b = c$	$L_a = \frac{1}{\gamma^2 - 1} \left[ \left( \frac{\gamma}{2\sqrt{\gamma^2 - 1}} \right) \ln \left( \frac{\gamma + \sqrt{\gamma^2 - 1}}{\gamma - \sqrt{\gamma^2 - 1}} \right) - 1 \right]$ $L_b = L_c = \frac{1 - L_a}{2}$
Oblate spheroids	$a = b > c$	$L_a = L_b = \frac{1}{2(\gamma^2 - 1)} \left[ \left( \frac{\gamma^2}{\sqrt{\gamma^2 - 1}} \right) \arcsin \left( \frac{\sqrt{\gamma^2 - 1}}{\gamma} \right) - 1 \right]$ $L_c = 1 - 2L_a$
Spheres	$a = b = c$	$L_\tau = \frac{1}{3}$

Table 4-2: Ellipsoid depolarization factors, where  $\gamma$  is the aspect ratio of major semi-axis to minor semi-axis ( $\gamma \geq 1$ ).  $\tau$  refers to the index of the Cartesian axis; and  $a, b, c$  refer to the radii of the semi-axes from largest to smallest. The integration variable,  $q$ , in the expression for the general form is an ellipsoidal coordinate; details are outside the scope of this work but can be found in Bohren and Huffman.<sup>88</sup>

The complexity of the Bruggeman expression depends on the number of different particle types as well as the complexity of their polarizability functions. The solution to the Bruggeman equation is fairly simple for a two-component mixture of spherical particles but can be very complex for a multi-phase system involving coated ellipsoids. Perhaps the most common expression of Bruggeman found in the literature is the case for a two-component system of spherical particles, such as given in equation 32 in Bruggeman's seminal 1935 paper:<sup>90</sup>

$$f_1 \frac{\epsilon_1 - \epsilon_{BR}}{\epsilon_1 + 2\epsilon_{BR}} + f_2 \frac{\epsilon_2 - \epsilon_{BR}}{\epsilon_2 + 2\epsilon_{BR}} = 0 \quad 4-2$$

In this form, it is clear to see how this equation is a specific case of the more general form of equation 4-1. Equation 4-2 follows from 4-1 with the introduction of two phases of spherical particles. Starting with the polarizability of a spherical particle of bulk permittivity of the first

material,  $\epsilon_1$ , (from Table 4-1), the introduction of the self-consistency criterion (*i.e.*, replacing  $\epsilon_{matrix}$  with  $\epsilon_{BR}$ ) leads to

$$\frac{\epsilon_1 - \epsilon_{BR}}{\epsilon_1 + 2\epsilon_{BR}} = \frac{1}{3}\alpha \quad 4-3$$

As equation 4-3 is valid for the spherical particles of both materials, it is readily apparent that  $f_1\alpha_1 + f_2\alpha_2 = 0$ , gives equation 4-2 for the specific case of a collection of two spherical particles having permittivities  $\epsilon_1$  and  $\epsilon_2$ . Another expression of the Bruggeman model commonly seen in the EMA literature appears in the form of Equation 4-4:<sup>67</sup>

$$\epsilon_{BR} = \epsilon_m \frac{1 - f + \frac{1}{3}Q\alpha}{1 - f - \frac{2}{3}Q\alpha} \quad 4-4$$

This expression is a likewise a reformulation of equation 4-1:

$$\epsilon_{BR} \left(1 - f - \frac{2}{3}f\alpha\right) = \epsilon_m \left(1 - f + \frac{1}{3}f\alpha\right) \quad 4-5$$

$$(1 - f)\epsilon_{BR} - (1 - f)\epsilon_m - \frac{1}{3}f\alpha\epsilon_m - \frac{2}{3}f\alpha\epsilon_{BR} = 0 \quad 4-6$$

$$(1 - f)(\epsilon_{BR} - \epsilon_m) - f\alpha \left(\frac{\epsilon_m + 2\epsilon_{BR}}{3}\right) = 0 \quad 4-7$$

$$f\alpha + (1 - f) \left(\frac{\epsilon_m - \epsilon_{BR}}{\frac{1}{3}(\epsilon_m + 2\epsilon_{BR})}\right) = 0 \quad 4-8$$

$$f\alpha + (1 - f) \left(\frac{\epsilon_m - \epsilon_{BR}}{\epsilon_{BR} + \frac{1}{3}(\epsilon_m - \epsilon_{BR})}\right) = 0 \quad 4-9$$

$$f_1\alpha + f_2\alpha_{sphere} = 0 \quad 4-10$$

Essentially, this expression is for a two-phase system where one of the particles has been designated the “medium” and has been treated as a sphere, while the other may assume any polarizability function. The trivial algebra shown above is to emphasize the point that the myriad

of Bruggeman EMA expressions found in the literature for a diverse set of physics can all be shown to be specific cases of the general expression described in Equation 4-1.

### **4.3 Derivation of an Algorithm for an Arbitrary Number of Ellipsoidal particles**

When expressed in the form of equation 4-4, the Bruggeman permittivity appears straightforward to calculate for spherical particles. However, this representation obscures the nonlinear nature of the model. When a self-consistent polarizability is introduced, the  $\epsilon_{BR}$  term appears on both sides of the equation. When solved, the result is a polynomial in  $\epsilon_{BR}$ , where the degree of the polynomial is equal to the number of phases. The complexity of the mathematical problem increases if the particles are not modelled as isotropic spheres but rather as anisotropic ellipsoids as it means the depolarization term,  $L$ , is no longer a simple scalar ( $L = \frac{1}{3}$  for spheres) but now has different values along each coordinate depending on the radii of the semi-axes of the ellipsoid (*Table 4-2*).

This section describes the development of an algorithm for an arbitrary number of *ellipsoidal* particles, which could be applied to simulating composite films having a range of shapes or sizes. The required steps are:

- 1) Algorithmically determine the coefficients of the binomial factors.
- 2) Calculate the coefficients of each term in the polynomial, for each additive polynomial in the starting expression. Add the coefficients of each additive polynomial to obtain the final coefficients of the polynomial.
- 3) Calculate the roots of the polynomial.
- 4) Determine the physically correct root.
- 5) For anisotropic particles, repeat the calculation for each of the three elements of the diagonalized permittivity tensor:  $\epsilon_{BR,x}, \epsilon_{BR,y}, \epsilon_{BR,z}$ . Convert the permittivity tensor to align with the axes of the applied field.

First, consider the full expression for two types of ellipsoidal particles (the permittivities of which are denoted with subscripts “1” and “2”), using the Bruggeman expression provided in

the first row of *Table 2-1*. It is a sum over each constituent particle type, which itself is a sum over the three Cartesian axes. Written out explicitly this yields:

$$f_1 \frac{\epsilon_{1,x} - \epsilon_{BR,x}}{L_{1,x}\epsilon_{1,x} + (1 - L_{1,x})\epsilon_{BR,x}} + f_2 \frac{\epsilon_{2,x} - \epsilon_{BR,x}}{L_{2,x}\epsilon_{2,x} + (1 - L_{2,x})\epsilon_{BR,x}} = 0 \quad 4-11a$$

$$f_1 \frac{\epsilon_{1,y} - \epsilon_{BR,y}}{L_{1,y}\epsilon_{1,y} + (1 - L_{1,y})\epsilon_{BR,y}} + f_2 \frac{\epsilon_{2,y} - \epsilon_{BR,y}}{L_{2,y}\epsilon_{2,y} + (1 - L_{2,y})\epsilon_{BR,y}} = 0 \quad 4-11b$$

$$f_1 \frac{\epsilon_{1,z} - \epsilon_{BR,z}}{L_{1,z}\epsilon_{1,z} + (1 - L_{1,z})\epsilon_{BR,z}} + f_2 \frac{\epsilon_{2,z} - \epsilon_{BR,z}}{L_{2,z}\epsilon_{2,z} + (1 - L_{2,z})\epsilon_{BR,z}} = 0 \quad 4-11c$$

where  $\epsilon_{BR,\tau}$  is the diagonal tensor element of the Bruggeman-modelled permittivity of the effective medium in the  $\tau^{\text{th}}$  direction. By assuming that the constituent materials have isotropic permittivities (*i.e.*, they are described by a singular complex number at a given particular frequency, independent of direction of the incident radiation), the problem simplifies considerably. Isotropic materials have the same permittivity in all directions, so some of the terms in the above expression are equal:  $\epsilon_{j,x} = \epsilon_{j,y} = \epsilon_{j,z} \equiv \epsilon_\tau$ . Note that anisotropy of the effective medium can still arise due to shape anisotropy of the constituent particles. The following section will deal with calculating the value of  $\epsilon_{BR,x}$  using equation 4-11a; the process is then repeated for the analogous equations for  $\epsilon_{BR,y}$  and  $\epsilon_{BR,z}$ . The sum of quotients may be written as a single quotient:

$$\frac{f_1(\epsilon_1 - \epsilon_{BR,x})[L_{2,x}\epsilon_{2,x} + (1 - L_{2,x})\epsilon_{BR,x}] + f_2(\epsilon_2 - \epsilon_{BR,x})[L_{1,x}\epsilon_{1,x} + (1 - L_{1,x})\epsilon_{BR,x}]}{[L_{1,x}\epsilon_1 + (1 - L_{1,x})\epsilon_{BR,x}][L_{2,x}\epsilon_2 + (1 - L_{2,x})\epsilon_{BR,x}]} = 0 \quad 4-12$$

The denominator approaches zero under two conditions: as  $\epsilon_{BR,x} \rightarrow \left(\frac{L_{1,x}}{L_{1,x}-1}\right)\epsilon_1$  and as  $\epsilon_{BR,x} \rightarrow \left(\frac{L_{2,x}}{L_{2,x}-1}\right)\epsilon_2$ . For spherical particles this simplifies to  $\epsilon_{BR,x} = -0.5\epsilon_1$  and  $\epsilon_{BR,x} = -0.5\epsilon_2$ . These are the conditions where LSPPs may be expressed due to the internal field of the particles diverging.<sup>41</sup> If a singularity is avoided, equation 4-12 can be simplified by multiplying both sides by the denominator:

$$\{f_1(\epsilon_1 - \epsilon_{BR,x})[L_{2,x}\epsilon_2 + (1 - L_{2,x})\epsilon_{BR,x}]\} + \{f_2(\epsilon_2 - \epsilon_{BR,x})[L_{1,x}\epsilon_1 + (1 - L_{1,x})\epsilon_{BR,x}]\} = 0 \quad 4-13$$

To solve for  $\epsilon_{BR,x}$ , notice that each additive term (enclosed in braces) is a product of binomial factors in the form of  $(a_1 + a_2\epsilon_{BR,x})$ , where  $a_1$  and  $a_2$  are constants. For example, the first additive term in equation 4-13 is  $(f_1\epsilon_1 - f_1\epsilon_{BR,x})(L_{2,x}\epsilon_2 + (1 - L_{2,x})\epsilon_{BR,x})$ , which has the form  $(a_1 + a_2\epsilon_{BR,x})(b_1 + b_2\epsilon_{BR,x})$  where  $a_1 = f_1\epsilon_1$ ;  $a_2 = -f_1$ ;  $b_1 = L_{2,x}\epsilon_2$ ;  $b_2 = 1 - L_{2,x}$ . Each additive term can be expanded to generate a polynomial. In this case there are two materials, so there are two additive terms and hence two polynomials (of degree 2) which can be summed together to generate the final polynomial.

Now, consider the more general case where there are  $j$  terms corresponding to the number of constituent materials. Each additional constituent material requires one more binomial factor to be multiplied to all the additive terms (*i.e.*, its denominator is multiplied to each term in the numerator in 4-12). Therefore, the number of binomial factors multiplied together for each term is equal to  $j$ , the number of constituent materials. When the product of binomial factors is fully expanded, each term will generate a polynomial of degree  $j$ . Each polynomial is added to the polynomials of the other additive terms. The roots of the polynomial can then be determined, and the physically correct root selected.

#### 4.3.1 Algorithm for the Product of a Variable Number of Binomial Terms

Consider a product of binomial terms in the form:

$$(a_1 + a_2x)(b_1 + b_2x)(c_1 + c_2x)\dots(m_1 + m_2x)(n_1 + n_2x) = 0 \quad 4-14$$

Expanded fully, this gives a polynomial of degree  $n$ , where  $n$  is the number of binomial terms:

$$C_0x^0 + C_1x^1 + C_2x^2 + \dots + C_mx^m + C_nx^n = 0 \quad 4-15$$

The coefficients are given by:

$$C_0 = a_1b_1c_1 \dots m_1n_1$$

$$C_1 = a_2b_1c_1 \dots m_1n_1 + a_1b_2c_1 \dots m_1n_1 + a_1b_1c_2 \dots m_1n_1 + \dots + a_1b_1c_1 \dots m_2n_1 + a_1b_1c_1 \dots m_1n_2$$

$$C_2 = a_2b_2c_1 \dots m_1n_1 + a_2b_1c_2 \dots m_1n_1 + a_2b_1c_2 \dots m_1n_1 + \dots + a_2b_1c_1 \dots m_2n_1 + a_2b_1c_1 \dots m_2n_2 \\ + a_1b_2c_2 \dots m_1n_1 + a_1b_2c_1 \dots m_1n_1 + \dots + a_1b_2c_1 \dots m_2n_1 + a_1b_2c_1 \dots m_1n_2 \\ + \dots \\ + a_1b_1c_1 \dots m_2n_2$$

...

$$C_n = a_2 b_2 c_2 \dots m_2 n_2$$

The polynomial can be represented in the form of factored binomial terms using two arrays,  $R_1$  and  $R_2$ :

$$R_1 = [a_1, b_1, c_1, \dots, m_1, n_1] \quad 4-16$$

$$R_2 = [a_2, b_2, c_2, \dots, m_2, n_2] \quad 4-17$$

The coefficient of degree zero is simply the product of all the terms of  $R_1$ . To calculate the coefficient of degree one, the first term in  $R_1$  is replaced by the first term in  $R_2$ , then the product of all terms in the resulting array is taken. Next, the second term in  $R_1$  is replaced by the second term in  $R_2$  and all terms of the resulting array are multiplied. Once all terms have been replaced, and the products calculated, the final coefficient is obtained by summing all of the products.

Generally, the coefficient,  $C_i$ , of the  $\epsilon_{BR,x}^i$  term is calculated by first obtaining all the sequences formed by replacing  $i$  terms in  $R_1$  by the corresponding terms in  $R_2$ . The elementwise product of each sequence is then calculated. Finally, the sum of all of these products yields the coefficient.

### 4.3.2 Calculate the Coefficients for Each Additive Polynomial

The preceding section has not addressed how the components of the binomial terms (*e.g.*, the values in  $R_1$  and  $R_2$ ) are determined. Additionally, it only considered how to calculate the coefficients of the polynomial  $f_1$  term in the numerator of equation 4-13. It is important to keep in mind that there are  $N$ -many additive “ $f$  terms” which can each be expanded to yield a polynomial of degree  $N$ . Thus, it is necessary to calculate  $N$ -many of each  $C_i$  coefficient, each which then must be summed together to yield a single  $C_i$  coefficient for each power of  $\epsilon_{BR,x}$ . Introducing another subscript may help to clarify:  $C_{i,j}$ , where the  $i$  index refers to the power of  $\epsilon_{BR,x}$  of which it is the coefficient, and the  $j$  index refers to the “additive term” to which it belongs. Both  $i$  and  $j$  range from 1 to  $N$ , where  $N$  is the number of different particle types.

To determine the values in the arrays  $R_1$  and  $R_2$ , return to equation 4-12. One of the binomial factors originates from the numerator, and the other factors are comprised of the denominators of all the other terms. First, an array can be constructed from the factors from all the denominators and then one term can be replaced by the numerator.

$$R_1 = [L_{1,x}\epsilon_1, L_{2,x}\epsilon_2, L_{1,3}\epsilon_3, \dots, L_{m,x}\epsilon_m, L_{n,x}\epsilon_n] \quad 4-18$$

$$R_2 = [(1 - L_{1,x}), (1 - L_{2,x}), (1 - L_{3,x}), \dots, (1 - L_{m,x}), (1 - L_{n,x})] \quad 4-19$$

When calculating the coefficients for the first additive polynomial, the 1<sup>st</sup> element in  $R_1$  is replaced with  $f_1\epsilon_1$  and the 1<sup>st</sup> element in  $R_2$  is replaced with  $-f_1$ , which are the corresponding terms from the numerator. From these modified arrays,  $R_{1,1}$  and  $R_{2,1}$ , the coefficients  $C_{0,1}$  to  $C_{N,1}$  is calculated using the method described in section 4.3.1. The second suite of coefficients is calculated in the same manner. The process is repeated for all subsequent terms up until the coefficients  $C_{0,0}$  to  $C_{N,N}$  have been calculated by replacing the  $j^{th}$  element in  $R_1$  with  $f_j\epsilon_j$  and replacing the  $j^{th}$  element in  $R_2$  with  $-f_j$ . Finally, sum all the  $C_i$  values to determine the overall coefficients:

$$C_{i,tot} = \sum_{j=1}^N C_{i,j} \quad 4-20$$

### 4.3.3 Calculate the Roots of the Polynomial

Various algorithms exist for calculating the roots of polynomials given the coefficient, descriptions of which are outside the scope of this work. The Python NumPy library utilized in this work calculates the eigenvalues of the companion matrix.<sup>91</sup>

### 4.3.4 Determine the Physically Correct Root

For a polynomial of degree  $N$ , there are  $N$ -many roots which satisfy the equation. However, most of these roots do not describe physically valid permittivities. There are several different approaches to rejecting aphysical solutions. Typically, the first step is to reject all roots having a negative imaginary component of their permittivity as these solutions imply a medium with gain.

The success of the root-selection algorithm can be evaluated by plotting the permittivity values as a function of frequency for a variety of different constituent materials and fill factors. Failure of the root selection algorithm is clearly identified if discontinuities are observed in the resulting permittivity function. One must be careful to restrict the fill factors such that their sum equals one; even a correctly implemented algorithm may generate discontinuities in the permittivity function if the volume fill fractions fail to sum to unity.

Wiener limits <sup>62</sup>  $(\epsilon \in \mathbb{C})$	$\epsilon_{BR} = f_1\epsilon_1 + f_2\epsilon_2 \quad 4-21$ $\epsilon_{BR} = \left( \frac{f_1}{\epsilon_1} + \frac{f_2}{\epsilon_2} \right)^{-1} \quad 4-22$
Hashin-Shtrikman <sup>92</sup>  (isotropic only; $\epsilon \in \mathbb{R}$ )	$\epsilon_{BR} = \epsilon_1 + \frac{f_2}{\frac{1}{\epsilon_2 - \epsilon_1} + \frac{f_1}{3\epsilon_1}} \quad 4-23$ $\epsilon_{BR} = \epsilon_2 + \frac{f_1}{\frac{1}{\epsilon_1 - \epsilon_2} + \frac{f_2}{3\epsilon_2}} \quad 4-24$
Bergman-Milton <sup>93</sup>  $(\epsilon \in \mathbb{C})$	$\epsilon_{BR} = f_1\epsilon_1 + f_2\epsilon_2 - \frac{f_1f_2(\epsilon_2 - \epsilon_1)^2}{3[\gamma\epsilon_1 + (1-\gamma)\epsilon_2]}; \frac{(1-f_1)}{3} \leq \gamma \leq 1 - \frac{f_1}{3}; \gamma \in \mathbb{R} \quad 4-25$ $\epsilon_{BR} = \left( \frac{f_1}{\epsilon_1} + \frac{f_2}{\epsilon_2} - \frac{2f_1f_2(\epsilon_2 - \epsilon_1)^2}{3\epsilon_1\epsilon_2[\gamma\epsilon_2 + (1-\gamma)\epsilon_1]} \right)^{-1}; \frac{2(1-f_1)}{3} \leq \gamma \leq 1 - \frac{2f_1}{3}; \gamma \in \mathbb{R} \quad 4-26$

Table 4-3: Bounds on physical validity of  $\epsilon_{BR}$ .

Several different bounds from the literature are reported in Table 4-3. The Wiener bounds were utilized in this work for simplicity. A situation where the root selection failed was not encountered for three-phase composites, but occasionally the root selection for four phases was ambiguous, in which case the root must be selected manually to generate a continuous function. The Hashin-Shtrikman bounds provide improved (narrower) limits but are limited to strictly real-valued permittivities. The Bergman-Milton bounds extend the Hashin-Shtrikman bounds to complex permittivities and should be preferred to the Wiener bounds if the Wiener bounds fail to unambiguously determine the valid root.

The Wiener bounds describe a circle and chord on the complex plane which enclose a circular segment where physically plausible roots may be found. For a two-phase composite, the valid root must lie inside this region defined by the permittivities of the two constituent materials,  $\epsilon_1$  and  $\epsilon_2$ , using the equations in Table 4-3. For composites containing additional phases, the overall region of validity is the intersection of the circular segments defined by every combination of each pair of component permittivities, yielding  $\binom{N}{2} = \frac{N!}{2!(N-2)!}$  segments. Additionally, the valid root may lie inside any triangle formed by every combination of each trio of component permittivities for a total of  $\binom{N}{3}$  triangles. For metal-insulator composites where the permittivities

are very dissimilar, the roots will frequently lie very close to the region of validity, and due to floating point errors, the valid root may in fact lie outside the region. Conversely an invalid root may lie within the region due to floating point errors. A signed distance function was implemented in my program to determine the “best” root in the cases where either no or multiple roots are within the region of validity because of floating point errors.

#### 4.3.5 Calculate $\epsilon_{BR,x}$ , $\epsilon_{BR,y}$ , $\epsilon_{BR,z}$

For the calculation of anisotropic particles, the above steps are repeated in each of the coordinate directions to obtain each of  $\epsilon_{BR,x}$ ,  $\epsilon_{BR,y}$ ,  $\epsilon_{BR,z}$ . If the ellipsoids are randomly oriented about a particular axis, one can take the arithmetic mean of the permittivities orthogonal to the axis of rotation. If the ellipsoids are oriented and an ellipsoidal semi-axis is aligned with the applied field. However, if the ellipsoids are oriented off-axis with respect to the applied field, the permittivity tensor for the coordinate system of the applied field can be calculated by:  $\epsilon' = R^{-1}\epsilon R$  where  $\epsilon$  is the permittivity tensor in the local coordinate system of the ellipsoid,  $\epsilon'$  is the permittivity tensor in the coordinate system of the applied field and  $R$  is the rotation matrix to transform the basis vectors of the ellipsoid into the basis vectors of the applied field<sup>94</sup> (Figure 4-2). The rotation matrix may be parameterized in many different ways, two methods implemented in my program are: 1) three angles representing the clockwise angle of rotation about the local axes (yaw, pitch and roll) and 2) a vector and a single angle using the method described by Rodrigues.<sup>95</sup>

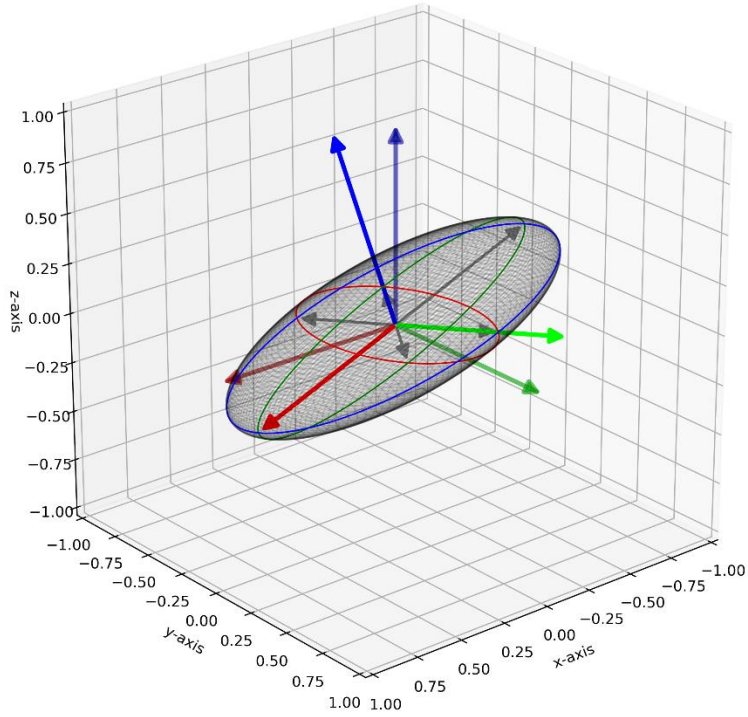


*Figure 4-2: Program output visualizing an ellipsoid oriented off-axis with respect to the applied field; rotated  $20^\circ$  counterclockwise about the  $[111]$  axis. The rotation matrix is the matrix which will transform the local basis vectors of the ellipsoid (saturated RGB vectors) into the desired coordinate system of the applied field (dull RGB vectors).*

## 5 RESULTS AND DISCUSSION

First, the parameters of the CMO films in terms of the Drude model will be described and the questions raised by Figure 2-9 of the potentially existing plasmonic modes will be addressed. The observed behaviour of CMO-metal ATR-SEIRAS substrates will be compared to all-metal films and an account of the asymmetric lineshapes will be provided in terms of the Bruggeman-modelled material parameters.

### 5.1 CMO Modelling

To model ATR-SEIRAS substrates using the transfer matrix method, it is necessary to define the permittivity of all of the layers. Furthermore, to adjudicate whether any of the plasmonic effects depicted in Figure 2-9 are responsible for the observed surface enhancement, the plasma frequency of the CMO layer must be determined. To this end, reflectivity spectra were measured at a range of angles and for ITO and IZO layers of different thicknesses. Using the Drude model and the transfer matrix method (TMM), calculated spectra were fit to the experimental spectra and the material properties (plasma frequency and damping factor) can be extracted. These parameters were used to calculate the permittivity of the CMO for the model. Both ITO and IZO behaved similarly. The standard thermal annealing procedure (1 hour at 300 °C) yielded films which could not be fitted to the Drude model since the plasma frequency was in the NIR, outside the spectral range of the FTIR spectrometer. A reduced annealing procedure of 10 nm at 150 °C enabled measurements to be made. Two limits were identified as the reasonable bounds of films which could be likely produced: metal-like CMO with  $\omega_p = 25000 \text{ cm}^{-1}$ ,  $\Gamma = 400 \text{ cm}^{-1}$ ,  $\epsilon_\infty = 4.5$  and dielectric-like CMO with  $\omega_p = 8000 \text{ cm}^{-1}$ ,  $\Gamma = 2500 \text{ cm}^{-1}$ ,  $\epsilon_\infty = 4.5$ . These parameters were utilized in the calculations for Figure 5-8. Note that experimental films having these exact parameters were not produced, but these parameters represent reasonable limiting cases of the most insulating and most conductive films that could possibly be produced by varying the sputtering and annealing parameters of the CMO deposition.

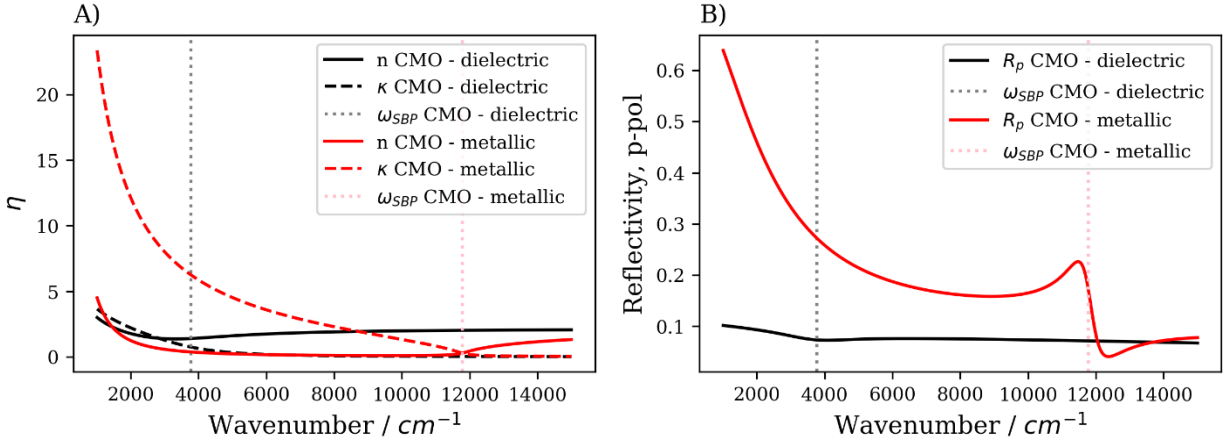


Figure 5-1: A) Real ( $n$ ) and imaginary ( $\kappa$ ) refractive index of a CMO calculated by Drude model (parameters extracted from external reflection spectra); B)  $p$ -polarized external reflectivity spectrum calculated for air/25 nm of CMO/Si.

There is a dip in the  $p$ -polarized external reflectivity spectrum which occurs at the screened bulk-plasma frequency,  $\omega_{SBP} \approx \sqrt{\frac{\omega_p^2}{\epsilon_\infty}}$ . This is best described as an epsilon-near zero mode<sup>96</sup> which occurs in the vicinity of  $Re(\epsilon) = 0$ ; *i.e.*, the crossing point of  $n$  and  $\kappa$  (Figure 5-1).

## 5.2 Plasmons

The underlying mechanism that gives rise to the ATR-SEIRAS effect remains a poorly understood concept. Various interpretations in the literature (and within the Burgess group) invoke “plasmonic” factors. Prior to the work of this thesis, the group did not have the necessary tools to attempt a systematic evaluation of the relevancy of various surface plasmon polariton (SPP) mechanisms. Evaluating possible SPP contributions requires knowledge of the permittivity function of all the layers in the ATR-SEIRAS substrate. The successful implementation of the Drude model for the ITO layer and Bruggeman EMA for the Au-composite layer now enables such an evaluation.

As indicated in Figure 2-9, several interfaces of the ATR-SEIRAS substrates investigated in this thesis work present possible scenarios where various SPP modes might manifest. In addition to laterally *propagating* SPP modes, thin conductive films also allow ENZ modes where charge oscillates from one side of the film to the other. Finally, the electrodeposited Au films may behave as isolated nanoparticles at low fill-factors, enabling the possibility of *localized* SPPs. If

SPPs (propagating, localized or ENZ modes) are excited under the conditions of an ATR-SEIRAS experiment, they may be at least partly responsible for the surface enhancement effect. Identifying any relevant SPPs would inform efforts to adjust the optical properties of the films and experimental conditions (AOI, polarization) to maximize the enhancement.

### 5.2.1 Propagating Surface Plasmon Polariton (PSPP) Modes

In general, satisfying the momentum matching condition for exciting a *propagating* SPP requires an incident EM wave to be propagating in a high refractive index medium, impinging on a conductor/dielectric interface. Osawa *et al.*<sup>42</sup> concluded that *propagating* SPPs are unlikely to be responsible for the enhancement observed on traditional all-metal SEIRAS substrates for two main reasons. Firstly, the enhancement seen from the evaporated Au metal island films is observed at all angles but is highest at grazing angles of incidence. Conversely, PSPP modes are only operative under momentum matching conditions, which occur under a very narrow range of angles, very near the critical angle (eqn. 2-1). For typical ATR crystal materials, the critical angle occurs much closer to normal incidence than the angles where the highest enhancement is observed on pure Au substrates. Secondly, PSPPs are only excited by p-polarized light, while SEIRA spectra can be observed for both s- and p-polarized light (albeit higher enhancement is generally observed for p-polarized light).

Unlike conventional all-metal substrates supported directly on the ATR crystal, substrates with a CMO underlayer show their maximum enhancement at angles just above the critical angle, as would be expected if PSPPs were the dominant contributor to enhancement (to be discussed in section 5.3.3). To evaluate whether a PSPP may be supported at an interface, recall that the momentum matching condition requires that the two materials forming the interface have opposite permittivities, *i.e.*, the interface must be between a conductor and a dielectric. Three interfaces which could conceivably have opposite-signed permittivities were identified in Figure 2-9 as potential locations where PSPPs may be supported, namely: 1) Si prism/CMO, 2) Au composite/solution, and 3) CMO/Au composite.

#### 5.2.1.1 Si prism/CMO interface

First, consider the Si prism/CMO interface. It is not possible to excite a *purely propagating* SPP at a metal/dielectric interface by going through the dielectric material, no matter how high the

index of the dielectric. As  $\omega \rightarrow 0$ , the permittivity of an undamped Drude-modelled conductor approaches  $-\infty$  and therefore  $k_{x,PSPP} \rightarrow \frac{\omega}{c} \sqrt{\epsilon_{dielectric}}$  according to equation 2-21. The wavevector of the PSPP at any frequency between 0 and  $\omega_{SPP}$  will be higher than the wavevector passing through the dielectric, even at grazing incidence. Thus, to attain momentum matching conditions, the excitation photon must pass through a material having a higher permittivity than the dielectric involved with the PSPP. For this reason, a *purely propagating* SPP can be ruled out at the Si/CMO interface, since the excitation photon is passing through the same dielectric (Si prism) as the dielectric at the interface in question. However, for highly damped “conductors” (poor conductors), there may be the possibility of exciting damped SPPs, since the imaginary part of the conductor’s permittivity broadens the resonance. The wavevector of the surface mode becomes complex, which indicates a damped mode.

The wavevector for the Si/metal-like CMO interface (calculated by the dispersion relation given by eqn. 2-21) only matches the wavevector through the Si prism at frequencies above  $\nu_{SPP}$  (Figure 5-2A), that is, frequencies which are, by definition, not PSPPs. This is evident by observing the significant imaginary component of the wavevector, which indicates that the surface wave is decaying exponentially. Furthermore, these frequencies lie significantly outside the upper bound of the mid-IR region of the EM spectrum. For the dielectric-like CMO, the damping factor has broadened the resonance considerably and the overall magnitude of the wavevector is quite low. Momentum matching conditions are achieved at mid-IR wavelengths and at commonly accessible angles, but again these are not purely propagating SPPs, and the surface wave is highly damped because  $Im(k_{PSPP})$  is quite large. It is possible that this *quasi*-PSPP may contribute to the surface enhancement, however the effect is likely small since it is highly damped. Furthermore, the parameters of the dielectric-like CMO are the upper bound of what may be realistically achievable for the damping factor of a CMO, and the typical ITO films used in this work were considerably more conductive.

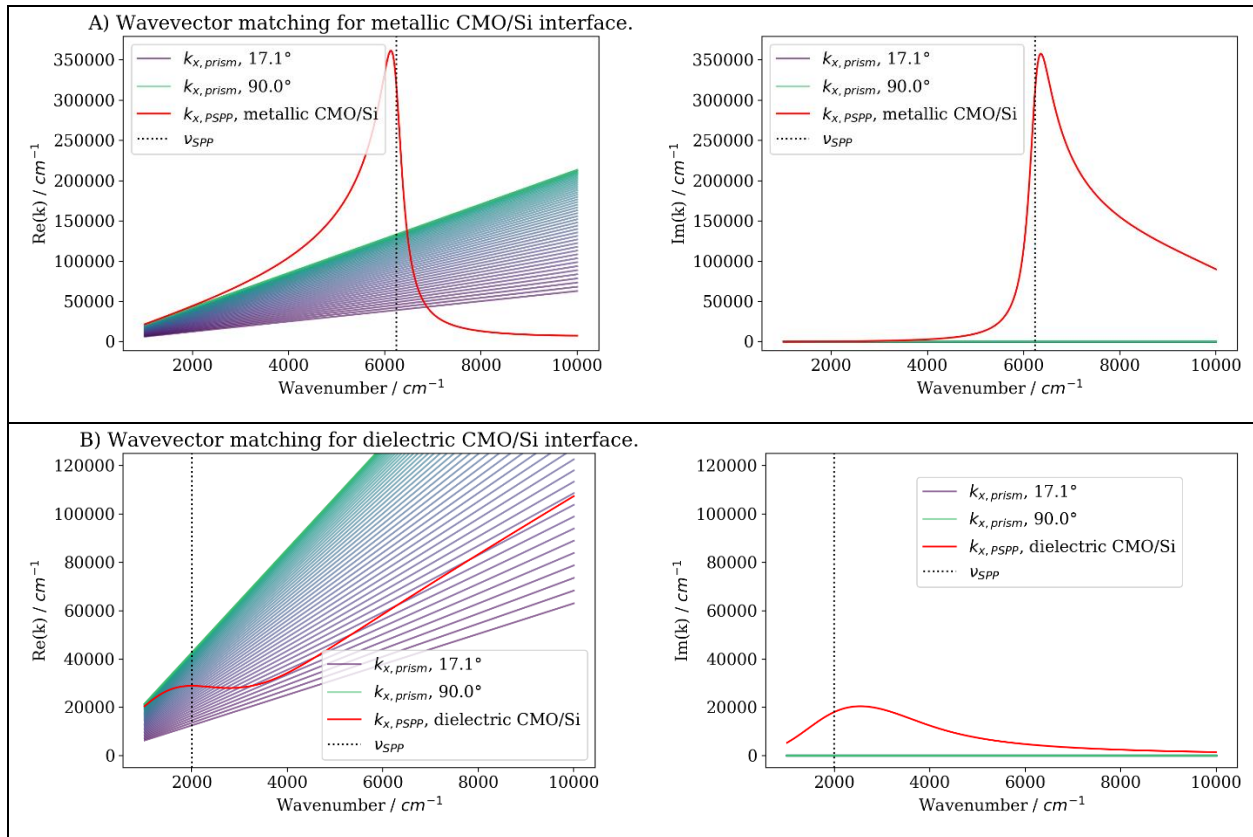


Figure 5-2: In-plane wavevector components of PSPP at the interface between the Si prism and CMO interface for: A) metal-like CMO and B) dielectric-like CMO. The intersection between the PSPP wavevector (red) and the wavevector of the excitation polariton in the Si prism (indigo to teal at AOIs from  $17.1^\circ$  to  $90.0^\circ$ ) indicates the conditions (frequency, angle and wavevector) where a PSPP may be excited.

### 5.2.1.2 CMO/Au composite interface

Thoroughly investigating and concisely reporting all the possible PSPP modes which may exist at the CMO/Au-composite interface is challenging due to the large range of optical properties available by combinations of CMO and Au-composite layers.

Table 5-1 presents the results of analyzing the wavevector matching conditions for the four broad categories of CMO/Au composite interfaces. The main conclusion from this table is that for any combination of materials investigated, there was never any set of conditions which resulted in a minimally damped PSPP occurring in the mid-IR at moderate AOIs relevant to an ATR-SEIRAS experiment.

Au fill factor \ CMO type	Low $f_{Au}$	High $f_{Au}$
Dielectric-like CMO	Minimally damped PSPPs in mid-IR occurring only very near the $\theta_{crit}$ .	Highly damped PSPPs in mid-IR occurring at moderate AOIs.
Metal-like CMO	Minimally damped PSPPs blue shifted out of mid-IR.	Permittivity of both materials has the same sign; no PSPPs.

Table 5-1: Summary of investigation of momentum matching analysis for CMO/Au composite interface.

### 5.2.1.3 Au composite/solution interface

As for the Au composite/H<sub>2</sub>O interface, wavevector matching occurs only very near the critical angle. At higher metal volume fractions, the matching angle increases, however the frequency is blue shifted out of the mid-IR and is therefore not relevant to ATR-SEIRAS enhancement (Figure 5-3).

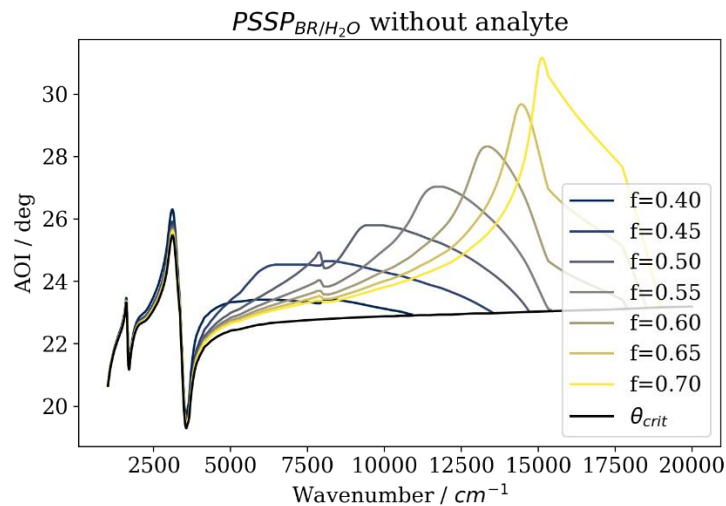


Figure 5-3: Wavevector matching condition for the Bruggeman-modelled Au-composite/H<sub>2</sub>O interface. The frequency and AOI of each intersection between  $k_x$  (PSPP Bruggeman/H<sub>2</sub>O) and  $k_x$  (Si) is plotted to identify possible PSPPs.

### 5.2.2 Epsilon Near Zero (ENZ) Modes

It is clear from the experimental external reflectivity spectra (Figure 5-4) of the CMO films that there is a decrease in reflectivity which occurs at the screened bulk plasma frequency. This

peak is only observed in the p-polarized spectrum and the position is angle-independent, which is indicative of an ENZ mode (Figure 5-4).

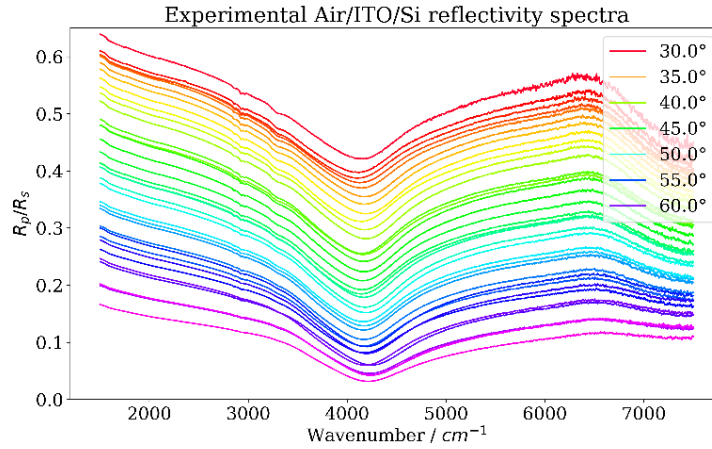


Figure 5-4: Experimental external reflectivity spectra of an as-deposited (unannealed) 50 nm ITO film demonstrating the excitation of an ENZ mode at  $\sim 4200 \text{ cm}^{-1}$ .

Rhodes *et al.*<sup>49</sup> have demonstrated that either ENZ modes or PSPPs can be excited for the glass/ITO/air system, and the thickness of the ITO film determines which phenomenon will be expressed. Analogous calculations were performed using a high index Si prism instead of glass and H<sub>2</sub>O as the backing layer to identify ENZ and PSPP modes in the ITO films used in this work. Figure 5-5 shows the modelled reflectivity for light internally reflected from the interface of water and two different thicknesses of an ITO film supported on Si. ENZ modes are only supported on ITO layers thin enough to support charge localization perpendicular to the surface. In contrast, the PSPP oscillation of unbound electrons is parallel to the surface. At the conductor–insulator surface, a PSPP mode results in an evanescent wave which extends into both sides of the interface. The evanescent wave cannot be supported if the thickness of the CMO is smaller than the skin depth of the material. Thus, below  $\sim 50 \text{ nm}$ , the ITO layer only supports ENZ modes, whereas above  $\sim 100 \text{ nm}$  only PSPP modes are observed. Figure 5-5A shows the ENZ mode as a pronounced dip in the ratio of  $R_p$  to  $R_s$  that occurs at the frequency where the real and imaginary parts of the refractive index of ITO converge. Figure 5-5B shows the PSPP that develops for thicker ITO layers. Unlike the ENZ mode, the frequency of the PSPP mode is highly dependent on AOI. The PSSP is most pronounced at angles close to the critical angle and its amplitude rapidly diminishes

with increasing angle of incidence. These calculations allow an assessment of the relevancy of ENZ and PSPP modes to experimental ATR-SEIRAS.

As the PSPP mode is not observed in modelling calculations until the film is several times thicker than the CMO layers used in these experiments, it is highly unlikely to be active in our SEIRAS experiments. On the other hand, the ENZ mode is likely operative but for the typical ITO films produced and modelled in this work, the resonance occurs only at near-IR frequencies ( $\sim 8000 \text{ cm}^{-1}$ ). However, since the plasma frequency of CMOs can be tuned by modifying the deposition and annealing conditions, this presents an interesting possible research project to engineer the ITO optical parameters such that ENZ modes are supported in the mid-IR.

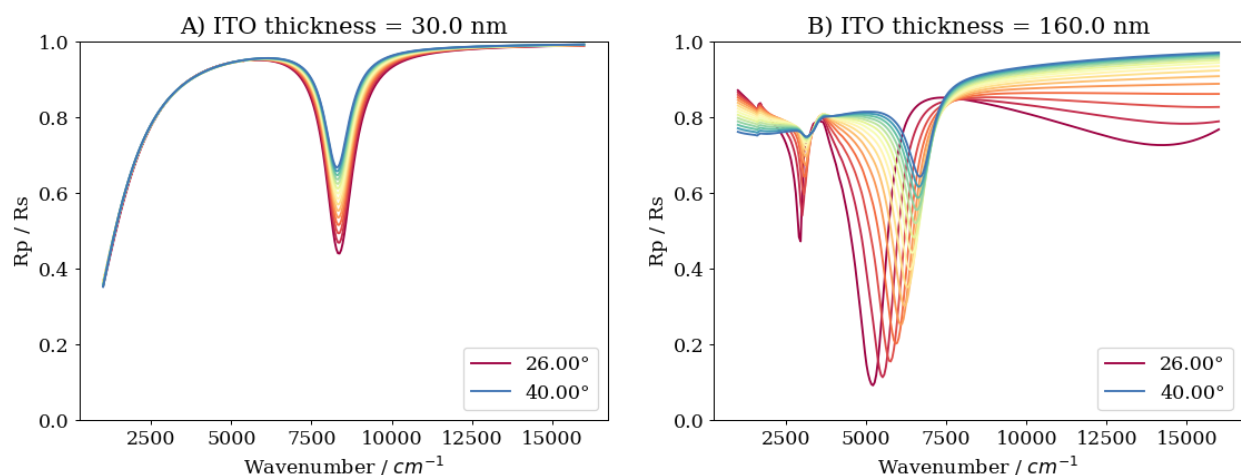


Figure 5-5: Ratio of  $p$ - to  $s$ -polarized modelled reflectivity spectra for the Si/ITO/ $\text{H}_2\text{O}$  system. The 30 nm film (A) demonstrates an ENZ mode, while the 160 nm film (B) demonstrates a PSPP whose frequency is angle dependent. The feature beyond  $14000 \text{ cm}^{-1}$  is a nonresonant phenomenon resulting from the ITO acting as an interference antireflection coating.<sup>49</sup>

### 5.2.3 Localized Surface Plasmon Polariton (LSPP) Modes

It is difficult to make any definitive statements regarding the presence or absence of LSPPs, as these resonances are polarization and angle-independent and given the metal particle size and shape inhomogeneity, the response is likely to be quite broadband. The electrodeposition procedure yields nanoparticle films where the particles are in the correct size regime for LSPPs to be relevant. At low fill factors, the particles are reasonably well isolated, but as the metal content is increased, it appears from the SEMs (Figure 5-9) that the particles contact each other. The gaps between particles, particularly for high aspect ratio particles, have long been known to provide

extremely high field strengths such as are seen in SERS, but the EMA approach cannot provide any insight into these near-field effects. It is plausible that excitation of LSPPs contribute to the surface enhancement, however some finite-element method would be required to conclusively determine whether that is the case.

In conclusion, as it stands for a typical ATR-SEIRAS experiment the PSPPs and ENZ modes raised as possibilities in Figure 2-9 are either absent or of minimal contribution to the enhancement observed in a typical ATR-SEIRAS experiment involving frequencies in the range of 400 to 3000  $\text{cm}^{-1}$  and at AOIs of 40 to 70°. The relevant range of angles for ENZ and PSPP excitations is rather close to the critical angle, which is not easily experimentally accessible using our off-the-shelf variable incidence angle optics accessory. Similar to pure Au substrates, the ITO-Au substrates also show significant signals with s-polarized light. For these reasons, ENZ and PSPP resonances are unlikely to be responsible for the enhancement effect under the conditions of a standard experiment. No definitive statements about the relevance of LSPPs can be made without finite-element analysis, however there is evidence of significant imaginary wavevector components at certain interfaces which is a precondition for LSPPs.

Identifying and understanding plasmonic phenomena in thin films used for ATR-SEIRAS is of considerable interest to gaining a deeper comprehension of the SEIRAS enhancement mechanism. Both PSPP and ENZ modes have been shown to be unlikely contributors based on our current experimental conditions. However, modelling the permittivity functions (using the Drude-Lorentz and EMA models described in this thesis) opens the possibility of customizing the optical properties and experimental parameters to match calculated SPP conditions. Such an approach could lead to significant improvement in ATR-SEIRAS enhancement factors and detection limits.

However, it is also vitally important to recognize that part of the utility of the EMA/TMM approach is that it abstracts from these details and provides the optical response without any allusion to plasmonic enhancement mechanism. In other words, the EMA/TMM approach can be used to model SEIRAS activity regardless of whether plasmonic modes are active. Instead, EMA/TMM reduces the problem to a far-field assessment of changes in the interfacial reflectivity manifested by the presence or absence of an adsorbed layer. Accordingly, the following sections will not make any further determinations as to the physical origin of the observed enhancement

but rather the performance of CMO-Au substrates will be analyzed by comparing experimental results to EMA/TMM modelling results.

### 5.3 Evaluating SEIRAS response

To evaluate the performance of the EMA model in describing the surface enhancement as a function of deposition, four depositions were performed using different underlayers: ITO and IZO, each in the “as deposited” and “annealed” states. Au was electrodeposited in the presence of 0.1 mM of 4-methoxypyridine (MOP), which is the test analyte used to measure the IR response, selected for its strong IR bands and highly reversible desorption on Au surfaces. Typically, when performing a deposition to obtain an ATR-SEIRAS substrate for a further experiment, the Au deposition process is halted after attaining an absorbance signal of approximately  $10\text{-}15 \times 10^{-3}$  of the  $1309\text{ cm}^{-1}$  band of MOP in order maximize the signal while avoiding distorted bands. To investigate a more complete range, the depositions presented in this section were continued well beyond this point, until the signal became difficult to reliably measure above the noise.

Absorbance spectra were collected during the course of the Au electrodeposition to obtain the response of the films at a range of metallic Au content, which can be compared to modelled spectra at different fill fractions. Three characteristic parameters of the absorbance spectra were calculated, and are plotted as a function of the extent of Au deposition: peak-to-peak absorbance (Figure 5-6), bimodality parameter (Figure 5-7) and integrated detector signal, which is a proxy for the overall reflectivity of the substrate (Figure 5-8). The subplots labelled A) are experimental data, while the B) subplots are modelled data using the EMA/TMM approach for an analogous system, namely: Si / 25 nm of ITO / 25 nm of Bruggeman-modelled composite / H<sub>2</sub>O.

The first significant observation is that over the course of the deposition, the IR enhancement increases until it reaches a maximum, and then the decreases as further Au is deposited. This general trend is predicted by EMA calculations, but there are two maxima rather than one (Figure 5-6). Both experiment and model demonstrate that the overall level of enhancement is higher for unannealed (dielectric-like) CMO.

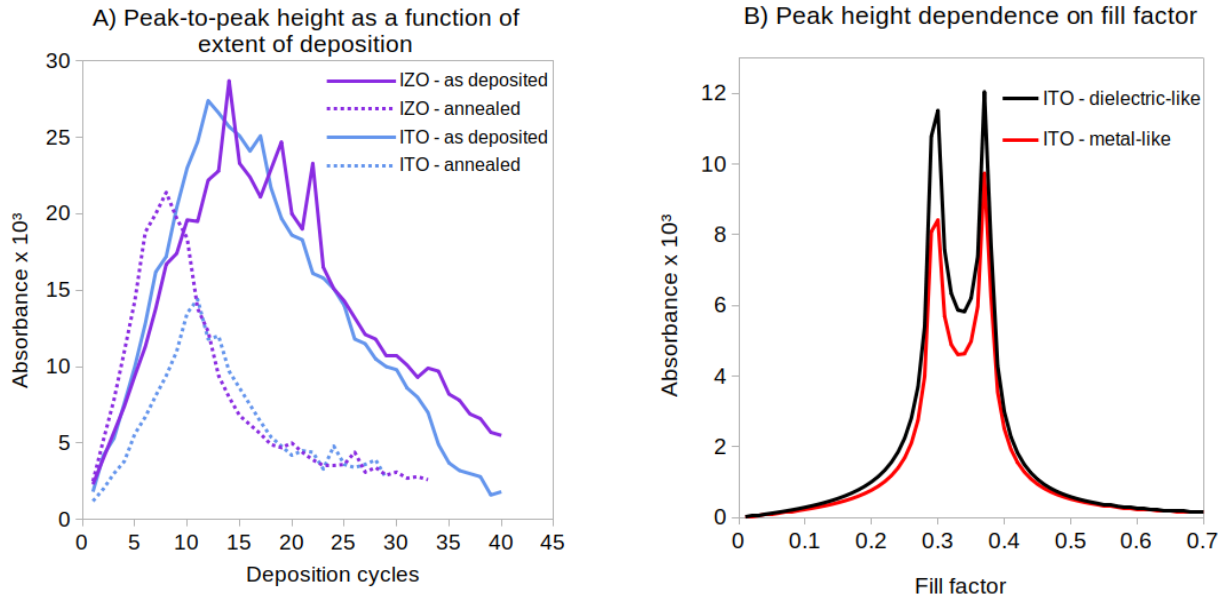


Figure 5-6: Absorbance peak height as a function of the extent of Au deposition for different CMO underlayers.

The general trend of the bimodality parameter of the EMA model matches the experiment somewhat, where the peaks are initially largely upright and the peak asymmetry increases, becoming somewhat inverted (bimodality parameter  $< 0.5$ ) before a partial recovery. The correspondence between experiment and model is not altogether satisfying, partly because the S/N of the experimental data after many Au deposition cycles is quite low. The annealed (conductive) CMO films become more inverted than the unannealed films, however the effect predicted by calculations is much less significant than that observed experimentally.

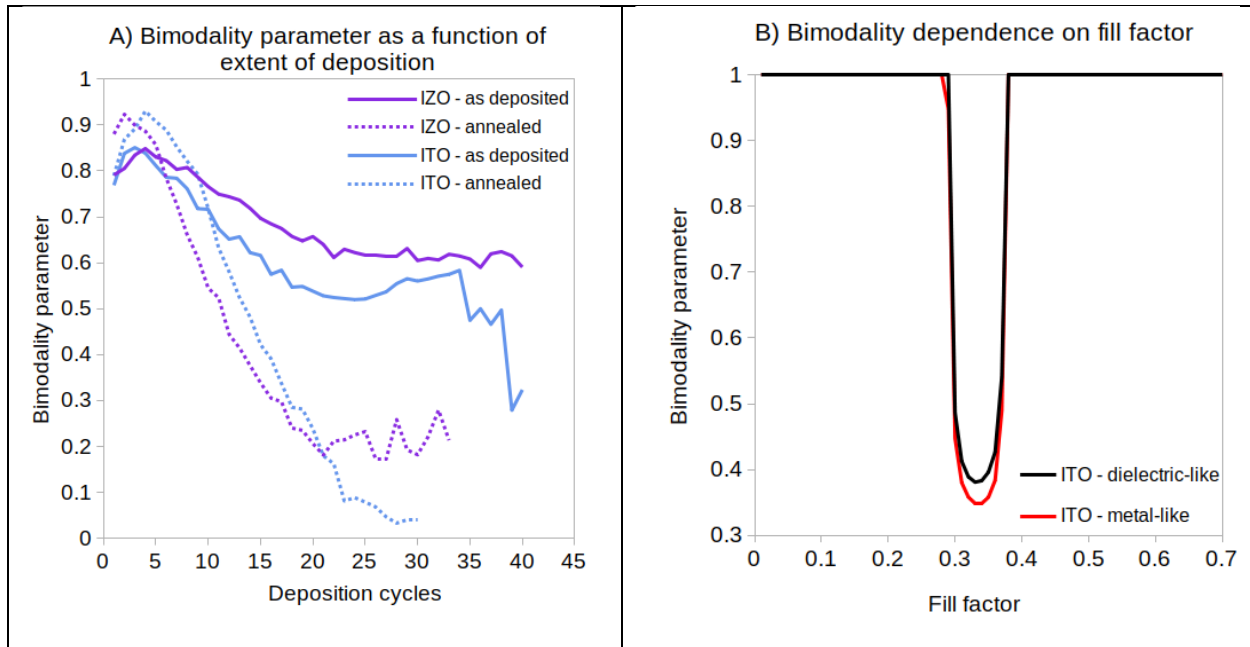


Figure 5-7: Calculated bimodality parameter (as defined in section 3.2) as a function of extent of Au deposition for different CMO underlayers. A) shows experimentally derived data, and B) shows the analogous Bruggeman-modelled data.

The detector counts provide a measure of the reflectivity of the overall system as the deposition progresses. During the initial stage, the reflectivity drops rapidly, then reaches a local minimum. For annealed CMO, the reflectivity increases again as the layer becomes a metallic reflector. This increase in reflectivity is not observed in the experimental data for unannealed CMO, but it is likely that eventually the reflectivity would increase if the deposition had proceeded further by nature of increasing the density and thickness of the Au layer.

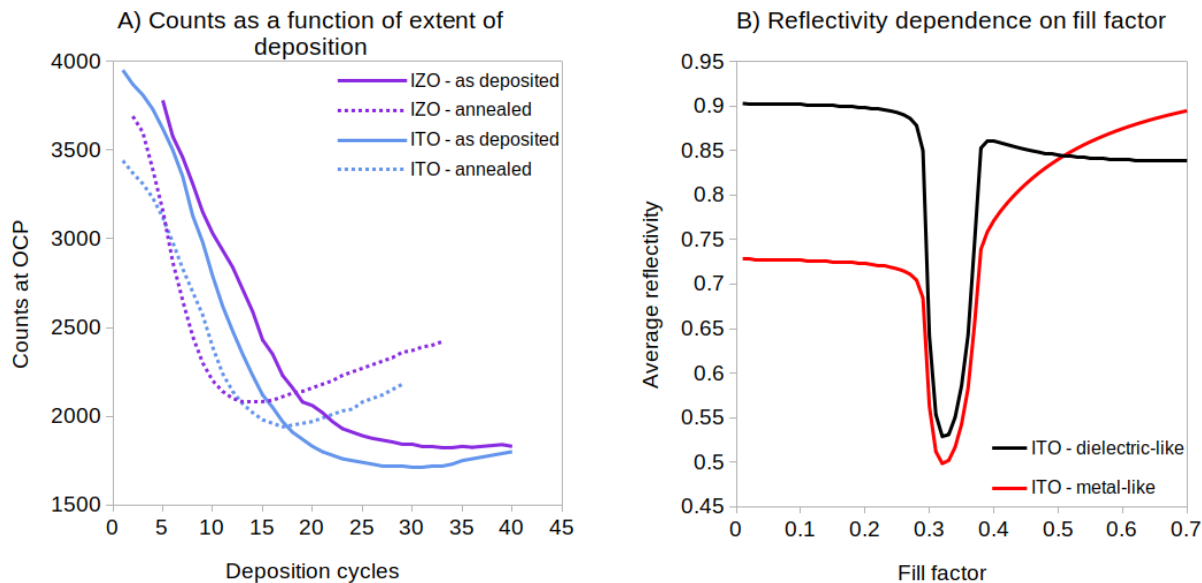


Figure 5-8: Overall substrate reflectivity as a function of deposition for different underlayers. A) plots the detector counts of the sample single beam spectrum as a stand-in for the reflectivity while B) is the directly computed sample reflectivity averaged over the entire spectral range.

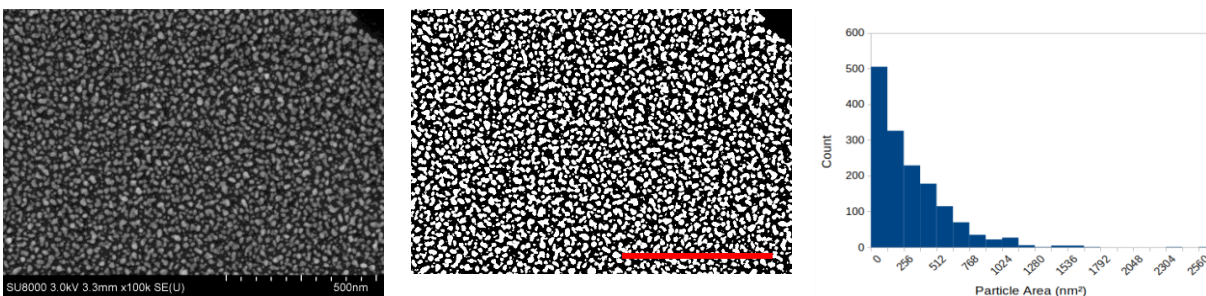
For each of the parameters plotted in the above figures, the annealed CMO films behave quite similarly. The optical responses of the unannealed films are likewise correlated. The differences between ITO and IZO seem not to be especially relevant to the behaviour of the films. This is sensible, as the optical properties of the two CMOs are quite similar, but annealing makes them considerably more conductive.

While the general empirical trends observed in the absorbance peak height, bimodality and overall reflectivity broadly confirm the EMA modelling results, the correlation is far from perfect, but this is likely not a failing of the underlying physics assumed in the model. As performed in this work, the electrodeposition of Au nanoparticle films on CMO underlayers yields SEIRAS substrates which depend quite significantly on whether the CMO is annealed or not -- much more than would be expected by the modelling results. The model assumes that identically structured Au nanoparticle films can be produced on top of different CMO layers, and the differences between dielectric-like and metal-like CMO seen in the B) subplots are therefore purely attributable to optical properties of the underlayer. However, when the optical properties of the underlayer are modified by annealing or changing the composition, the electrical properties are also modified. This makes it challenging to untangle the electrical effects of the substrate which cause different

electrodeposition conditions and hence morphology from the differences attributed to the different optical properties of the underlayer, assuming the composite layer on top is identical. For example, Figure 5-6A clearly demonstrates an enhancement maximum at a lower number of deposition cycles for annealed CMO films than unannealed ones. This is not predicted by the EMA modelled spectra. It is very likely that the deposition proceeded more rapidly on the annealed substrates due to their greater electrical conductivity. Since the deposition cycles are potentiostatic, the resistance of the electrode and the resistance of the solution will act as a voltage divider and the relative resistances will affect the current delivered. More conductive CMO electrodes will have a lower voltage dropped across them, and therefore the voltage across the solution is higher and a larger current can be delivered. Therefore, the number of deposition cycles (as described in section 3.3) does not map one-to-one onto the fill fraction of Au. The lack of a simple experimental method to measure the Au fill fraction presents a significant challenge in comparing experimental data to EMA-modelled results. The next section will describe one possible method to determine the volumetric fill fraction of an electrodeposited Au film.

### 5.3.1 Model to Extract Fill Factor From SEM of SEIRAS film

In order to model the permittivity of the Au composite films using EMA, the microscopic morphology of the metal particles must be characterized. The most critical parameter impacting the resulting permittivity of the composite effective medium is the fill factor, usually defined as the volumetric fraction occupied by each component material. To determine the fill factor, an SEM image of a representative sample (Figure 5-9a) was acquired and thresholded to generate a binary image with gold particles in white and the ITO underlayer in black (Figure 5-9b). The area-based fill fraction can be readily determined from the histogram (Figure 5-9c). The image was analyzed for particles in Image J for particles having an area between 10 and 3000 nm<sup>2</sup>. From the particle count and mean particle area, the mean particle radius and thus the total volume of the particles can be calculated, assuming spherical particles. The total volume of the field of view was calculated using the diameter as the height of the rectangular prism. Finally, the volume fill fraction is calculated by dividing the total volume of the particles by the volume of the field of view.



A) Original SEM image of electrodeposited Au on ITO electrode. B) Thresholded image used for image analysis. Scale bar is 500 nm. C) Histogram obtained by particle analysis using *Image J* (20 bins).

Figure 5-9: SEM of SEIRAS film to extract parameters for EMA modelling.

This method generates a reasonable fill factor, but it should be noted that selecting an appropriate threshold point to isolate the metal particles is a somewhat subjective process. The particles are also by no means perfect hemispheres (aspect ratio  $1.7 \pm 0.6$ ; circularity  $0.5 \pm 0.2$ ) and they have a large size variance (RSD = 0.9).

Correlating the film morphology obtained by SEM *post facto* with the *in-situ* performance of the layer presents additional difficulties. The Au-MOP system is chemically reactive, even without applying any potential.<sup>36,97</sup> These spontaneous chemical reactions can continue to occur after the last scan prior to emptying the cell. In addition, some of the gold particles do not appear to be strongly attached to the ITO electrode. Rinsing the substrate in preparation for SEM causes some particles of physisorbed Au to be washed off. Mobility of Au atoms at room temperature is fairly significant, and cycling the potential as is often done in an electrochemical experiment can cause significant restructuring of the Au layer,<sup>98</sup> depending on the electrolyte composition. A film which is first imaged by SEM and then loaded into a cell for an experiment may undergo appreciable morphological changes throughout the course of the experiment such that its optical properties do not correlate with the film morphology seen by SEM prior to the experiment.

### 5.3.2 Nucleation and Growth

Deposition of Au onto a Au electrode is more thermodynamically favourable than deposition of Au onto ITO.<sup>99</sup> Thus, in the presence of a large number of gold nuclei, further reduction will generally cause Au to be deposited on top of existing nuclei rather than causing further nucleation. This implies that there are generally two regimes to an electroreduction process: an early period where there are no or few nuclei in which nucleation is dominant and a later period

where growth of existing nuclei dominates. The overpotential applied during the early part of the deposition can increase the number of nuclei (high overpotentials) or instead cause concurrent nucleation and growth (lower overpotentials). As the nuclei begin to grow, a diffusion-controlled zone develops around each particle as it depletes the precursor in its vicinity. It appears that the range of fill factors investigated by the experiments reported in Figure 5-6 to Figure 5-8 is significantly less than the corresponding calculations from  $f = 0$  to  $f = 0.7$ . Additionally, the number of deposition cycles does not map linearly onto the fill factor, which can be seen by the stretched “tail” of the A) subplots of Figure 5-6 to Figure 5-8 compared to the corresponding calculations shown in the B) subplots. One hypothesis consistent with this observation is that a multilayer of particles develops which is a porous film. As further deposition cycles are carried out, further reduction of Au occurs at the topmost surface (closest to the bulk of solution) where Au ions are most abundant, increasing the thickness of the porous structure without significantly increasing the infill of the layer. Thus, early deposition cycles increase the fill factor to a greater extent than later deposition cycles. Figure 5-10c demonstrates that multilayers of Au particles are observed after extended electrodeposition, while significant void space remains.

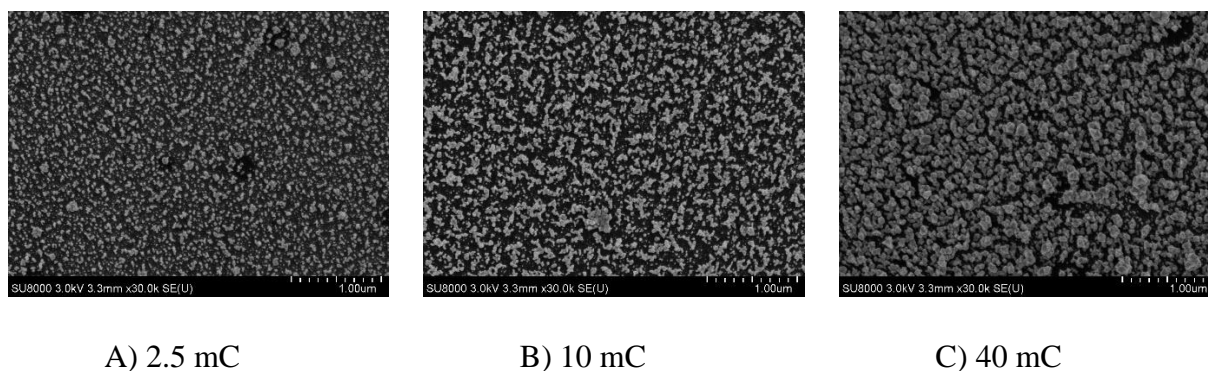


*Figure 5-10: Representative SEMs of electrodeposited Au on annealed ITO for the stated charges.*

Crystal defects on the electrode surface provide sites where nucleation is more likely to occur.<sup>100</sup> Thermal annealing changes the crystallinity of the CMO film as well as the number of defects. Of course, the conductivity of the CMO also increases as a result of annealing. For any given voltage, the current density will increase as the electrode’s conductivity increases. These changes in the defects, crystallinity, and electronic properties of the ITO cause major differences in the morphology of a metal film electrodeposited using that material as an electrode. In general, it can be seen in Figure 5-6 to Figure 5-8 that the deposition proceeded more rapidly in the annealed

films compared to their unannealed counterparts. The increased conductivity resulted in larger current densities and more reduction of gold per deposition cycle. In a computer model, it is trivial to change the optical properties of the ITO layer without changing the properties of the composite layer. However, experimentally changing the opto-electronic properties of ITO also changes the nature of the composite layer even (especially) if the electrodeposition procedure remains the same. As discussed in the section 5.3.1, accurately characterizing the composite films in terms of the simplified parameters of the Bruggeman model makes even semi-quantitative comparisons problematic. The computational model is useful for determining the effects of changing the CMO underlayer in isolation, but not in predicting the performance of an enhancing film produced by electrodeposition on that material.

### 5.3.3 CMO-Au Films Compared to Conventional Pure Au Films

To evaluate the polarization and angle-dependent responses of Au-ITO films, the spectra collected by my colleague Erick Lins (Figure 5-11) will be discussed in comparison to my modelling results.

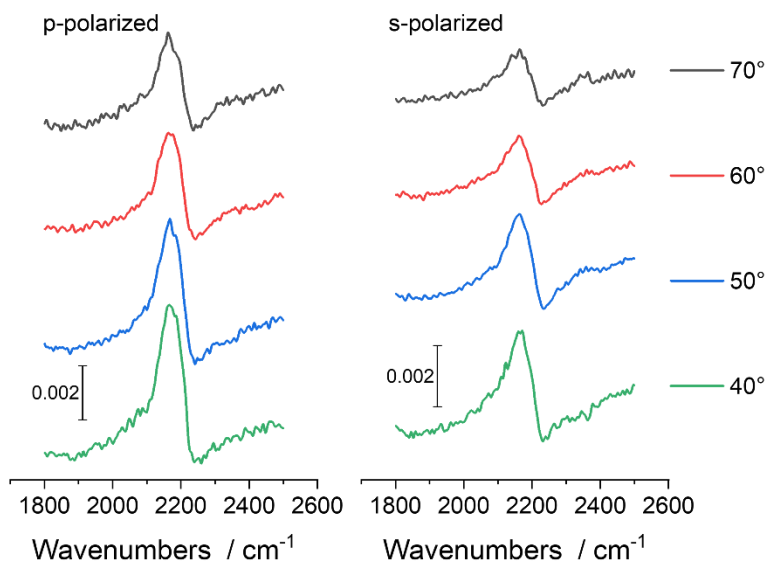


Figure 5-11: Angle-dependent SEIRAS of  $\nu_{CN}$  mode of cyanate for *p*- and *s*-polarized light.

In a traditional SEIRAS film, the metal must provide the conductivity required to behave as the working electrode. To account for both the high conductivity and the surface-enhancing properties, these films have been modelled as a continuous bulk metal underlayer which supports

the textured composite layer. As seen in the yellow traces in Figure 5-12, enhancing films supported on a continuous gold layer are highly dependent on the polarization with s-polarization providing a fraction of the signal compared p-polarization. Additionally, the p-polarized response is highly angle dependent, showing increased apparent absorption as the angle is increased above the critical angle, until a maximum absorbance is reached, and it declines at very large angles. This is typical behaviour for all-metal SEIRAS films and is borne out by experiments using both vacuum-deposited<sup>101</sup> and electrolessly-deposited<sup>102</sup> films.

This behaviour can be explained quite well by the physics underlying the surface selection rule, described in section 2.1.3. Given the conductive underlayer, s-polarized light is not expected to excite any observable modes. Above the critical angle, the fraction of p-polarized light capable of exciting modes that are allowed by the surface selection rule increases as the angle is increased, since the fraction of the electric field vector oscillating normal to the interface continually increases as the angle of incidence becomes more grazing. At extremely grazing angles, the interface becomes so highly reflective that a sharp decrease in the absorbance intensity is observed. It can be readily seen by looking at the equations for the Fresnel reflection coefficients (equations 2-12 and 2-14) that as  $\theta \rightarrow 90^\circ$ , then  $\cos(\theta) \rightarrow 0$ . The effect of the two refractive indices becomes less and less relevant and the reflection coefficients approach 1 for p-polarized light and -1 for s-polarized light. The observable consequence of this is that the overall reflectivity becomes very high and is independent of the refractive indices of the materials, so it is sensible that this would manifest as a lower apparent absorbance intensity.

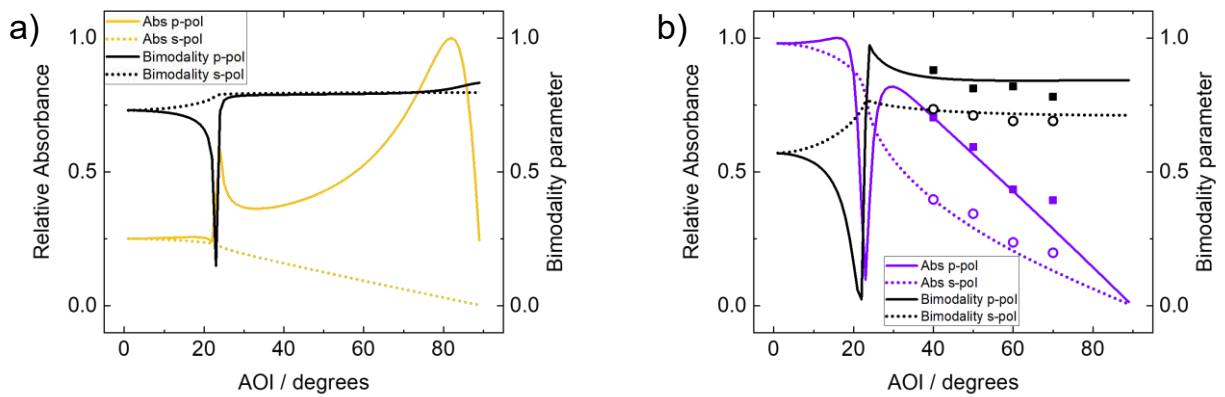


Figure 5-12: Comparison of enhancement and spectral line shapes for traditional all-metal SEIRAS films and ITO/Au composite films. The markers represent experimental data points

*calculated from the spectra shown in Figure 5-11. The experimental absorbance data was normalized such that the point at 40 degrees lies on the calculated curve.*

In contrast to the all-metal substrate, the CMO underlayer shows significantly different behaviour. Firstly, the difference between the absorbance peak heights of s- and p-polarization is much reduced. As shown in Figure 5-12b, both s- and p-polarized spectra trend downwards as the AOI is increased. Both these trends in the calculated spectra are validated by the experimental data (Figure 5-11 and data points in Figure 5-12b). This behaviour suggests that the underlayer is not behaving as a perfect conductor where the surface selection rule would apply. The impedance of the ITO prevents it from fully screening electric fields parallel to the interface, so a significant response is observed with s-polarized light. Under these conditions, p-polarized light is effective at all angles, so there is no increased signal at higher angles. The falloff in absorption intensity as the angle is increased is entirely a consequence of the Fresnel equations.

The p- and s-polarized spectra are approximately 35 and 100 times more intense, respectively than their corresponding spectrum calculated with the pure metal substrate also measured in the ATR-SEIRAS configuration. This is explained by calculating  $F$ , the electric field intensities, defined as:

$$F(z) = \frac{|E^+(z) - E^-(z)|^2}{|E^+(z=0)|^2} \quad 5-1$$

where  $z$  is the position along the optical axis (perpendicular to the interfaces), and  $E^+$  and  $E^-$  are the forward- and backward-propagating electric field amplitudes, respectively. These electric field amplitudes are intermediate quantities in the calculation of  $R$  and  $T$  using the TMM<sup>103</sup> and can be calculated independently for each polarization state. The field strengths at Bruggeman composite/H<sub>2</sub>O interface are plotted for pure Au and CMO-Au substrates in Figure 5-13. The field strengths are normalized by  $\cos \theta$  to account for the elongated beam spot at non-normal incidence. The relative enhancement difference is larger for s-polarization since the CMO underlayer substrate is capable of supporting electric fields parallel to the interface, while these are nearly totally suppressed by the conductive Au layer with the conventional substrate. The overall increase in absorption intensity can largely be attributed to the increased transparency of the ITO compared to the same thickness of continuous Au (see value of  $\kappa$  in Figure 5-1).

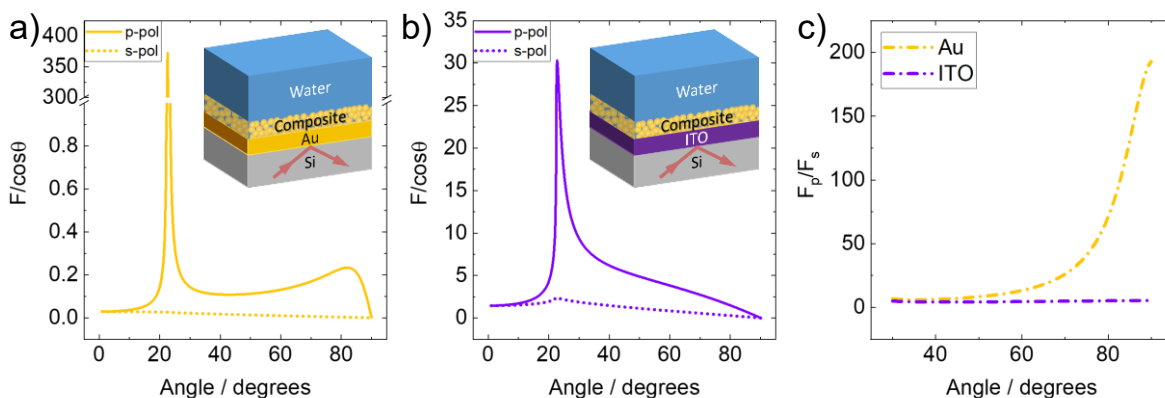


Figure 5-13: Electric field strength calculations for: yellow trace: Si, 25 nm Au, 25 nm composite,  $H_2O$ ; purple trace: Si, 25 nm ITO, 25 nm composite,  $H_2O$ .

The sharp absorption feature near 22 degrees deserves a brief comment. This is very near the critical angle for the prism-electrolyte interface. The addition of the thin films (conductive underlayer and enhancing composite layer) causes the angle to shift slightly. The angle will even shift slightly upon adsorption of a molecule, which is the premise underlying SPR. The large absorption is caused by exciting a PSPP and the angle corresponds to the momentum matching condition for a propagating surface mode with a polariton (section 2.7.3). Although the electric field is greatly enhanced at this angle, it occurs over too narrow a range to be broadly useful for ATR-SEIRAS and furthermore, the very low angle of incidence is experimentally challenging to access.

## 5.4 Spectral Line Shapes

As previously mentioned in section 2.1.3, the asymmetric spectral lineshapes frequently observed in ATR-SEIRAS spectra have been explained as a consequence of Fresnel's equations for adsorbates on moderately reflecting substrates.<sup>40,41</sup> This is somewhat unsatisfying, as it is not clear what threshold of optical parameters define the limits of “moderately reflecting”. The details of how lineshape asymmetry develops are obscured by TMM calculations, which prevent an intuitive appreciation of how moderate reflectivity arises from the material properties. This section develops an alternative, complementary explanation: that asymmetric lineshapes can be predicted with reasonable accuracy solely based on the material properties ( $n$  and  $\kappa$ ) of the Bruggeman composite layer.

To begin, when attempting to explain the unconventional spectral line shapes often observed in experimental spectra (see for example, the asymmetry in the peaks in Figure 5.7), it should first be recognized that the “absorbance” spectrum in the context of SEIRAS is not the same as a classical transmission experiment. The absorbance in a transmission experiment quantifies the power loss of an absorbing medium by measuring the irradiance (units of  $W \cdot m^{-2}$ ) spectrum in the presence and absence of an absorbing analyte. The absorption coefficient ( $\alpha$ ) can then be calculated by recognizing that the irradiance ( $I$ ) in a lossy medium decays exponentially as a function of distance ( $z$ ), according to the Beer-Lambert Law:  $I = I_0 \exp(-\alpha z)$ . In SEIRAS, what is often discussed as an “absorbance” spectrum is actually a differential reflectance spectrum, which is computed analogously to absorbance in a transmission experiment by the expression:

$$-\log\left(\frac{R_{matrix+adsorbate}}{R_{matrix}}\right).$$

In a transmission experiment, the change in the real part of the refractive index of the matrix by the introduction of an absorbing molecule is very small because it is dilute. Furthermore, it does not significantly impact the measurement because the matrix and analyte are thoroughly mixed and behave as a single optical material without any interface. Thus, the molar absorptivity is fundamentally a measurement of how the absorber changes the matrix's value of  $\kappa$ , and the change in  $n$  does not substantially affect the measurement. Conversely, in ATR-SEIRAS the system is well-described as a series of stratified layers: the prism, the underlayer (if any), the enhancing composite film, and the matrix. If the analyte adsorbs on to the surface of the enhancing film, one

can consider two states: 1) a “reference” state where the composite film is composed solely of the electrolyte and the metal and 2) a “sample” state where the adsorbate is also present. Because the adsorbate is localized to the surface of the film, its local concentration is very high, and it displaces some of the electrolyte. Accordingly, the real part of the refractive index of the composite film undergoes a small, but significant change in  $n$  upon adsorption of the analyte. Because of the system of layers, changes in  $n$  will cause changes in the interfacial reflectivity in accordance with the Fresnel reflection coefficients.

As stated in the introduction to this section, it is tempting to examine the expression for reflectivity and analyze how its value would change with small changes to the refractive index of the composite layer. The fully expanded complex expression for the reflectivity of a 3-phase system contains a bewildering number of terms. Simply examining an expression with so many terms does not provide intuition as to how a small change to the refractive index caused by the adsorbate will affect the overall reflectivity.<sup>20</sup> Although the presence of an adsorbate will dissipate energy at the resonant frequency of its vibrational mode, it is possible that the overall reflectivity of that interface at that frequency will increase as a result of the modulated permittivity, which is simply a result of the Fresnel equations. It is somewhat unsatisfying to lack a simple theoretical intuition, however, the reflectivity can be numerically evaluated over a broad range of conditions to determine the set of conditions under which it is expected that bimodal or inverted line shapes will appear.

Rather than analyzing the expressions in detail, this work has attempted to draw generalizations by brute numerical evaluation under a broad range of conditions. This is a sort of *in silico* empirical approach: to simulate various types of composite films and observe trends in the results. Although it lacks an intuitive mathematical representation of the underlying phenomenon, the computation is fairly rapid, and the domain of applicability can be extended by performing additional calculations under the parameter space of interest. The most significant result of this approach is the observation that the permittivity of the composite layer as a function of frequency is an excellent predictor of the line shape of the computed absorbance. First, the real and imaginary refractive index (RI) components of the composite layer in the presence of adsorbate are normalized by the respective components of the RI without the adsorbate. Over the small spectral range of a vibrational absorption band, the RI of the composite layer in the absence of the

adsorbate is nearly constant, however a pointwise normalization was performed. The spectral line shape of the product of the normalized  $n$  and  $\kappa$  matches the general shape of the calculated absorbance very well for p-polarized light and all angles and for s-polarized light at lower angles (Figure 5-14). This can be somewhat rationalized by recognizing that the imaginary component of  $\epsilon$  scales with the product of  $n$  and  $\kappa$  (recall that  $\epsilon = (n + ik)^2$ ), which accounts for absorptive loss. This is not a perfect predictor; at grazing angles with s-polarized light, there is an additional region of bimodality occurring above the end of the percolation transition (typically around  $f = 0.4$ ) which is not demonstrated in product of  $n$  and  $\kappa$ .

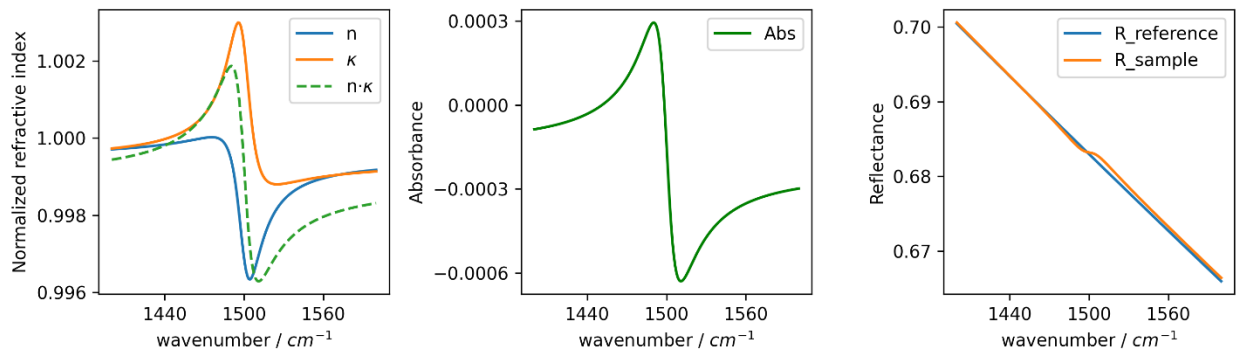


Figure 5-14: From left to right: calculated RI, absorbance, and reflectance for the 3-phase Bruggeman formula for spheres containing metal, organic, and water. Reflectivity and absorbance are calculated at 60 degrees using p-polarized light. These plots were calculated at  $f = \frac{1}{3}$ , however the product of the normalized  $n$  and  $\kappa$  values (dashed green trace) matches the line shape of the absorbance fairly well at all values of  $f$ .

If it is accepted that the product of  $n$  and  $\kappa$  is a reasonable predictor of the absorbance line shape, the origin of the asymmetric line shapes near the percolation threshold can be understood by examining a simplified case using a two-phase Bruggeman model for spheres (in 3-dimensions).

$$f \frac{\epsilon_{met} - \epsilon_{BR}}{\epsilon_{met} + 2\epsilon_{BR}} + (1 - f) \frac{\epsilon_{org} - \epsilon_{BR}}{\epsilon_{org} + 2\epsilon_{BR}} = 0 \quad 5-2$$

Expanding and simplifying yields the following polynomial:

$$-2(\epsilon_{BR})^2 + [(3f - 1)\epsilon_{met} + (2 - 3f)\epsilon_{org}](\epsilon_{BR})^1 + \epsilon_{met}\epsilon_{org}(\epsilon_{BR})^0 = 0 \quad 5-3$$

The roots of this polynomial are:

$$\epsilon_{BR} = \frac{(3f - 1)\epsilon_{met} - \epsilon_{org} \pm \sqrt{(9f^2 - 6f + 1)\epsilon_{met}^2 + (10 - 6f)\epsilon_{met}\epsilon_{org} + \epsilon_{org}^2}}{4} \quad 5-4$$

At the percolation threshold in 3-dimensions ( $f = \frac{1}{3}$ ), the roots simplify considerably:

$$\epsilon_{BR} = \frac{\epsilon_{org} \pm \sqrt{8\epsilon_{met}\epsilon_{org} + \epsilon_{org}^2}}{4} \quad 5-5$$

Recognizing that the modulus of  $\epsilon_{org}$  is much less than the modulus of  $\epsilon_{met}$ , the dominant term will be  $\pm \frac{1}{4}\sqrt{8\epsilon_{met}\epsilon_{org}}$ , which can further be expressed as  $\pm \frac{\sqrt{2}}{2}\eta_{met}\eta_{org}$ , in other words the product of the complex refractive indices of the two components and a scalar. To see why this product causes bimodal line shape, note that multiplying a complex number by another complex number can be described as a rotation and a scaling of a 2D vector on the complex plane. This rotation and scaling has the effect of transforming the dispersive line shape of  $n_{org}$  into an inverted Lorentzian while transforming the Lorentzian line shape of  $\kappa_{org}$  into a dispersive one. Complex multiplication is more intuitive in polar form, so consider that in the mid-IR  $\eta_{met} \approx 1 + 30i$ , which has an argument of nearly  $\frac{\pi}{2}$  rad. Multiplying any complex number by  $\eta_{met}$  will therefore have the approximate effect of rotating the vector on the complex plane by  $\frac{\pi}{2}$ , along with some scaling. This rotation will cause  $Re(\epsilon_{Bruggeman})$  to adopt the negative line shape of  $\kappa_{org}$  and will cause  $Im(\epsilon_{Bruggeman})$  to adopt the same line shape of  $n_{org}$ . Figure 5-15 demonstrates the rotation of the complex refractive index of the organic component upon multiplication by the metal's refractive index. Finally,  $\eta_{Bruggeman}$  is calculated as  $\sqrt{\epsilon_{Bruggeman}}$ . Since the arguments are added when complex numbers are multiplied, the argument of  $\eta_{Bruggeman}$  will be half of the argument of  $\epsilon_{Bruggeman}$ ; approximately  $\frac{\pi}{4}$ , as shown in column 2 of Figure 5-15. This will cause mixing of the real and imaginary line shapes, so neither component will be a pure Lorentzian or pure dispersive shape. The product of these “mixed” lineshapes of  $n_{Bruggeman}$  and  $\kappa_{Bruggeman}$  yields a bimodal line shape, which appears similar to the leftmost plot in Figure 5-14.

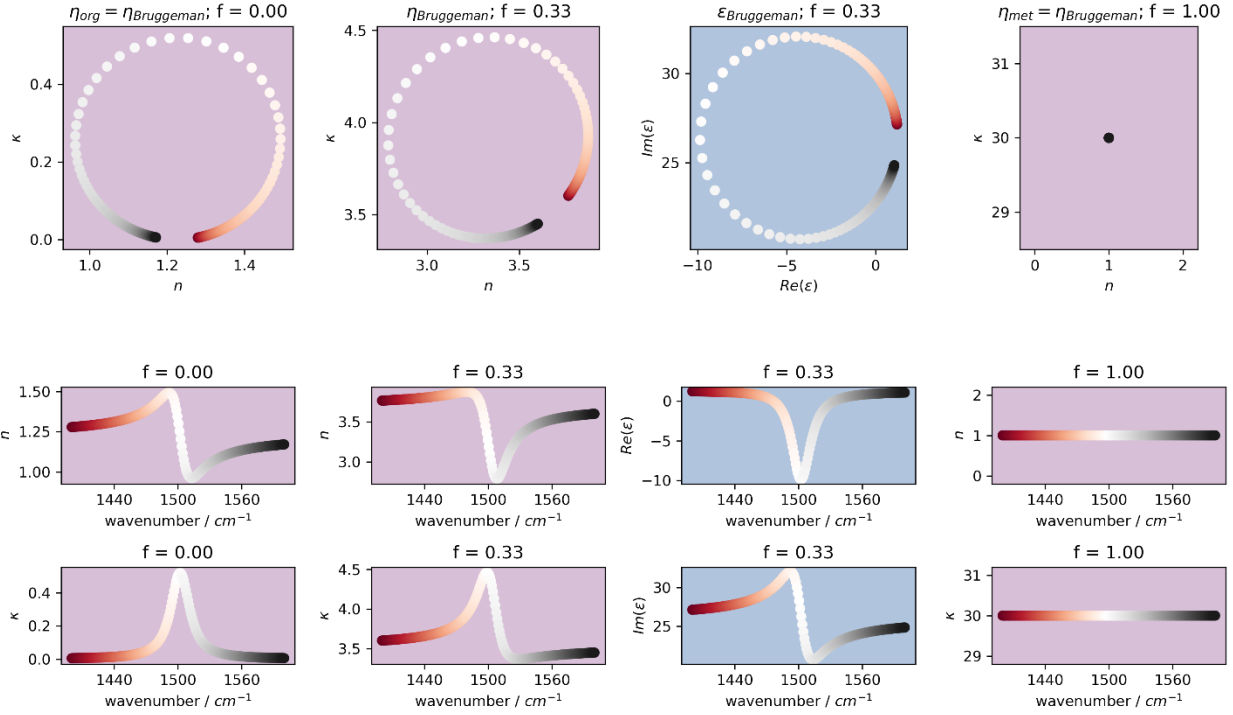


Figure 5-15: The refractive indices of a 2-phase Bruggeman composite are in lavender while the permittivities are in blue. The fill-factor increases from left to right; the first column ( $f = 0$ ) corresponds to pure organic ( $\eta_{org}$ ), while the last column ( $f = 1$ ) corresponds to pure metal ( $\eta_{met} = 1 + 30i$ ). The organic is modelled as a Lorentz oscillator with parameters:  $\nu_0 = 1500 \text{ cm}^{-1}$ ;  $\gamma = 20 \text{ cm}^{-1}$ ;  $\epsilon_\infty = 1.5$ . The top row plots  $\eta$  or  $\epsilon$  on the complex plane, while the bottom two rows plot the components as a function of frequency. When  $f = 1/3$ ,  $\epsilon_{BR}$  is dominated by the product of  $\eta_{met}$  and  $\eta_{org}$ , which manifests as a rotation and scaling of the  $\eta_{org}$  in the complex plane (top row,  $\eta_{org}$  in the first column is rotated and scaled to give  $\epsilon_{BR}$  in the middle column). This appears in the individual components as a swap of their line shapes and an inversion in the Lorentzian (bottom rows, middle column).

The greatest level of enhancement, as well as the greatest distortion of the line shapes occurs in the vicinity of  $f = \frac{1}{3}$ , which is the percolation threshold in 3-dimensions as defined by the Bruggeman model. It is noteworthy that this is the approximate region where the values of  $n$  and  $\kappa$  become equal, which is the condition of an epsilon near zero mode (ENZ). At low fill fractions, the RI of the composite layer is essentially that of the non-metallic phase, while at high fill fractions, it is dominated by the RI of the metal. As the fill factor is increased,  $n$  of the composite layer increases to a maximum around the percolation threshold and then decreases while  $\kappa$  increases continuously.

In summary, by knowing the optical properties of the materials that constitute the Bruggeman layer, it's possible to predict the spectral lineshape without reference to the Fresnel equations. From a computational perspective, the TMM is such an efficient and rapid algorithm that the time savings of calculating the product of  $n$  and  $\kappa$  in lieu of the full TMM is not especially significant. However, this does require an implementation of both the TMM and the EMA, while the method described here obviates the need to implement the TMM. Again, it should be emphasized that the major determinant of both “moderate reflectivity” and lineshape asymmetry in a Bruggeman-modelled material is the fill factor. In cases where the fill factor may be reliably determined, such as for nanoparticle films produced by electron beam lithography (EBL), it may be possible to use the product of  $n$  and  $\kappa$  obtained by the Bruggeman EMA using the fill factor calculated from the CAD file to be written to predict the spectral asymmetry prior to producing the substrates. Of course, this approach will have the same limitations as the Bruggeman EMA, most importantly that it neglects near-field effects.

To conclude, the permittivity functions of each layer in the CMO-Au hybrid substrates can be defined using tabulated values, the Drude-Lorentz model, or the Bruggeman EMA. This enabled the analysis of SPP modes, which were determined to be largely insignificant under the experimental conditions investigated. The permittivity functions also enable the calculation of simulated ATR-SEIRAS absorbance spectra, which can be compared to experimental spectra. The qualitative predictions of the modelled spectra reproduce the observed trends in enhancement, bimodality and reflectivity quite successfully. The EMA/TMM results clearly highlight the overwhelming importance of the fill factor parameter as the major determining factor of the performance of the composite film as an enhancing surface. This reveals that the major limitation in using EMA to model experimental nanoparticle films is the difficulty in determining the volume fill fractions of the particles. Unlike conventional all-metal films, CMO-Au hybrid films are most enhancing nearest to the critical angle, and there is a much more significant s-polarized signal. These differences were shown to be consistent with electric field strength calculations at the composite/H<sub>2</sub>O interface as a function of angle and polarization. Finally, an analysis of spectral lineshapes was conducted to gain an appreciation of what is meant by “moderate reflectivity” in terms of more fundamental material parameters.

## 6 CONCLUSIONS AND FUTURE WORK

An algorithm for the Bruggeman EMA was developed to calculate an arbitrary number of ellipsoidal particle types. This model combined with the transfer matrix method provides quite a successful model of the experimental SEIRAS films. The modelling predicts the asymmetric line spectral line shapes observed, in addition to the general trend of the enhancement as a function of the extent of deposition. If upright, Lorentzian bands are desired, the deposition should be halted before the maximum signal is achieved. A shortcoming of the EMA approach is revealed by comparing the modelled spectra as a function of fill factor to the experimental spectra over the course of the deposition. The number of deposition cycles does not correlate linearly to increasing the fill factor, although broadly over time, as the deposition proceeds, the fill factor increases.

The Drude model was used to describe the properties of CMOs. One significant difference of the CMO-metal substrates compared to all-metal films is the angle-dependent behaviour. The field strength is highest near the critical angle and there is a larger s-polarized signal than traditional films, which is rationalized by the lower conductivity of the CMO and the loosening of the surface selection rule. The mechanism of enhancement as applied to CMO-Au films was also reviewed. A complete analysis would require the calculation of the local field strengths by some finite element method. Propagating surface plasmon polaritons are unlikely to play a major role in the enhancement provided in a typical electrochemical SEIRAS experiment due to the restricted conditions of AOI and the narrow spectral range over which plasmons are operative. It is possible that enhancement could be improved by exciting surface plasmons through careful selection of the AOI and operating within a narrow range of fill factors. ENZ modes are observable where the CMO films are sufficiently thin, although they occur at a higher frequency than what is generally useful for mid-IR spectroscopy, and do not account for the broadband enhancement observed experimentally. The improved signal of CMO-Au hybrid films compared to pure Au films is largely attributable to the increased transparency of CMOs at mid-IR wavelengths compared to Au.

A practitioner of ATR-SEIRAS desires a means to reliably produce a highly enhancing film, while avoiding problematic asymmetric lineshapes that often invalidate quantification and spectral library searches. The EMA calculations described in this work are a helpful tool directing the development of new, more consistent films. However, one of the major limitations of applying the results of basic EMA calculations to the experimental creation of composite films is the lack of accessible and inexpensive preparation techniques to create highly controlled substrates having well-defined and easily characterized fill factors. There are two possible approaches to deal with this challenge: 1) develop more refined models in terms of parameters that can be readily measured, or 2) develop new synthetic procedures which create composite films which match the simple morphologies described by basic EMAs. A possible example of an improved model might include combining models of nucleation and growth to better relate the “extent of deposition” parameter in an experiment to the theoretical “fill factor” parameter required by EMA. Models from the percolation theory literature, such as making use of complete SEM images to better determine fill factors by accounting for both small and large-scale features appear to be a logical extension of EMA.<sup>58</sup>

The analysis of SPPs is an exciting possibility brought forth by this thesis’s contribution of providing the means to calculate the permittivity functions of both the supporting CMO layer and the metal composite layer. Despite not being able to conclusively attribute the surface enhancement of CMO-Au substrates to particular plasmonic modes, the TMM/EMA approach presents an empirically grounded modelling tool to assist in the interpretation and development of substrates for ATR-SEIRAS. Commonly available variable angle accessories for FTIR spectrometers have their best throughput in the approximate range of 40 to 70° and ATR prisms typically have angles cut in this range to minimize reflective losses. There is no fundamental reason why variable angle accessory and corresponding prisms couldn’t be optimized closer to the critical angle of the prism (~20 to 30°) which might significantly increase the level of enhancement as suggested by the field strength calculations and PSPP analysis presented in this work.

Many other models exist which would be even better suited to evaluate the resonances of structures in the low frequency domain (dimensions of structures smaller than the frequency of light). There are certainly more advances and extensions which could improve the EMA models presented here, but in the opinion of this author, exploring other categories of models may prove

to be a more informative approach. One interesting method is Finite Differences Frequency Domain (FDFD), which being a frequency domain method, is efficient for resonant systems and allows local fields to be visualized. There has recently been a publication describing how to implement this type of model at a level which should be accessible for the average chemist.<sup>104</sup>

Of course, there are several commercial software packages available that enable advanced calculations to be performed without requiring the user to understand the underlying physics and math. If this approach is utilized, it is important for the user to take it upon themselves to learn about the domain of applicability and the limitations of the model, so they do not misinterpret the results. One benefit of implementing a model for oneself is that the implied assumptions of the model will be understood, curtailing undue confidence in modelling results.

As discussed in section 2.1.1, ATR-SEIRAS remains a rather marginal technique among the multitude of surface-enhanced vibrational spectroscopies. It is the opinion of this author that the production of ATR-SEIRAS substrates having a consistent enhancement factor is the major factor limiting its more widespread adoption. It is unlikely that ATR-SEIRAS will ever supplant SPR as the dominant technique in commercial sensors optimized for sensitivity and selectivity of a specific biomolecule as a point-of-care diagnostic, for example. However, there remains much room for growth in the adoption of the technique in research environments for studying the binding of substrates in electrocatalysis. This thesis aims to take an early step into making ATR-SEIRAS more of a quantitative technique by demonstrating a wide range of substrates that can be produced using CMO-Au films. The fill factor was identified as the critical parameter that must be controlled to create reproducible enhancing films with upright absorbance peaks. It is likely that further research into producing better ATR-SEIRAS films will be assisted by using a model capable of predicting the spectral response in terms of easily accessible experimental parameters, and the EMA/TMM model described here demonstrates the promise of such an approach.

## 7 REFERENCES

- (1) Alvarez-Malmagro, J.; García-Molina, G.; López De Lacey, A. Electrochemical Biosensors Based on Membrane-Bound Enzymes in Biomimetic Configurations. *Sensors* **2020**, *20* (12), 3393. DOI: 10.3390/s20123393.
- (2) Perro, A.; Lebourdon, G.; Henry, S.; Lecomte, S.; Servant, L.; Marre, S. Combining Microfluidics and FT-IR Spectroscopy: Towards Spatially Resolved Information on Chemical Processes. *React. Chem. Eng.* **2016**, *1* (6), 577–594. DOI: 10.1039/C6RE00127K.
- (3) Andvaag, I. R.; Morhart, T. A.; Clarke, O. J. R.; Burgess, I. J. Hybrid Gold–Conductive Metal Oxide Films for Attenuated Total Reflectance Surface Enhanced Infrared Absorption Spectroscopy. *ACS Appl. Nano Mater.* **2019**, *2* (3), 1274–1284. DOI: 10.1021/acsanm.8b02155.
- (4) Thi Phan, V. T.; Andvaag, I. R.; Boyle, N. D.; Flaman, G. T.; Unni, B.; Burgess, I. J. Surface Sensitive Infrared Spectroelectrochemistry Using Palladium Electrodeposited on ITO-Modified Internal Reflection Elements. *Phys. Chem. Chem. Phys.* **2022**, *24* (5), 2925–2933. DOI: 10.1039/D1CP05130J.
- (5) Nishikawa, Y.; Fujiwara, K.; Shima, T. Qualitative Analysis of Nanogram Samples with Fourier Transform Infrared Transmission Surface Electromagnetic Wave Spectroscopy. *Appl. Spectrosc.* **1990**, *44* (4), 691–694. DOI: 10.1366/0003702904087280.
- (6) Nishikawa, Y.; Nagasawa, T.; Fujiwara, K.; Osawa, M. Silver Island Films for Surface-Enhanced Infrared Absorption Spectroscopy: Effect of Island Morphology on the Absorption Enhancement. *Vib. Spectrosc.* **1993**, *6* (1), 43–53. DOI: 10.1016/0924-2031(93)87021-K.
- (7) Bjerke, A. E.; Griffiths, P. R.; Theiss, W. Surface-Enhanced Infrared Absorption of CO on Platinized Platinum. *Anal. Chem.* **1999**, *71* (10), 1967–1974. DOI: 10.1021/ac981093u.
- (8) Suzuki, Y.; Osawa, M.; Hatta, A.; Suëtaka, W. Mechanism of Absorption Enhancement in Infrared ATR Spectra Observed in the Kretschmann Configuration. *Appl. Surf. Sci.* **1988**, *33–34*, 875–881. DOI: 10.1016/0169-4332(88)90393-5.
- (9) Otto, A. Excitation of Nonradiative Surface Plasma Waves in Silver by the Method of Frustrated Total Reflection. *Z. Physik* **1968**, *216* (4), 398–410. DOI: 10.1007/BF01391532.

- (10) Kretschmann, E.; Raether, H. Notizen: Radiative Decay of Non Radiative Surface Plasmons Excited by Light. *Z. Naturforsch. A* **1968**, *23* (12), 2135–2136. DOI: 10.1515/zna-1968-1247.
- (11) Chen, J.-Q.; Huang, Q.-S.; Qi, R.-Z.; Feng, Y.-F.; Feng, J.-T.; Zhang, Z.; Li, W.-B.; Wang, Z.-S. Effects of Sputtering Power and Annealing Temperature on Surface Roughness of Gold Films for High-Reflectivity Synchrotron Radiation Mirrors. *Nucl. Sci. Tech.* **2019**, *30* (7), 107. DOI: 10.1007/s41365-019-0635-x.
- (12) Liu, C.-W.; Tsai, T.-C.; Osawa, M.; Chang, H.-C.; Yang, R.-J. Aptamer-Based Sensor for Quantitative Detection of Mercury (II) Ions by Attenuated Total Reflection Surface Enhanced Infrared Absorption Spectroscopy. *Anal. Chim. Acta* **2018**, *1033*, 137–147. DOI: 10.1016/j.aca.2018.05.037.
- (13) Yang, Y.-Y.; Zhang, L.-N.; Osawa, M.; Cai, W.-B. Surface-Enhanced Infrared Spectroscopic Study of a CO-Covered Pt Electrode in Room-Temperature Ionic Liquid. *J. Phys. Chem. Lett.* **2013**, *4* (10), 1582–1586. DOI: 10.1021/jz400657t.
- (14) Hartstein, A.; Kirtley, J. R.; Tsang, J. C. Enhancement of the Infrared Absorption from Molecular Monolayers with Thin Metal Overlayers. *Phys. Rev. Lett.* **1980**, *45* (3), 201–204. DOI: 10.1103/PhysRevLett.45.201.
- (15) Miyake, H.; Ye, S.; Osawa, M. Electroless Deposition of Gold Thin Films on Silicon for Surface-Enhanced Infrared Spectroelectrochemistry. *Electrochem. Commun.* **2002**, *4* (12), 973–977. DOI: 10.1016/S1388-2481(02)00510-6.
- (16) Ohta, N.; Nomura, K.; Yagi, I. Electrochemical Modification of Surface Morphology of Au/Ti Bilayer Films Deposited on a Si Prism for in Situ Surface-Enhanced Infrared Absorption (SEIRA) Spectroscopy. *Langmuir* **2010**, *26* (23), 18097–18104. DOI: 10.1021/la102970r.
- (17) Corson, E. R.; Kas, R.; Kostecky, R.; Urban, J. J.; Smith, W. A.; McCloskey, B. D.; Kortlever, R. In Situ ATR–SEIRAS of Carbon Dioxide Reduction at a Plasmonic Silver Cathode. *J. Am. Chem. Soc.* **2020**, *142* (27), 11750–11762. DOI: 10.1021/jacs.0c01953.
- (18) Yang, X. M.; Zhong, Z. W.; Diallo, E. M.; Wang, Z. H.; Yue, W. S. Silicon Wafer Wettability and Aging Behaviors: Impact on Gold Thin-Film Morphology. *Mater. Sci. Semicond. Process.* **2014**, *26*, 25–32. DOI: 10.1016/j.mssp.2014.03.044.
- (19) Abbott, W. M.; Murray, C. P.; Ní Lochlainn, S.; Bello, F.; Zhong, C.; Smith, C.; McCarthy, E. K.; Downing, C.; Daly, D.; Petford-Long, A. K.; McGuinness, C.; Chunin, I. I.; Donegan, J. F.; McCloskey, D. Comparison of Metal Adhesion Layers for Au Films in Thermoplasmonic Applications. *ACS Appl. Mater. Interfaces* **2020**, *12* (11), 13503–13509. DOI: 10.1021/acsami.9b22279.
- (20) Ortiz, R.; Cuesta, A.; Márquez, O. P.; Márquez, J.; Méndez, J. A.; Gutiérrez, C. Origin of the Infrared Reflectance Increase Produced by the Adsorption of CO on Particulate Metals

- Deposited on Moderately Reflecting Substrates. *J. Electroanal. Chem.* **1999**, *465* (2), 234–238. DOI: 10.1016/S0022-0728(99)00099-6.
- (21) McPherson, I. J.; Ash, P. A.; Jones, L.; Varambhia, A.; Jacobs, R. M. J.; Vincent, K. A. Electrochemical CO Oxidation at Platinum on Carbon Studied through Analysis of Anomalous in Situ IR Spectra. *J Phys Chem C Nanomater Interfaces* **2017**, *121* (32), 17176–17187. DOI: 10.1021/acs.jpcc.7b02166.
- (22) Zhu, S.; Li, T.; Cai, W.-B.; Shao, M. CO<sub>2</sub> Electrochemical Reduction As Probed through Infrared Spectroscopy. *ACS Energy Lett.* **2019**, *4* (3), 682–689. DOI: 10.1021/acsenerylett.8b02525.
- (23) Leverette, C. L.; Jacobs, S. A.; Shanmukh, S.; Chaney, S. B.; Dluhy, R. A.; Zhao, Y.-P. Aligned Silver Nanorod Arrays as Substrates for Surface-Enhanced Infrared Absorption Spectroscopy. *Appl Spectrosc* **2006**, *60* (8), 906–913. DOI: 10.1366/000370206778062084.
- (24) Bibikova, O.; Haas, J.; López-Lorente, Á. I.; Popov, A.; Kinnunen, M.; Ryabchikov, Y.; Kabashin, A.; Meglinski, I.; Mizaikoff, B. Surface Enhanced Infrared Absorption Spectroscopy Based on Gold Nanostars and Spherical Nanoparticles. *Anal. Chim. Acta* **2017**, *990*, 141–149. DOI: 10.1016/j.aca.2017.07.045.
- (25) Soto-Nieto, F.; Farías, R.; Reyes-López, S. Y. Sol–Gel and Electrospinning Synthesis of Silica–Hydroxyapatite–Silver Nanofibers for SEIRAS and SERS. *Coatings* **2020**, *10* (10). DOI: 10.3390/coatings10100910.
- (26) Li, J. F.; Huang, Y. F.; Ding, Y.; Yang, Z. L.; Li, S. B.; Zhou, X. S.; Fan, F. R.; Zhang, W.; Zhou, Z. Y.; Wu, D. Y.; Ren, B.; Wang, Z. L.; Tian, Z. Q. Shell-Isolated Nanoparticle-Enhanced Raman Spectroscopy. *Nature* **2010**, *464* (7287), 392–395. DOI: 10.1038/nature08907.
- (27) Chen, J.; Guo, L.; Qiu, B.; Lin, Z.; Wang, T. Application of Ordered Nanoparticle Self-Assemblies in Surface-Enhanced Spectroscopy. *Mater. Chem. Front.* **2018**, *2* (5), 835–860. DOI: 10.1039/C7QM00557A.
- (28) Wang, H.-F.; Yan, Y.-G.; Huo, S.-J.; Cai, W.-B.; Xu, Q.-J.; Osawa, Masatoshi. Seeded Growth Fabrication of Cu-on-Si Electrodes for in Situ ATR-SEIRAS Applications. *Electrochim. Acta* **2007**, *52* (19), 5950–5957. DOI: 10.1016/j.electacta.2007.03.042.
- (29) Yang, G.; Hallinan, D. T. Gold Nanoparticle Monolayers from Sequential Interfacial Ligand Exchange and Migration in a Three-Phase System. *Sci. Rep.* **2016**, *6* (1), 35339. DOI: 10.1038/srep35339.
- (30) Osawa, M.; Kuramitsu, M.; Hatta, A.; Suëtaka, W.; Seki, H. Electromagnetic Effect in Enhanced Infrared Absorption of Adsorbed Molecules on Thin Metal Films. *Surf. Sci. Lett.* **1986**, *175* (3), L787–L793. DOI: 10.1016/0167-2584(86)90330-0.

- (31) Priebe, A.; Fahsold, G.; Pucci, A. Surface Enhanced Infrared Absorption of CO on Smooth Iron Ultrathin Films. *Surf. Sci.* **2001**, *482–485*, 90–95. DOI: 10.1016/S0039-6028(01)00780-4.
- (32) Perry, D. A.; Borchers, R. L.; Golden, J. W.; Owen, A. R.; Price, A. S.; Henry, W. A.; Watanabe, F.; Biris, A. S. Surface-Enhanced Infrared Absorption on Elongated Nickel Nanostructures. *J. Phys. Chem. Lett.* **2013**, *4* (22), 3945–3949. DOI: 10.1021/jz402092y.
- (33) Yoshidome, T.; Kamata, S. Surface Enhanced Infrared Spectra with the Use of the Pb Film and Its Application to the Microanalyses. *Anal. Sci.* **1997**, *13* (Supplement), 351–354. DOI: 10.2116/analsci.13.Supplement\_351.
- (34) Miki, A.; Ye, S.; Osawa, M. Surface-Enhanced IR Absorption on Platinum Nanoparticles: An Application to Real-Time Monitoring of Electrocatalytic Reactions. *Chem. Commun.* **2002**, *14*, 1500–1501. DOI: 10.1039/B203392E.
- (35) Aroca, R.; Price, B. A New Surface for Surface-Enhanced Infrared Spectroscopy: Tin Island Films. *J. Phys. Chem. B* **1997**, *101* (33), 6537–6540. DOI: 10.1021/jp971601o.
- (36) Simon, S.; Olumorin, T. I.; Guo, B.; Burgess, I. J. Role of Au(I) Intermediates in the Electrochemical Formation of Highly Anisotropic Gold Nanostructures with Near-IR SERS Applications. *J. Phys. Chem. C* **2016**, *120* (45), 26150–26158. DOI: 10.1021/acs.jpcc.6b09202.
- (37) Hu, Y.; López-Lorente, Á. I.; Mizaikoff, B. Graphene-Based Surface Enhanced Vibrational Spectroscopy: Recent Developments, Challenges, and Applications. *ACS Photonics* **2019**, *6* (9), 2182–2197. DOI: 10.1021/acsp Photonics.9b00645.
- (38) Zheng, M.-S.; Sun, S.-G. In Situ FTIR Spectroscopic Studies of CO Adsorption on Electrodes with Nanometer-Scale Thin Films of Ruthenium in Sulfuric Acid Solutions. *J. Electroanal. Chem.* **2001**, *500* (1), 223–232. DOI: 10.1016/S0022-0728(00)00476-9.
- (39) Fahsold, G.; Krauth, O.; Priebe, A.; Sinther, M.; Starzetz, P.; Pucci, A. Anomalous Infrared Absorption of Adsorbates on Ultrathin Metal Films. *Proc. Third Vietnam. Ger. Workshop Phys. Eng. Ho Chi Minh City 03-08 April 2000* **2000**.
- (40) Pecharroman, C.; Cuesta, A.; Gutierrez, C. Comments on the Paper by M.-S. Zheng and S.-G. Sun Entitled “In Situ FTIR Spectroscopic Studies of CO Adsorption on Electrodes with Nanometer-Scale Thin Films of Ruthenium in Sulfuric Acid Solutions.” *J. Electroanal. Chem.* **2002**, *529* (2), 145–154. DOI: 10.1016/S0022-0728(02)00968-3.
- (41) Pecharroman, C.; Cuesta, A.; Gutierrez, C. Calculation of Adsorption-Induced Differential External Reflectance Infrared Spectra of Particulate Metals Deposited on a Substrate. *J. Electroanal. Chem.* **2004**, *563* (1), 91–109. DOI: 10.1016/j.jelechem.2003.09.013.
- (42) Osawa, M.; Ataka, K.-I.; Yoshii, K.; Nishikawa, Y. Surface-Enhanced Infrared Spectroscopy: The Origin of the Absorption Enhancement and Band Selection Rule in the

- Infrared Spectra of Molecules Adsorbed on Fine Metal Particles. *Appl. Spectrosc.* **1993**, 47 (9), 1497–1502. DOI: 10.1366/0003702934067478.
- (43) Adato, R.; Artar, A.; Erramilli, S.; Altug, H. Engineered Absorption Enhancement and Induced Transparency in Coupled Molecular and Plasmonic Resonator Systems. *Nano Lett.* **2013**, 13 (6), 2584–2591. DOI: 10.1021/nl400689q.
- (44) Ataka, K.; Stripp, S. T.; Heberle, J. Surface-Enhanced Infrared Absorption Spectroscopy (SEIRAS) to Probe Monolayers of Membrane Proteins. *FTIR Membr. Proteins Pept. Stud.* **2013**, 1828 (10), 2283–2293. DOI: 10.1016/j.bbamem.2013.04.026.
- (45) Liao, P. F.; Wokaun, A. Lightning Rod Effect in Surface Enhanced Raman Scattering. *J. Chem. Phys.* **1982**, 76 (1), 751–752. DOI: 10.1063/1.442690.
- (46) Wang, H.; Kundu, J.; Halas, N. J. Plasmonic Nanoshell Arrays Combine Surface-Enhanced Vibrational Spectroscopies on a Single Substrate. *Angew. Chem. Int. Ed.* **2007**, 46 (47), 9040–9044. DOI: 10.1002/anie.200702072.
- (47) F. Neubrech; A. Pucci. Plasmonic Enhancement of Vibrational Excitations in the Infrared. *IEEE J. Sel. Top. Quantum Electron.* **2013**, 19 (3), 4600809–4600809. DOI: 10.1109/JSTQE.2012.2227302.
- (48) Alonso-González, P.; Albella, P.; Schnell, M.; Chen, J.; Huth, F.; García-Etxarri, A.; Casanova, F.; Golmar, F.; Arzubiaga, L.; Hueso, L. E.; Aizpurua, J.; Hillenbrand, R. Resolving the Electromagnetic Mechanism of Surface-Enhanced Light Scattering at Single Hot Spots. *Nat. Commun.* **2012**, 3, 684. DOI: 10.1038/ncomms1674.
- (49) Rhodes, C.; Cerruti, M.; Efremenko, A.; Losego, M.; Aspnes, D. E.; Maria, J.-P.; Franzen, S. Dependence of Plasmon Polaritons on the Thickness of Indium Tin Oxide Thin Films. *J. Appl. Phys.* **2008**, 103 (9), 093108. DOI: 10.1063/1.2908862.
- (50) D.E. Aspnes. Local-field Effects and Effective-medium Theory: A Microscopic Perspective. **1982**, 50 (8), 704–709.
- (51) McNutt, A.; Haq, S.; Raval, R. High Temperature Phase of the DNA Base Thymine on Cu(110): A Resonance Delocalised Bonding System. *Surf. Sci.* **2002**, 502–503, 185–192. DOI: 10.1016/S0039-6028(01)01931-8.
- (52) Hecht, E. *Optics*, 4th ed.; Pearson Education, Inc., 2002.
- (53) Fresnel, A. J. *Oeuvres Complètes d'Augustin Fresnel: Volume I*; Impr. Impériale, 1866.
- (54) Abelès, F. La Théorie Générale Des Couches Minces. *J. Phys. Radium* **1950**, 11 (7), 307–309. DOI: 10.1051/jphysrad:01950001107030700.
- (55) Passler, N. C.; Paarmann, A. Generalized  $4 \times 4$  Matrix Formalism for Light Propagation in Anisotropic Stratified Media: Study of Surface Phonon Polaritons in Polar Dielectric

- Heterostructures. *J. Opt. Soc. Am. B* **2017**, *34* (10), 2128–2139. DOI: 10.1364/JOSAB.34.002128.
- (56) Brouers, F.; Clerc, J. P.; Giraud, G.; Laugier, J. M.; Randriamantany, Z. A. Dielectric and Optical Properties Close to the Percolation Threshold. II. *Phys. Rev. B* **1993**, *47* (2), 666–673. DOI: 10.1103/PhysRevB.47.666.
- (57) Berthier, S.; Driss-Khodja, K.; Lafait, J. Optical Dielectric Function of Inhomogeneous Media Calculated by Kadanoff's Block Method. *Europhys. Lett. EPL* **1987**, *4* (12), 1415–1420. DOI: 10.1209/0295-5075/4/12/013.
- (58) Berthier, S.; Peiro, J. Anomalous Infra-Red Absorption of Nanocermetes in the Percolation Range. *J. Phys. Condens. Matter* **1998**, *10* (16), 3679–3694. DOI: 10.1088/0953-8984/10/16/019.
- (59) Decker, M.; Staude, I.; Pertsch, T.; Burger, S.; Petschulat, J.; Scharf, T.; Werdehausen, D. Using Effective Medium Theories to Design Tailored Nanocomposite Materials for Optical Systems. In *Current Developments in Lens Design and Optical Engineering XIX*; Johnson, R. B., Mahajan, V. N., Thibault, S., Eds.; SPIE, 2018. DOI: 10.1117/12.2320525.
- (60) Zare, S.; Pouria, R.; Edalatpour, S. Validity of the Effective Medium Theory for Modeling Near-Field Thermal Emission by Nanowire Arrays. *J. Quant. Spectrosc. Radiat. Transf.* **2021**, *261*, 107482. DOI: 10.1016/j.jqsrt.2020.107482.
- (61) Sihvola, A. Mixing Rules with Complex Dielectric Coefficients. *Subsurf. Sens. Technol. Appl.* **2000**, *1* (4), 393–415. DOI: 10.1023/A:1026511515005.
- (62) Jansson, R.; Arwin, H. Selection of the Physically Correct Solution in the N-Media Bruggeman Effective Medium Approximation. *Opt. Commun.* **1994**, *106* (4), 133–138. DOI: 10.1016/0030-4018(94)90309-3.
- (63) Theiß, W. The Use of Effective Medium Theories in Optical Spectroscopy. In *Advances in Solid State Physics 33*; Helbig, R., Ed.; Springer Berlin Heidelberg: Berlin, Heidelberg, 1993; pp 149–176. DOI: 10.1007/BFb0107886.
- (64) Noh, T.; Song, P.; Sievers, A. Self-Consistency Conditions for the Effective-Medium Approximation in Composite Materials. *Phys. Rev. B Condens. Matter* **1991**, *44*, 5459–5464. DOI: 10.1103/PhysRevB.44.5459.
- (65) Schmidt, D.; Schubert, M. Anisotropic Bruggeman Effective Medium Approaches for Slanted Columnar Thin Films. *J. Appl. Phys.* **2013**, *114* (8), 083510. DOI: 10.1063/1.4819240.
- (66) Markel, V. A. Introduction to the Maxwell Garnett Approximation: Tutorial. *J. Opt. Soc. Am. A* **2016**, *33* (7), 1244–1256. DOI: 10.1364/JOSAA.33.001244.

- (67) Granqvist, C. G.; Hunderi, O. Optical Properties of Ag-SiO<sub>2</sub> Cermet Films: A Comparison of Effective-Medium Theories. *Phys. Rev. B* **1978**, *18* (6), 2897–2906. DOI: 10.1103/PhysRevB.18.2897.
- (68) A. H. Sihvola; J. A. Kong. Effective Permittivity of Dielectric Mixtures. *IEEE Trans. Geosci. Remote Sens.* **1988**, *26* (4), 420–429. DOI: 10.1109/36.3045.
- (69) Bergman, D. J. The Dielectric Constant of a Composite Material—A Problem in Classical Physics. *Phys. Rep.* **1978**, *43* (9), 377–407. DOI: 10.1016/0370-1573(78)90009-1.
- (70) Johanson, R.; Kasap, S.; Koughia, C.; Ruda, H. Inhomogeneous Media. Effective Media Approximation. In *Springer Handbook of Electronic and Photonic Materials*; Springer International Publishing AG, 2017; pp 32–35.
- (71) Xu, G.; Tazawa, M.; Jin, P.; Nakao, S. Surface Plasmon Resonance of Sputtered Ag Films: Substrate and Mass Thickness Dependence. *Appl. Phys. A* **2005**, *80* (7), 1535–1540. DOI: 10.1007/s00339-003-2395-y.
- (72) Chatterjee, A.; Chakravorty, D. Glass-Metal Nanocomposite Synthesis by Metal Organic Route. *J. Phys. Appl. Phys.* **1989**, *22* (9), 1386–1392. DOI: 10.1088/0022-3727/22/9/025.
- (73) Wooten, F. *Optical Properties of Solids*; Academic Press: New York, 1972.
- (74) Sreekanth, K. V.; De Luca, A.; Strangi, G. Experimental Demonstration of Surface and Bulk Plasmon Polaritons in Hypergratings. *Sci. Rep.* **2013**, *3* (1), 3291. DOI: 10.1038/srep03291.
- (75) Goswami, S.; Kumar Sharma, A.; Biswas, S.; Alagarsamy, P. Evolution of Epsilon-near-Zero Plasmon with Surface Roughness and Demonstration of Perfect Absorption in Randomly Rough Indium Tin Oxide Thin Films. *J. Appl. Phys.* **2021**, *130* (17), 173102. DOI: 10.1063/5.0062208.
- (76) Franzen, S.; Rhodes, C.; Cerruti, M.; Gerber, R. W.; Losego, M.; Maria, J.-P.; Aspnes, D. E. Plasmonic Phenomena in Indium Tin Oxide and ITO-Au Hybrid Films. *Opt. Lett.* **2009**, *34* (18), 2867–2869. DOI: 10.1364/OL.34.002867.
- (77) Dzedolik, I. V.; Lapayeva, S. N. Mass of Polaritons in Different Dielectric Media. *J. Opt.* **2010**, *13* (1), 015204. DOI: 10.1088/2040-8978/13/1/015204.
- (78) Franzen, S. Surface Plasmon Polaritons and Screened Plasma Absorption in Indium Tin Oxide Compared to Silver and Gold. *J. Phys. Chem. C* **2008**, *112* (15), 6027–6032. DOI: 10.1021/jp7097813.
- (79) Kurdesau, F.; Khripunov, G.; da Cunha, A. F.; Kaelin, M.; Tiwari, A. N. Comparative Study of ITO Layers Deposited by DC and RF Magnetron Sputtering at Room Temperature. *Amorph. Nanocrystalline Semicond. - Sci. Technol.* **2006**, *352* (9), 1466–1470. DOI: 10.1016/j.jnoncrysol.2005.11.088.

- (80) Gas Flow. In *A User's Guide to Vacuum Technology*; John Wiley & Sons, Ltd, 2003; pp 25–56. DOI: <https://doi.org/10.1002/0471467162.ch3>.
- (81) Quirk, A.; Unni, B.; Burgess, I. J. Surface Enhanced Infrared Studies of 4-Methoxypyridine Adsorption on Gold Film Electrodes. *Langmuir* **2016**, *32* (9), 2184–2191. DOI: [10.1021/acs.langmuir.5b04178](https://doi.org/10.1021/acs.langmuir.5b04178).
- (82) Andvaag, I. R.; Lins, E.; Burgess, I. J. An Effective Medium Theory Description of Surface-Enhanced Infrared Absorption from Metal Island Layers Grown on Conductive Metal Oxide Films. *J. Phys. Chem. C* **2021**. DOI: [10.1021/acs.jpcc.1c06627](https://doi.org/10.1021/acs.jpcc.1c06627).
- (83) Yamaguchi, T.; Yoshida, S.; Kinbara, A. Effect of Retarded Dipole–Dipole Interactions between Island Particles on the Optical Plasma-Resonance Absorption of a Silver-Island Film. *J. Opt. Soc. Am.* **1974**, *64* (11), 1563–1568. DOI: [10.1364/JOSA.64.001563](https://doi.org/10.1364/JOSA.64.001563).
- (84) Fedotov, V. A.; Emel'yanov, V. I.; MacDonald, K. F.; Zheludev, N. I. Optical Properties of Closely Packed Nanoparticle Films: Spheroids and Nanoshells. *J. Opt. Pure Appl. Opt.* **2003**, *6* (2), 155–160. DOI: [10.1088/1464-4258/6/2/001](https://doi.org/10.1088/1464-4258/6/2/001).
- (85) Zhao, C.; Mei, Z. The Effective Permittivity of the Coated Ellipsoid: A Tunable Electromagnetic Parameter Approach. *J. Phys. Appl. Phys.* **2017**, *50* (50), 505001. DOI: [10.1088/1361-6463/aa9606](https://doi.org/10.1088/1361-6463/aa9606).
- (86) Gittleman, J. I.; Abeles, B. Comparison of the Effective Medium and the Maxwell-Garnett Predictions for the Dielectric Constants of Granular Metals. *Phys. Rev. B* **1977**, *15* (6), 3273–3275. DOI: [10.1103/PhysRevB.15.3273](https://doi.org/10.1103/PhysRevB.15.3273).
- (87) Lins, E. Ph.D. Thesis, University of Saskatchewan, in prep.
- (88) Bohren, C.; Huffman, D. Particles Small Compared with the Wavelength. In *Absorption and Scattering of Light by Small Particles*; John Wiley & Sons, Ltd, 1983; pp 130–157.
- (89) Osborn, J. A. Demagnetizing Factors of the General Ellipsoid. *Phys. Rev.* **1945**, *67* (11–12), 351–357. DOI: [10.1103/PhysRev.67.351](https://doi.org/10.1103/PhysRev.67.351).
- (90) Bruggeman, D. A. G. Berechnung Verschiedener Physikalischer Konstanten von Heterogenen Substanzen. I. Dielektrizitätskonstanten und Leitfähigkeiten der Mischkörper aus Isotropen Substanzen. *Ann. Phys.* **1935**, *416* (7), 636–664. DOI: [10.1002/andp.19354160705](https://doi.org/10.1002/andp.19354160705).
- (91) Horn, R. A.; Johnson, C. R. Eigenvalues of the Companion Matrix. In *Matrix Analysis*; Cambridge University Press: Cambridge, UK, 1999; pp 146–147.
- (92) Hashin, Z.; Shtrikman, S. A Variational Approach to the Theory of the Effective Magnetic Permeability of Multiphase Materials. *J. Appl. Phys.* **1962**, *33* (10), 3125–3131. DOI: [10.1063/1.1728579](https://doi.org/10.1063/1.1728579).

- (93) Duncan, A. J.; Mackay, T. G.; Lakhtakia, A. On the Bergman–Milton Bounds for the Homogenization of Dielectric Composite Materials. *Opt. Commun.* **2007**, *271* (2), 470–474. DOI: 10.1016/j.optcom.2006.10.056.
- (94) Postava, K.; Sýkora, R.; Legut, D.; Pištora, J. Determination of Anisotropic Crystal Optical Properties Using Mueller Matrix Spectroscopic Ellipsometry. *6<sup>th</sup> New Methods Damage Fail. Anal. Struct. Parts* **2016**, *12*, 118–123. DOI: 10.1016/j.mspro.2016.03.021.
- (95) Rodrigues. Des lois géométriques qui régissent les déplacements d'un système solide dans l'espace, et de la variation des coordonnées provenant de ces déplacements considérés indépendamment des causes qui peuvent les produire. *J. Mathématiques Pures Appliquées* **1840**, 380–440.
- (96) Campione, S.; Brener, I.; Marquier, F. What Is an Epsilon-near-Zero Mode? In *Advanced Photonics 2015*; OSA Technical Digest (online); Optica Publishing Group: Boston, Massachusetts, 2015; p IM4A.5. DOI: 10.1364/IPRSN.2015.IM4A.5.
- (97) Simon, S.; Clarke, O. J. R.; Burgess, I. J. On the Ligand Exchange, Redox, and Disproportionation Processes of Tetrachloroaurate in the Presence of a Pyridine Derivative. *Electrochim. Acta* **2020**, *363*, 137213. DOI: 10.1016/j.electacta.2020.137213.
- (98) Doña, J. M.; González-Velasco, J. The Dependence of the Surface Diffusion Coefficients of Gold Atoms on the Potential: Its Influence on Reconstruction of Metal Lattices. *Surf. Sci.* **1992**, *274* (2), 205–214. DOI: 10.1016/0039-6028(92)90524-A.
- (99) Sakai, N.; Fujiwara, Y.; Arai, M.; Yu, K.; Tatsuma, T. Electrodeposition of Gold Nanoparticles on ITO: Control of Morphology and Plasmon Resonance-Based Absorption and Scattering. *J. Electroanal. Chem.* **2009**, *628* (1), 7–15. DOI: 10.1016/j.jelechem.2008.12.008.
- (100) Waldfried, P. *Electrochemistry for Materials Science*; Elsevier B.V.: Oxford, UK, 2008.
- (101) Osawa, M.; Ataka, K.; Yoshii, K.; Yotsuyanagi, T. Surface-Enhanced Infrared ATR Spectroscopy for in Situ Studies of Electrode/Electrolyte Interfaces. *J. Electron Spectrosc. Relat. Phenom.* **1993**, *64–65*, 371–379. DOI: 10.1016/0368-2048(93)80099-8.
- (102) Sigrist, J. A.; Lins, E. S.; Morhart, T. A.; Briggs, J. L.; Burgess, I. J. Optimization of a Commercial Variable Angle Accessory for Entry Level Users of Electrochemical Attenuated Total Reflection Surface-Enhanced Infrared Absorption Spectroscopy (ATR-SEIRAS). *Appl Spectrosc* **2019**, *73* (12), 1394–1402. DOI: 10.1177/0003702819858353.
- (103) Ohta, K.; Ishida, H. Matrix Formalism for Calculation of Electric Field Intensity of Light in Stratified Multilayered Films. *Appl Opt* **1990**, *29* (13), 1952–1959.
- (104) Rumpf, R. C. *Electromagnetic and Photonic Simulation for the Beginner: Finite-Difference Frequency-Domain in MATLAB®*; Artech, 2022.

## **8 APPENDIX: DETAILED SPUTTERING INSTRUCTIONS**

### **8.1 Introductory notes**

This manual describes the procedure to be followed to operate the magnetron sputtering unit (MagSput-4G2-RF/DC-HOT-UpG, Torr International, Inc.) in the thin film lab in Engineering 3C18. The user must be trained by the owner of the equipment (at present, Dr. Robert Johanson) and obtain permission to utilize the equipment. This manual does not serve as a substitute to in-person training.

A significant concern with the current configuration of the sputtering unit is to avoid exposing turbo pump to atmospheric pressure while spinning. There is no interlock preventing you from making this very expensive mistake!

The system has two gauges for measuring the pressure. The primary gauge is a “combination” gauge (green LED display). This gauge contains two sensing elements: a thermocouple and an ion gauge, both of which depend on the identity of the gas measured. This gauge reads over a large range, from atmospheric down to the lowest base pressure attainable by the system. The second gauge is a capacitance manometer in (red LED display). This gauge only has 3 decades of range (0.001 to 1 Torr), but reads correctly regardless of the gas and should be preferred as the more accurate gauge in the operating regime.

The system is colour-coded. Yellow lines indicate air pressure for pneumatically controlled gate valve. Green lines are for water coolant for sputtering gun and quartz crystal.

### **8.2 Changing the target**

Loosen the knurled locking ring on the gun slightly. Unscrew the metal hood/shield, which is grounded. Under the hood is a metal collar which holds the target. This collar is under high voltage during operation. With one hand underneath the collar, unscrew the collar and remove the existing target. Install the new target in the collar and screw the collar on being careful not to cross-thread it. Tighten until just finger tight. There is a metal sheath around the collar; slide it up. Re-attach the metal hood/shield. There must be a gap between the hood (which is grounded) and the collar (which is under high voltage.) There is a gap-ing tool (piece of bent copper wire that is

somewhere around 8 or 10 gauge). Insert the gap-ing tool between the hood and the collar, and tighten the collar (but not so much that you cannot remove the gap-ing tool.)

### 8.3 Calibrating the thickness measurement of the quartz crystal monitor

Two parameters must be known and input into the control panel:

- The empirically-determined tooling factor, independent of material
- The Young's modulus of the material

These parameters can be input by depressing the “program” button, selecting the Film Number to store the parameters into memory, and setting the values with the up and down arrows.

### 8.4 Instructions for use

Vent the system. After making sure that the desired target is installed, load the substrates and shut the door. Turn the air on and open the gate valve (only if Turbo pump is not spinning!) first to 50%, then to 100%. Shut off vent. Record in log book:

-Air on. Gate valve open. Water on. Mechanical pump on.

t (min)	P (Torr)
1	15
2	.64
3	0.17
..	..
15	2.4E-5

-Turbo pump on (safe to do so after pumping down to a pressure of about 0.1 T, approx. 4 min.)

AC generators are used for both dielectric and metallic targets. DC is used only for conductive targets. Turn on the power to the RF (AC) generator, but do not press the “run” button yet. Adjust the incident power with the up and down arrows. Commence platform rotation by turning on the “motor” switch. Turn on the Ar at the tank. Consider the Ar flow controller operation: A dial on the left hand side is used to change settings between:

- “flow”, which gives a readout of the Ar flow in units of SCCM (i.e.  $\text{cm}^3 / \text{min}$ )
- “set”, which allows the user to change the Ar flow rate using the adjustment knob on the right hand side.

A three-way switch on the bottom is used to change between the following settings:

- “close”, for no Ar flow
- “control”, for normal Ar flow
- “purge”, for a burst of Ar to strike a plasma

Record the pressure in the logbook. Turn the dial on the flow controller to “set” and verify that the flow rate is sensible (we used “1.7”). Open the Ar valve (toggle switch marked “Argon”.) Switch the Ar flow controller switch from “close” to “control”. After several seconds, check that flow equals set point, i.e. that the controller is functioning properly.

Record in log book: Flowing Ar at “1.7” ;  $P = 2.1\text{E-}3$  Torr.

Check through the window that your substrates have not been displaced from the sputtering stage. The next step is a bit challenging and should be practiced before attempting. In relatively quick succession:

Turn on the RF generator. Need to turn on “Gun 2” to override the interlock. Check window for plasma strike. If plasma does not strike, flick the Ar controller switch to “purge” for a split second. Press “zero” to zero the thickness and the time. Adjust the two knobs (“Tune” and “Control”) on the AC generator such that the reflected power reads zero.

Record in log book:

t (min)	P (T)	Power reflected (W)	Thickness ( $\text{\AA}$ )
0	-	-	0
1	2.2E-3	0	4
2	2.2E-3	0	9
5	2.2E-3	0	26
10	2.2E-3	0	55
..	..	..	..
50	2.2E-3	0	310

Record the thickness every five minutes and verify that the sputtering rate is either staying the same, or slowly increasing at a constant rate.

## **8.5 Shutdown procedure**

Turn off RF power (can turn off “Gun 2”, or on the generator itself.) Shut off Ar with the valve (toggle above the controller), then turn off the Ar at the tank. Record the pressure in the log book. Switch Ar flow controller to “close”. Close gate valve, first flip the 100% switch, then the 50% switch. Turn turbo pump off. Turn off the switch marked “motor”. Turn off water, leave air on so as to be able to operate the gate. Wait 10 min, then turn off mechanical pump. Loosen the threaded door lock. Turn on “vent” switch (recall: the gate is closed at this point.) Note: you cannot open the vent valve until the mechanical pump is off. Wait an additional 10 min (20 min from the point at which the turbo pump was turned off.) Listen to ensure that the turbo pump is no longer spinning. After 20 min and the turbo pump is no longer spinning, open the gate.

Open the door and remove the samples from the chamber. Remove your target, unless you will be returning shortly to do more sputtering with the same material. Close the door, and pump down to 100 mT with the mechanical pump. After attaining a pressure of 0.1 T, close the gate and turn off the pump. Turn off the air.